CHARACTERIZATION AND MODELING OF WICKING IN ORDERED SILICON NANOSTRUCTURED SURFACES FABRICATED BY INTERFERENCE LITHOGRAPHY AND METAL-ASSISTED CHEMICAL ETCHING

MAI TRONG THI

NATIONAL UNIVERSITY OF SINGAPORE

2013

CHARACTERIZATION AND MODELING OF WICKING IN ORDERED SILICON NANOSTRUCTURED SURFACES FABRICATED BY INTERFERENCE LITHOGRAPHY AND METAL-ASSISTED CHEMICAL ETCHING

MAI TRONG THI

(B. Eng (Hons), Electrical Engineering, National University of Singapore)

A THESIS SUBMITTED FOR THE DEGREE OF

DOCTOR OF PHILOSOPHY

DEPARTMENT OF ELECTRICAL AND COMPUTER ENGINEERING

NATIONAL UNIVERSITY OF SINGAPORE

2013

DECLARATION

I hereby declare that this thesis is my original work and it has been written by me in its entirety. I have duly acknowledged all the sources of information which have been used in the thesis.

This thesis has also not been submitted for any degree in any university previously.

_____

Mai Trong Thi

14th Mar 2014

ACKNOWLEDGEMENTS

This project would not have been feasible without the guidance, support and constant encouragement of many individuals. Firstly, I would like to express my deepest gratitude to my thesis supervisor, Professor Choi Wee Kiong, for his invaluable guidance throughout the progress of my research. I would also like to thank Associate Professor Vincent Chengkou Lee, who always provided me with his invaluable advices.

I am sincerely grateful to our wonderful lab technicians Mr. Walter Lim and Mdm. Ah Lian Kiat for all the assistance rendered during the course of my research. During my stay in the Microelectronics Lab, I had many insightful discussions with my seniors Khalid, Tze Haw, Raja, Wei Beng, Yudi, and fellow schoolmates Changquan, Zheng Han, Cheng He, Zhu Mei, Bihan, Ria, Zongbin. I would like to thank them all for their great companionship and all the great memories.

I would also like to express my appreciation to Assistant Professor PS Lee for his kind provision of the high speed camera needed for the experiment. Special thanks to Ms. Roslina, Karthik, Tamana and Matthew from the Thermal Process Lab 2 for their help with arrangements and experiment setups.

Thanks my good friends Mariel and Nicole for helping me proofread this thesis, not only once but twice.

Finally, this thesis is dedicated to my family, particularly my Mom, Dad and Sister. I would not have been able to complete this thesis without their unfailing love and support.

TABLE OF CONTENTS

ACKNOWLEDGEMENTS i

TABLE OF CONTENTS iii

SUMMARY v

LIST OF TABLES vii

LIST OF FIGURES viii

LIST OF SYMBOLS xiii

Chapter 1 Introduction 1

1.1 Background 1

1.2 Motivation 5

1.3 Research Objectives 6

1.4 Thesis Organization 7

1.5 References 9

Chapter 2 Literature Review 12

2.1 Introduction 12

2.2 Basic Laws of Wetting and Spreading 13

2.3 Wicking in Irregular and Regular Micro-/Nano- Structures 20

2.4 Dynamics of Wicking 24

2.5 Initial Stage of Wicking 29

2.6 Basic Equations 33

2.7 Summary 36

2.8 References 37

Chapter 3 Experimental Techniques 42

3.1 Introduction 42

3.2 Wafer Cleaning 43

3.3 Interference Lithography 45

3.4 Plasma-Assisted Etching 48

3.5 Thermal Evaporation 49

3.6 Metal-assisted Chemical Etching 50
3.7 Characterization Techniques 54
3.8 References 60

Chapter 4 Results and Discussion I 62
4.1 Introduction 62
4.2 Experimental Details 64
4.3 Theoretical Model 66
4.4 Results and Discussion 78
4.5 Summary 87
4.6 References 89

Chapter 5 Results and Discussion II 92
5.1 Introduction 92
5.2 Experimental Details 94
5.3 Experimental Results 99
5.4 Theoretical Model 102
5.5 Discussion 108
5.6 Conclusions 112
5.7 References 114

Chapter 6 Results and Discussion III 116
6.1 Introduction 116
6.2 Experimental details 117
6.3 Shape Matters 121
6.4 Results and Discussions 125
6.5 Conclusions 144
6.6 References 145

Chapter 7 Conclusion 147
7.1 Summary 147
7.2 Future Works 150

APPENDIX A 151

APPENDIX B 153

SUMMARY

The objective of this study is to investigate and quantitatively characterize the wicking phenomenon of liquid on ordered silicon nanostructures fabricated by the interference lithography and metal-assisted etching techniques.

This thesis firstly presents a theoretical study and an experimental validation of the wicking dynamics in a regular silicon nanopillar surface. Due to the small scale of the dimensions of interest, we found that the influence of gravitational force was negligible. The forces acting on the body of the liquid were identified to be the capillary force, the viscous force, and skin friction due to the existence of nanostructures on the surface. By approximating one nanopillar primitive cell as a cell of nanochannel, the Navier-Stokes equations for dynamics of wicking were simplified and could be solved. The wicking dynamics were expressed fully without use of empirical values. The enhancement factor of viscous loss, β, due to the presence of the nanopillars was found to depend on the ratio of h/w, where w was the width of the channel used to approximate the wicking and h was the height of the nanopillar. The theoretical values for β were found to fit well with the experimental data and published results from other research groups.

Secondly, the dependence of wicking dynamics on the geometry of nanostructures was investigated through experiments of wicking in anisotropic structures such as nanofins. It was found that nanostructures dissipated flow

energy through viscous and form drags. While viscous drag was present for every form of nanostructure geometry (i.e. nanopillars), form drag was only associated with nanostructure geometries that have flat planes normal to the wicking direction. It was also discovered that the viscous dissipation for a unit cell of nanofin could be effectively approximated with a nanochannel of equivalent height and length that contains the same volume of liquid. The energy dissipated by the form drag per unit cell of nanofin was proportional to the volume of the fluid between the flat planes of the nanofins and the driving capillary pressure. With these findings, we were able to establish the dependence of the drag enhancement factor β on the geometrical parameters of the nanostructures. This is important as it provides a precise method for adjusting β, and therefore wicking velocity, for a given direction on a surface by means of nanostructure geometry.

Finally, the initial stage of wetting where the speed of liquid spreading was much faster than the speed of wicking, was studied. It was found that the surface tensions were the predominant driving force. During this initial stage of wetting, the skin friction proved to be significant in determining the spreading distance of the liquid bulk. The average energy dissipation per unit area at the cross-over time was calculated for nanopillar samples of various dimensions. This was believed to be an intrinsic property of the combination of the solid and wetting liquid materials. Based on this, the spreading diameter of the liquid bulk could be estimated.

LIST OF TABLES

Table 4.1 Dimensions of silicon nanopillar samples fabricated by the IL-MACE method. Crucial parameters such as surface roughness *r*, pillars fraction ϕ_s and the critical contact angles θ_c were calculated.....80

Table 5.1 Geometrical parameters of nanofins used in this study where *h* refers to the height of the nanofins, and definitions of *p, q, m* and *n* can be found in Figure 5.4. Important parameters such as the pillar fraction (ϕ_s) and the surface roughness (*r*) were shown. 99

Table 6.1 Dimensions of silicon nanopillars fabricated by the IL-MACE method. Crucial parameters such as diameter, height, and period of the nanopillars are shown. The surface roughness *r* and solid fraction ϕ_s were also calculated. 120

Table 6.2 The volumes of the liquid contained in the pillars V_{film} are calculated as a percentage of the original droplet volume V_{drop} for different samples at cross-over time t_c.....130

Table 6.3 Identification of energy components prior to droplet touches the solid surface and at cross-over time t_c. 132

Table 6.4 Energy components of the system before dispensing and at cross-over time. Here *h* stands for the nanopillar height. E_{pot} is the potential energy, E_{LV}, E_{SL}, E_{SV} are the interfacial energy of liquid - vapor, solid-liquid and solid-vapor interfaces, respectively.....135

Table 6.5 Energy dissipation per unit area calculated for different drop sizes. 139

LIST OF FIGURES

Figure 1.1 Water rise in a capillary tube in a downward gravity field. 2

Figure 1.2 Examples of surface tensions. (a) A paperclip floats on the water surface despite its higher density. (b) A spider stands on the water surface. 3

Figure 1.3 Difference between (a) Spreading and (b) Wicking of liquid on a solid surface. (c) Example of wicking of an ethanol drop on a horizontal silicon wafer.[1] 5

Figure 2.1 A liquid droplet rests on a flat solid surface. The equilibrium contact angle, θ, is the angle formed by a liquid at the three phase boundary where the liquid, vapor, and solid phases intersect.....14

Figure 2.2 Flow of liquid through a cylindrical pipe. 15

Figure 2.3 Capillary rise in a circular tube of arbitrary shape.[7] 16

Figure 2.4 Metal surfaces treated by femto-second laser shows (a) the parallel micro-grooves and (b-d) the unintentionally created nanostructures inside.[29] 21

Figure 2.5 (a) Top-view and (b) side-view of silicon nanowires fabricated by the glancing angle deposition technique.[31] 21

Figure 2.6 Various arrays of nanotubes on glass fabricated by the anodic oxidation technique.[32] 22

Figure 2.7 Photographs showing methanol running uphill on a vertically standing platinum sample.[29].....22

Figure 2.8 Plot of the experimental results of the spreading distance z versus the square root of time $t^{1/2}$ of different materials being treated by a nano-second laser. [30] 23

Figure 2.9 Examples of micropillar structures fabricated for wicking study by (a) inductively coupled plasma etching[36] and (b) micro-imprinting.[37] The latter structure was utilized in Bico *et al.*[9]'s study.....24

Figure 2.10 Variation of the contact line and precursor rim diameters with respect to time. In Stage I, both the contact line and precursor rim expand at the same velocity, $D \sim t$. However, in Stage II, the contact line stops expanding, and the precursor rim continues to expand at a lower velocity than Stage I, $D \sim t^{1/2}$.[32] 30

Figure 2.11 Variation of the spreading distance with respect to time. (a) shows the characteristics of the starting stage where the spreading distance increases with time very quickly, while in the following stage the spreading distance increases slowly. (b) shows the influence of the initial spreading time t_0, where clearly once $t > t_0$, the slopes of these lines are almost similar to each other.[30] 31

Figure 2.12 Illustration of Bico's theory on the effective contact angle θ^*.[9] .31

Figure 2.13 Qualitative behaviors of fluid flow over a cylinder depend on different Reynolds number. 35

Figure 3.1 Experimental setup for Lloyd's Mirror Interference Lithography. The He-Cd laser beam is directed at the spatial filter and either reaches the sample surface directly (the solid arrow) or reflects off the mirror before reaching the sample surface (the dotted arrow). Periodic fringes are produced based on the principle of constructive and destructive waves. 47

Figure 3.2 Schematic drawing of a typical Thermal Evaporator. 50

Figure 3.3 Before etching, the samples went through the lift-off process to transfer the negative image of the photoresist to the metal film. 51

Figure 3.4 (a) Schematic drawing of the two stages of the metal-assisted chemical etching process. The location of the metal catalyst determines the regularity of the nanostructures. (b) Precipated Ag particles produced a forest of randomly located nanowires.[7] (c) Regular array of nanowires was obtained with carefully designed Au particles by means of photolithography. [8] 53

Figure 3.5 Schematic diagram of the Scanning Electron Microscopy. 56

Figure 3.6 Interaction between primary electrons and the sample surface generates backscattered electrons, secondary electrons, Auger electrons and X-rays. 57

Figure 3.7 The setup of a contact angle measurement experiment. The VCA Optima system consists of a stage, a volume control syringe/needle and a CCD camera. 58

Figure 3.8 Illustration of the high-speed camera experiment. A nanostructured sample was placed vertically on a flat surface and a droplet was delivered to the bottom of the sample. The whole wicking action was captured by the camera. 59

Figure 4.1 (a) Schematic diagram of the process flow to fabricate Si nanopillars using the IL-MACE method, (b) SEM images of Si nanopillars at a height of (i) ~2 μm, (ii) ~4 μm and (iii) ~7 μm, respectively. The insets are top-view SEM images of the respective samples. All samples in Figure 1(b) have the same period of 1μm. 65

Figure 4.2 Approximating a unit cell (indicated by dashed black rectangle) of nanopillars as a unit cell of nanochannels that holds the same volume of liquid. (a) shows the top view of a unit cell of nanopillars while (b) and (c) show the top view and side view of a nanochannel. The yellow regions indicate the top of the nanostructures at $y = h$, which remain dry throughout the wicking process, while the violet regions indicate the bottom regions at $y = 0$. Flow of fluid is in the z-direction in all cases. 67

Figure 4.3 Simulation of flow inside (a) an array of nanopillars and (b) a nanochannel. The color bar represents the magnitude of velocity where blue stands for zero velocity (stagnant flow) and red means maximum velocity. The red arrows indicate the flow direction. The parameters used in the simulation are: $d = 0.3$ μm, $s = 0.7$ μm, $h = 4$ μm and $w = 0.93$ μm. Similar results were obtained by varying h from 1 to 7 μm. 69

Figure 4.5 Boundary conditions for wicking flow on silicon nanopillars surface. 74

Figure 4.6 Contact angle of (a) water and (b) silicone oil estimated using a contact angle goniometer 79

Figure 4.7 Snapshots of the wicking process of silicone oil on silicon nanopillars surface (Sample B). The red dotted line marks the liquid front. ...81

Figure 4.8 Plot of distance travelled by the wetting front against the square root of time for nanopillars with silicone oil (γ = 3.399×10^{-2} N/m, μ = 3.94×10^{-2} Pas, θ_{oil} = 18^{o}). 82

Figure 4.9 Experimental and calculated values of β. Data points for β (silicone oil) and β (water) are obtained with silicone oil and water respectively. Calculation based on our method is represented by a solid line. Also shown in this figure are the calculated β values of our samples based on the models of Zhang *et al.*[20] and Ishino *et al.*[4] 83

Figure 4.10 Comparison of β values obtained by our methods and others for the micropillars experiment presented in Ishino *et al.*'s paper. Experimental and theoretical values are plotted as points and lines respectively. Our model is represented by a solid blue line. Five different test liquids (γ = 2×10^{-2} N/m) were used and their respective viscosities are given in the legend. d = 2 μm and s = 8 μm remained constant for all experiments. 85

Figure 5.1 Different patterns can be achieved by utilizing multiple exposure method. For instance, a double exposure of 90^{o} (a) will create nanopillar structures after further processing (developing and etching). A double exposure of less than 90^{o} (b) will create nanofin structures. 95

Figure 5.2 Photoresist (denoted by the black color dots) remaining after (a) a single exposure, (b) a double exposure of 90^{o} and (c) a double exposure of less than 90^{o}. The white areas represent the silicon surface. To study wicking in nanofin structures, the sample is tilted so that the nanofins' major axis stands either vertically along the *z*-axis direction (*z* (*normal*)) like illustrated in (d), or horizontally (*z* (*parallel*)). Photo in (e) shows a representative sample tilted for *z* (*normal*) setup. SEM image in (f) shows that the fins' major axis is indeed along the *z*-axis direction. 96

Figure 5.3 SEM pictures of nanofin samples A - K used for this study tilted at 35^{o} angle. Insets show top view of nanofins. Each scale bar represents 2μm. 98

Figure 5.4 Schematic diagram (top-view) of the nanofin structures. The area of the dark blue region is given by *A* and the mean velocity of the fluid in this area is assumed to be zero when wicking occurs in *z (normal)* direction. Note also that $p' << p$ for all our samples. The dotted line demarcates a unit cell of the nanofins. 100

Figure 5.5 Snapshots of the wicking process of silicone oil on representative silicon nanofins surface. The sample is slightly tilted to examine wicking in *z (normal)* direction. The red dotted line marks the liquid front. 100

Figure 5.6 Representative *z* vs. $t^{1/2}$ plots obtained experimentally for wicking of silicone oil on a single sample surface. Best fit lines were drawn through the data points. 102

Figure 5.7 Plot of *A* vs. *pn* where *A*, *p* and *n* are structural parameters of the nanofin structure and are illustrated in Figure 5.4. The best fit line drawn

through the data points has a gradient value of 0.912 and passes through the origin. 109

Figure 5.8 Experimental values of $(1 - f)\ \beta$ vs. h/w where f represents the fraction of fluid that is stagnant, β is the drag enhancement factor, h and w are the height and width of the nanochannel used to appromixate the flow, respectively. Note that $f = 0$ for wicking in *z (parallel)* direction. 110

Figure 5.9 Plot of β *(parallel)*/ β *(normal)* vs. $(1\text{-}f)(w_n/w_p)^2$. β *(parallel)* > β *(normal)* in the orange region and β *(parallel)* < β *(normal)* in the smaller green region. No data points were expected to reside in the white regions. Only data from samples with $h/w > 2$ for both *z (normal)* and *z (parallel)* were used in this plot. 112

Figure 6.1 Experimental setup for the spreading experiments of liquid on nanostructure surfaces. The samples were put on a horizontal surface. The microbalance serves to determine the amount of liquid dispensed.....118

Figure 6.2 Water droplet of 1 µl forms a perfect sphere on the tip of the pipette.....119

Figure 6.3 Illustration of the liquid bulk and the thin film spreading on a silicon nanopillar surface. 121

Figure 6.4 (a) A 1µl water droplet on a flat silicon surface resulted in a spherical cap shape; and (b) Schematic diagram of a spherical cap with dimensional parameters. R is the radius of the spherical cap. H is the height of the droplet. D_{bulk} and D_{film} is the spreading diameter of the liquid bulk and the thin film, respectively. y_m denotes the center of gravity for the droplet. And θ is the contact angle. 122

Figure 6.6 The separation of liquid bulk and thin film spreadings as seen at $t > t_c$. 125

Figure 6.7 Spreading distances of the liquid bulk and the thin film versus the square root of time. The spreading and wicking regimes are clearly shown. The spreading diameter D_c and the cross over time t_c were identified.....126

Figure 6.9 Illustration of different contact angles at cross-over time for (a) a tall pillar sample and (b) a short pillar sample. It can be seen that $\theta_{tall} > \theta_{short}$. 131

Figure 6.10 Illustration of two energy states: (a) before the droplet touches the solid surface and (b) at t_c.....131

Figure 6.11 Total energy dissipation per unit area for different pillar heights. 136

Figure 6.12 Comparison of the spherical cap shape (represented by the solid line) and the real drop shape when spreading diameter is large. Picture taken from Harth *et al.*[1] 137

Figure 6.13 Spreading distance of the thin film diameter versus time for different drop volumes of (a) Sample F (height of 4.18 µm) and (b) Sample H (height of 5.39 µm). 138

Figure 6.14 Plot of cross-over time versus nanopillar heights for various drop sizes. The red line represents the average value of 10 milliseconds.....140

Figure 6.15 Theory and experimental spreading diameter at cross-over time for nanopillars samples of different heights.....143

Figure A1 Plot of *E* versus (a) *m* when *n* = 0 and (b) *n* when *m* = 0. Width (*w*) and height (*h*) of the nanochannel are fixed at 1μm and 2 μm respectively..152

LIST OF SYMBOLS

SEM	Scanning Electron Microscopy
IL	Interference Lithography
MACE	Metal-Assisted Chemical Etching
^{o}C	Degree Celsius
Ω	electrical resistance
λ	wavelength of the laser source (nm)
λ_c	capillary length (m)
ρ	mass density (kg/m^3)
θ	intrinsic contact angle the liquid makes with a flat solid surface
θ_c	critical contact angle ($0° \leq \theta_c \leq 90°$) or the maximum contact angle that wicking occur
γ	surface tension (N/m)
γ_{SV}, γ_{SL}, γ_{LV}	surface tension at solid-vapor, solid-liquid, liquid-vapor respectively
μ	viscosity (Pas)
β	viscous enhancement factor
r	roughness of the textured surface (ratio of the actual surface area to projected area)
ϕ_s	fraction of area of the solid tops, i.e. ratio of the area of the top of the nanostructure (which was assumed to remain dry) to the projected area
h	height of the nanostructures
z	distance of wicking
V	mean velocity (V= dz/dt)
t	time after the start of wicking (s)
ΔP	driving capillary pressure

Chapter 1

Introduction

1.1 Background

Around 450 B.C., the Greek philosopher Empedocles proposed that human being needed only two fundamental forces to account for all natural phenomena. One was Love, and the other was Hate. The former brought things together while the latter caused them to part.

As nonsensical as it may sound to modern scientists, Empedocles's philosophy embodied a pivotal understanding: every phenomenon that happened is the result of the continuous interactions of various basic forces, which are either attractive or repulsive in nature.[a] One of these forces – the gravitational force when acting together with intermolecular forces (surface tension) determines a class of phenomena known as capillary action (or capillarity).

Phenomena governed by capillarity pervade all facets of our daily life. The term '*capillary'*, adapted from the Latin word '*capillus*' for hair, was

[a] Until recently, the four basic forces were identified to either act in the nuclear level (known as Strong and Weak force) or act between atoms and molecules (known as Electromagnetic and Gravitational interactions).

applied to the phenomenon since it was firstly observed to give rise to water inside tubes with very fine openings (Figure 1.1). Clarification of the behavior became one of the major problems challenging the scientific world of the eighteenth century.

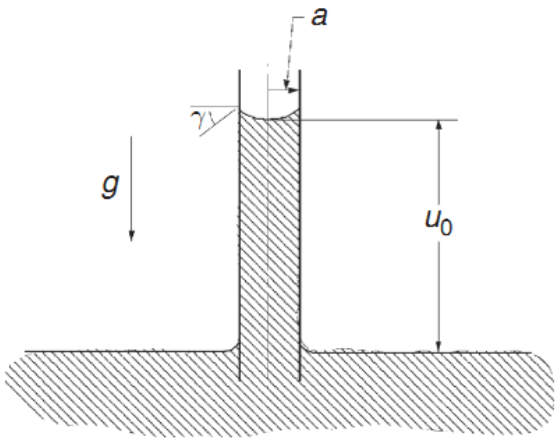

Figure 1.1 Water rise in a capillary tube in a downward gravity field.

Surface tension is an effect of liquid intermolecular attraction (adhesive and cohesive forces), in which molecules at or near the surface undergo a net attraction to the rest of the fluid, and molecules farther away from the surface are attracted to other molecules equally in all directions and undergo no net attraction. Surface tension plays an important role in the way liquids behave. By carefully placing a paperclip on a glass of water, the clip does not sink even though it is denser than water (Figure 1.2(a)). This is because the water molecules at the surface stick together and behave like an elastic film that supports the weight of the paperclip. Nature has used surface tension to develop several ingenious designs for insect propulsion, water collection and capillary adhesion. One example is the water spiders which can

run across the surface of water (Fig 1.2(b)). Their hairy legs prevent water from wetting them. Instead of penetrating the surface and sinking, their feet deform the interface, generating a surface tension force that supports the body weight.

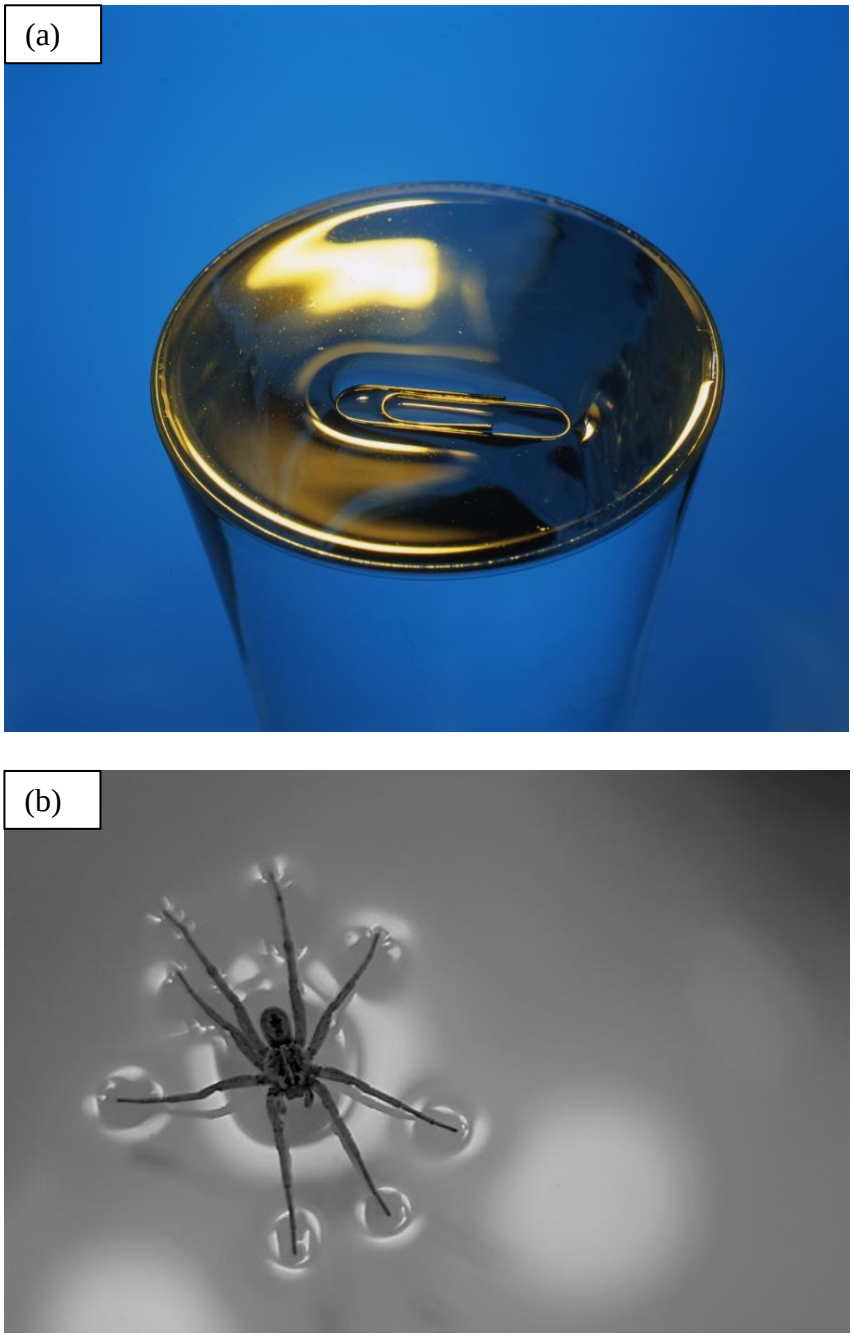

Figure 1.2 Examples of surface tensions. (a) A paperclip floats on the water surface despite its higher density. (b) A spider stands on the water surface.

Capillarity (or capillary action) is the direct consequence of surface tension. When a narrow glass circular-cylindrical tube is dipped vertically into water (Figure1.1), the liquid creeps up the inside of the tube as a result of attraction forces between the liquid molecules (cohesive force) and between the liquid and the inner walls of the tube (adhesive force). These phenomenon stops once these forces are balanced by the weight of the liquid.

Wicking, on the other hand, is the absorption of a liquid by a material through capillary action. For instance, small pores inside paper towels act as small capillaries that allow a fluid to be transferred from a surface to the towel. This behavior is similar to the manner of a candle wick, hence the term *wicking*. These common occurrences are all governed by the physics at the interface where the liquid, gas and solid phases meet. In other words they are dictated by the surface tension and the liquid-solid wettability.

Despite the similarity between spreading and wicking, there is a clear distinction between them which is illustrated in Figure 1.3. The spreading of liquid indicates the movement of the drop contact line until it reaches an equilibrium state governed by the Young's law which will be introduced later in Chapter 2 (Figure 1.3(a)). On the contrary, wicking is characterized by the extension of a thin film of liquid ahead of the drop (Figure 1.3(b)). A real example of wicking of an ethanol drop on a horizontal silicon wafer is shown in Figure 1.3(c).

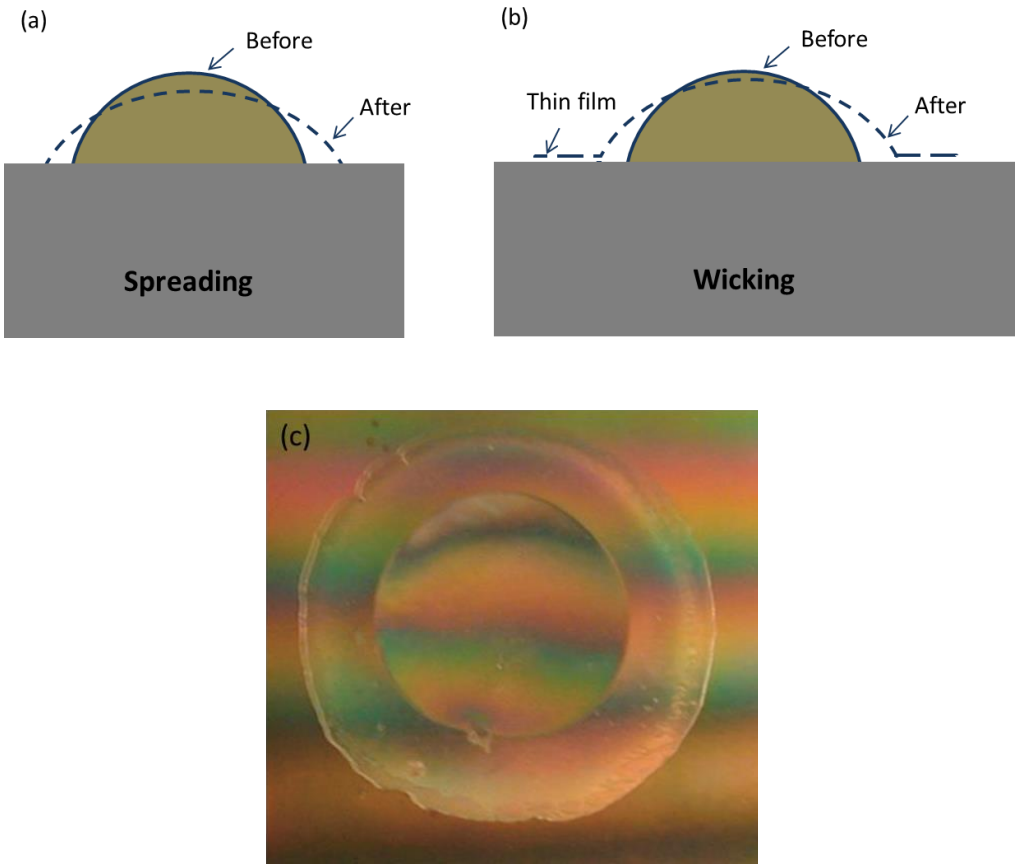

Figure 1.3 Difference between (a) Spreading and (b) Wicking of liquid on a solid surface. (c) Example of wicking of an ethanol drop on a horizontal silicon wafer.[1]

1.2 Motivation

The wicking of fluids on micro-/nano-textured surfaces is a subject that has received much attention because of its many engineering applications, e.g. thermal management for microchips,[2-5] biomedical devices,[6-10] sensors,[11,12] and industrial processes such as oil recovery.[13] The behavior of the droplet radius,[14-16] the velocity of the liquid front,[17] and the dynamic

contact angle[18,19] have been investigated experimentally and theoretically using pure non-volatile liquids.

Although wicking has been shown to take place on both regular[14,15,20,21] and irregular patterns of structures,[22-24] quantitative models have only been proposed on ordered rectangular micropillar arrays due to the ease of fabrication and analysis. The common behavior observed exemplifies the Washburn theory whereby the wicking distance follows a diffusive process such that the impregnated length is proportional to the square root of time.[25] However, there has not been a theory that fully describes the dynamics of wicking without the use of empirical parameters, or a quantitative study on nanostructured surfaces.

1.3 Research Objectives

The objective of this work is to examine quantitatively the dynamics of wicking in regular patterned silicon nanostructured surfaces fabricated using the interference lithography and metal-assisted chemical etching (IL-MACE) techniques. Its dependence on surface geometry and roughness are investigated on isotropic and anisotropic nanostructures. The governing forces are then identified and its limitations are also found. Lastly, this research looks at the wetting stage that happens right before wicking occurs.

1.4 Thesis Organization

The thesis is organized into seven chapters, with Chapter 1 being the introduction. Chapter 2 covers the theoretical background of wetting, the laws that govern it, and literature review on the dynamics of wicking in different micro-/nano-structured surfaces. This chapter will also briefly discuss the initial stage of wetting before wicking happens.

In Chapter 3, details on the experimental procedure are presented. In this section, a versatile fabrication technique called interference lithography and metal-assisted etching (IL-MACE) are utilized to make different regular silicon nanostructures, such as nanopillars and nanofins of various sizes and heights.

Chapter 4 reports on a theoretical study of wicking in nanopillar surfaces. The effect of geometry, represented by the nanopillar height on the dynamics of wicking is examined. An equation for the dynamics of wicking is derived without the use of empirical parameters. This theoretical prediction is compared with experimental results obtained from our samples prepared by the IL-MACE method. The theory is also extended to explain other data published in the literature.

In Chapter 5, an investigation of the geometrical effect of asymmetrical micro-/nano-structures on wicking is reported. Hexagonal arrays of silicon nanofin samples are chosen for the study because of the asymmetrical geometry that allows for an examination of the structural orientation. It is discovered that while viscous drag is present for every form

of nanostructure geometry, form drag is only associated with nanostructure geometries that have flat planes normal to the wicking direction. The drag enhancement factor β is adjusted to take into account the geometrical and orientation parameters of the nanofin structures.

Chapter 6 discusses the early stage of liquid spreading on nanopillar surfaces with different heights and using different drop volume sizes. An energy model is proposed and the dominating force in this regime is identified. In addition, the average energy dissipation per unit area is also calculated. This enables the prediction of the liquid bulk spreading diameter at the end of this stage based on energy consideration.

A final conclusion is made in Chapter 7 to summarize the accomplishments of this project and provide recommendations for future work.

1.5 References

1. C. Ishino, M. Reyssat, E. Reyssat, K. Okumura, and D. Quéré. Wicking within forests of micropillars. *Europhysics Letters* **2007**, 79[5] 56005-56005.

2. C. Zhang and C. H. Hidrovo, "Investigation of Nanopillar Wicking Capabilities for Heat Pipes Applications," pp. 423-437 in ASME 2009 Second Inter. Conf. on Micro/Nanoscale Heat and Mass Transfer

3. C. Ding, P. Bogorzi, M. Sigurdson, C. D. Meinhart, and N. C. MacDonald, "Wicking Optimization for Thermal Cooling," pp. 376 in Solid-State Sensors, Actuators and Microsystems Workshop (Hiltonhead 2010).

4. O. Christopher, L. Qian, L. Li-Anne, Y. Ronggui, Y. C. Lee, M. B. Victor, J. S. Darin, R. J. Nicholas, and C. M. Brian. Thermal performance of a flat polymer heat pipe heat spreader under high acceleration. *J Micromech Microeng* **2012**, 22[4] 045018.

5. S.-W. Kang, S.-H. Tsai, and M.-H. Ko. Metallic micro heat pipe heat spreader fabrication. *Applied Thermal Engineering* **2004**, 24[2–3] 299-309.

6. E. E. Pararas, D. A. Borkholder, and J. T. Borenstein. Microsystems technologies for drug delivery to the inner ear. *Advanced drug delivery reviews* **2012**, 64[14] 1650-1660.

7. D. W. Guillaume and D. DeVries. Improving the pneumatic nebulizer by shaping the discharge of the capillary wick. *Journal of biomedical engineering* **1991**, 13[6] 526-528.

8. C. Liu, M. G. Mauk, R. Hart, X. Qiu, and H. H. Bau. A self-heating cartridge for molecular diagnostics. *Lab on a chip* **2011**, 11[16] 2686-2692.

9. A. C. Araújo, Y. Song, J. Lundeberg, P. L. Ståhl, and H. Brumer. Activated Paper Surfaces for the Rapid Hybridization of DNA through Capillary Transport. *Analytical Chemistry* **2012**, 84[7] 3311-3317.

10. J. Lankelma, Z. Nie, E. Carrilho, and G. M. Whitesides. Paper-Based Analytical Device for Electrochemical Flow-Injection Analysis of Glucose in Urine. *Analytical Chemistry* **2012**, 84[9] 4147-4152.

11. N. Lazarus and G. K. Fedder. Designing a robust high-speed CMOS-MEMS capacitive humidity sensor. *J Micromech Microeng* **2012**, 22[8].

12. P. Peng, L. Summers, A. Rodriguez, and G. Garnier. Colloids engineering and filtration to enhance the sensitivity of paper-based biosensors. *Colloid Surface B* **2011**, 88[1] 271-278.

13. X. J. Feng and L. Jiang. Design and creation of superwetting/antiwetting surfaces. *Adv Mater* **2006**, 18[23] 3063-3078.

14. C. Ishino, M. Reyssat, E. Reyssat, K. Okumura, and D. Quéré. Wicking within forests of micropillars. *Europhysics Letters* **2007**, 79 56005.

15. J. Bico, C. Tordeux, and D. Quéré. Rough wetting. *Europhysics Letters* **2001**, 55[2] 214.

16. J. De Coninck, M. J. de Ruijter, and M. Voué. Dynamics of wetting. *Current Opinion in Colloid & Interface Science* **2001**, 6[1] 49-53.

17. Y.-L. Hung, M.-J. Wang, Y.-C. Liao, and S.-Y. Lin. Initial wetting velocity of droplet impact and spreading: Water on glass and parafilm.

Colloids and Surfaces A: Physicochemical and Engineering Aspects **2011**, 384[1–3] 172-179.

18. B. Lavi and A. Marmur. The exponential power law: partial wetting kinetics and dynamic contact angles. *Colloids and Surfaces A: Physicochemical and Engineering Aspects* **2004**, 250[1–3] 409-414.
19. M. Ramiasa, J. Ralston, R. Fetzer, and R. Sedev. The influence of topography on dynamic wetting. *Advances in Colloid and Interface Science* [0].
20. E. Martines, K. Seunarine, H. Morgan, N. Gadegaard, C. D. W. Wilkinson, and M. O. Riehle. Superhydrophobicity and Superhydrophilicity of Regular Nanopatterns. *Nano Letters* **2005**, 5[10] 2097-2103.
21. C. W. Extrand, S. I. Moon, P. Hall, and D. Schmidt. Superwetting of Structured Surfaces. *Langmuir* **2007**, 23[17] 8882-8890.
22. H. S. Ahn, G. Park, J. Kim, and M. H. Kim. Wicking and Spreading of Water Droplets on Nanotubes. *Langmuir* **2012**, 28[5] 2614-2619.
23. A. Y. Vorobyev and C. Guo. Laser turns silicon superwicking. *Opt. Express* **2010**, 18[7] 6455-6460.
24. A. Y. Vorobyev and C. Guo. Water sprints uphill on glass. *Journal of Applied Physics* **2010**, 108[12] 123512-123514.
25. E. W. Washburn. The Dynamics of Capillary Flow. *Physical Review* **1921**, 17[3] 273-283.

Chapter 2

Literature Review

2.1 Introduction

Wetting and spreading phenomena are extremely interesting because they are in an area where chemistry, physics, and engineering intersect. In a large scale, wetting plays an important role in oil recovery,[1] the efficient deposition of pesticides on plant leaves,[2] drainage of water from highways[3] and the cooling of industrial reactors. In a small scale, wetting solutions have been proposed to solve technological problems in microfluidics, inkjet printing,[4] thermal management,[5] and drug delivery[6] among many others.

In Section 2.2, we will first review the two classical laws on which the theory of wetting and spreading was built: the Young's law, which describes the static state of liquid, solid and vapor when they are in contact; and the Poiseuille's law, which describes the dynamic of fluid flow. A short discussion on the Washburn's law of capillary action[7] will cover the background of the special class of wetting: wicking phenomenon. Another well-known theory on the topic, the Tanner's law,[8] and its difference compared to the other law will be presented. Section 2.3 includes some

literature review of the characteristics of wicking in micro-/nano-structures. This will be followed by some quantitative analyses of dynamics of wicking in regular micropillar silicon surfaces, notably work done by Bico *et al.* [9] and Ishino *et al.*[10]

Literature review of the spreading of liquid at the initial stage when the liquid comes in contact with the solid surface, also known as the onset of wicking, is covered in Section 2.5. Lastly, some key equations, which will be used in subsequent Chapters, such as the capillary length and Reynold's number, are introduced in Section 2.6.

2.2 Basic Laws of Wetting and Spreading

2.2.1 Surface Thermodynamics (Young's Law)

When a droplet of liquid comes in contact with a solid, its behavior is governed by the interfacial forces at the triple phase contact line where solid, liquid and vapor phase intersect. These forces arise from surface tensions γ_{SV}, γ_{SL}, γ_{LV} at the solid-vapor, solid-liquid, and liquid-vapor interfaces, respectively (see Fig, 2.1). At thermal equilibrium, these three forces balance each other and an equilibrium contact angle θ is established at the triple phase contact line. Projecting the liquid-vapor force horizontally using the contact angle θ and establishing a horizontal force balance gives the Young's law as

$$\cos\theta = \frac{\gamma_{SV} - \gamma_{SL}}{\gamma_{LV}} \tag{2.1}$$

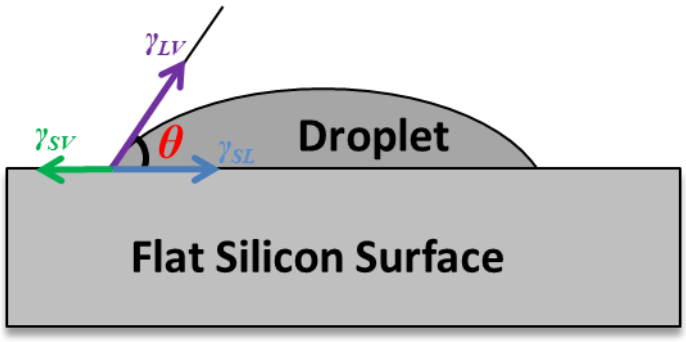

Figure 2.1 A liquid droplet rests on a flat solid surface. The equilibrium contact angle, θ, is the angle formed by a liquid at the three phase boundary where the liquid, vapor, and solid phases intersect.

The equilibrium angle θ is used as a measure of how well a liquid wets the solid substrate. If $\theta < 90^{o}$, the solid is often referred to as being hydrophilic, or "water loving". If $\theta > 90^{o}$ the solid is considered to be hydrophobic or "water hating". There are two special states in the hydrophilic and hydrophobic regimes: complete wetting or super-hydrophillic ($\theta \approx 0^{o}$) and non-wetting or super-hydrophobic ($\theta > 120^{o}$). In the complete wetting case, the liquid spreads completely onto the solid until it forms a continuous film with a microscopic thickness. Super-hydrophobic surfaces on the other hand are extremely difficult to wet, and have applications in self-cleaning,[11] and micro-fuel chip.[12] One example of a super-hydrophobic state in nature is the lotus leaf.

2.2.2 Hagen-Poiseuille's Law

Picking up any fluid mechanics book one will always find Hagen-Poiseuille's law introduced in the first chapters. The law was derived independently by two physicists: Gotthilf Heinrich Ludwig Hagen and Jean Louis Marie Poiseuille. The latter published his results in 1840 and 1846 and for this reason, it is better known as Poiseuille's law.[13]

Poiseuille's law describes a pressure drop in a fluid flowing through a long solid cylindrical pipe (Figure 2.2) and relates it to the dimensional parameters and the properties of the liquid

$$Q = \frac{|\Delta P|\pi R^4}{8\mu L}\ , \qquad (2.2)$$

where Q is the volumetric flow rate of the liquid, $\Delta P = P_1 - P_2$ is the pressure drop at the two ends of the pipe, R is the radius of the pipe, μ is the viscosity of the liquid, and L is the length of the pipe.

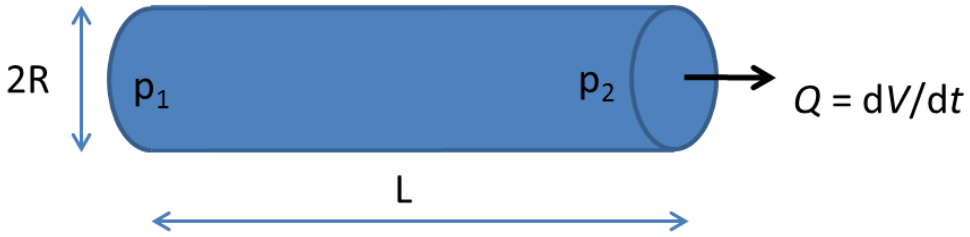

Figure 2.2 Flow of liquid through a cylindrical pipe.

Poiseuille's law was found to be in reasonable agreement with experiments for uniform liquids (called Newtonian fluids) and became a cornerstone for fluid dynamics. It quickly found applications in numerous

fields, especially in the medical community where the study of body fluids was extensive. The physical law can be extended to analyse other classes of flows, such as the Hele-Shaw flows between parallel plates; and broad classes of flows can also be reduced to Poiseuille's law. For instance, Poiseuille's law is the direct result derived from the Navier-Stokes equations for flow in a tube.[13]

2.2.2 Washburn's Law

Although the phenomenon of wetting and spreading pervades everyday life, the first quantitative study of the dynamics of wetting only dated back to 1921 in a study by Edward W. Washburn.[7] Investigating the capillary rise of water in a circular tube of arbitrary shape (Figure 2.3), Washburn was able to come up with a mathematical expression to predict the length of the wetted distance dependent on time.

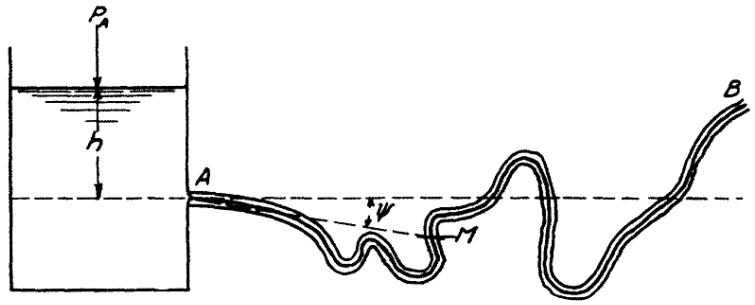

Figure 2.3 Capillary rise in a circular tube of arbitrary shape.[7]

To arrive at the solution, Washburn firstly used Poiseuille's law to express the change in liquid volume at the instance *t* as

$$dV = \frac{\pi \sum P}{8\mu z}(R^4 + 4\varepsilon R^3)dt \ , \qquad (2.3)$$

where *dV* is the volume of the liquid which in the time *dt* flows through any cross-section of the capillary, *z* is the length of the column of liquid in the capillary at the time *t*, μ is the viscosity of the liquid and ε is the coefficient of slip, ΣP is the total effective pressure which is acting to force the liquid along the capillary and *R* is the inner radius of the circular tube.

Washburn believed the capillary rise of liquid was driven by three separate pressures: the atmospheric pressure P_A which is constant; the hydrostatic pressure $P_H = \rho hg - l_s g\rho \sin\psi$ and the capillary pressure $P_C = \frac{2\gamma}{R}\cos\theta$. Note that ρ is the density of the liquid, *h* is the height of the liquid above the center of the capillary opening A (see Figure 2.3), *g* is the standard acceleration of gravity, l_s is the linear distance from the capillary opening point A to the wetting front M, Ψ is the angle between the horizontal line and the line connecting A and M, γ is the surface tension and θ is the contact angle.

Substituting the expressions for P_H and P_C into Eqn. (2.3) and integrating the two sides of the equation, Washburn arrives at the well-known diffusive equation:

$$z = \sqrt{\left(\frac{\gamma}{\mu}\frac{\cos\theta}{2}\right)Rt} \qquad (2.4)$$

The law has been used to explain wetting phenomenon such as capillary rise between flexible walls,[14] wicking in V-grooves surface,[15] or geometries with axial variations[16] and spreading on micro-decorated surfaces.[17] Diffusion-like dynamics behaviors were observed for these studies. It is however important to note that when the gravitational effect becomes significant, the liquid film thickness changes as a function of the height and can affect both the capillary pressure and viscous shear stress. For these reasons, it has been shown that the rise rate greatly deviates from the original equation.[18]

It is worthwhile to mention that besides Washburn's law, there is another well-received theory related to the dynamics of wetting called the Tanner's law.[8] In 1979, Tanner published a paper to investigate the spreading of a small drop of silicone oil on a flat horizontal surface. The author concluded that such spreading was driven by the surface tensions, resisted by the viscous force and proposed a power law of spreading as:

$$z(t) = V^{3/10}\left(\frac{\gamma}{\mu}\right)^{1/10} t^{1/10} \tag{2.5}$$

This model, which holds if the drop evolves slowly and has a shape similar to a spherical cap, has explained many experiments for complete wetting process.[19-21] However, the value of the pre-factor is still controversial and differs according to the model used for contact line motion.[22] Also, there are many wetting phenomena that the theory does not describe, thereby

illustrating that there are other mechanisms influencing or dominating the spreading.[23] For instance, in the case of an inertial spreading of water droplet on a lower energy substrate,[24] or spreading of viscous liquid (1 Pas), the spreading distance was found to follow $z \sim t^{1/2}$, which is similar to Washburn's theory.[24]

Nonetheless, the key difference between Tanner's and Washburn's theories lies in the nature of the wetting. On one hand, Washburn looked at the spreading of liquid inside a tube due to the capillary rise. The liquid penetrating inside the tube is similar to the thin film extending ahead of the liquid bulk in wicking (Figure 1.3(b)). On the other hand, Tanner looked at the spreading phenomenon of the liquid drop on a smooth solid surface where no capillary could be formed on the flat surface and no thin film was observed (Figure 1.3(a)). This thesis focuses on the wicking phenomenon, which is the spreading of the thin film extending ahead of the liquid drop and shares more similarity with Washburn's theory.

2.3 Wicking in Irregular and Regular Micro-/Nano-Structures

In the past decades, the spreading of liquid on a wide range of micro-/nano-textured surfaces has been observed and studied. These studies provided new insights on the influence of roughness on wettability and demonstrated that the wicking characteristics of a substrate can be tuned by changing the properties of the solid surface, such as its chemistry[25,26] or surface topography.[27,28] The former however is beyond the scope of this thesis topic and will not be discussed.

Random structures can be created on the solid surface via various fabrication techniques, such as high intensity nano-/femto-second laser pulses,[29,30] glancing angle deposition,[31] and the anodic oxidation technique.[32] The first method proves to be successful with metals, such as platinum, gold, aluminum and silver or non-metals such as glass. The glancing angle deposition technique was utilized to create random nanowires on silicon and the last method was used to make nanotubes on a glass substrate. Figures 2.4 to 2.6 show the irregular micro-/nano-structures on the surface of the respective fabrication techniques.

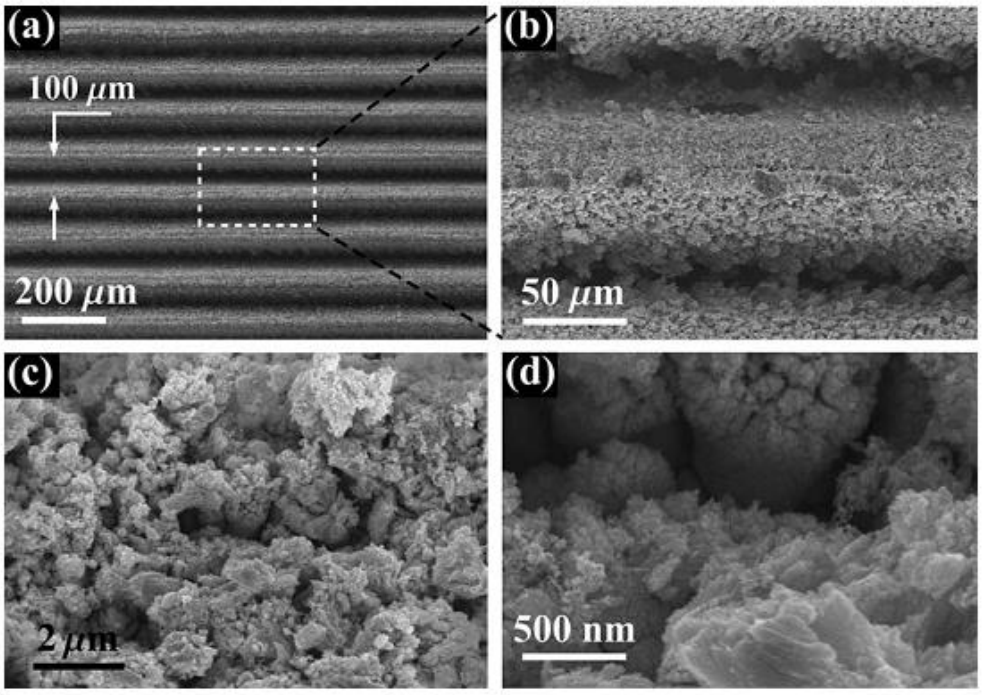

Figure 2.4 Metal surfaces treated by femto-second laser shows (a) the parallel micro-grooves and (b-d) the unintentionally created nanostructures inside.[29]

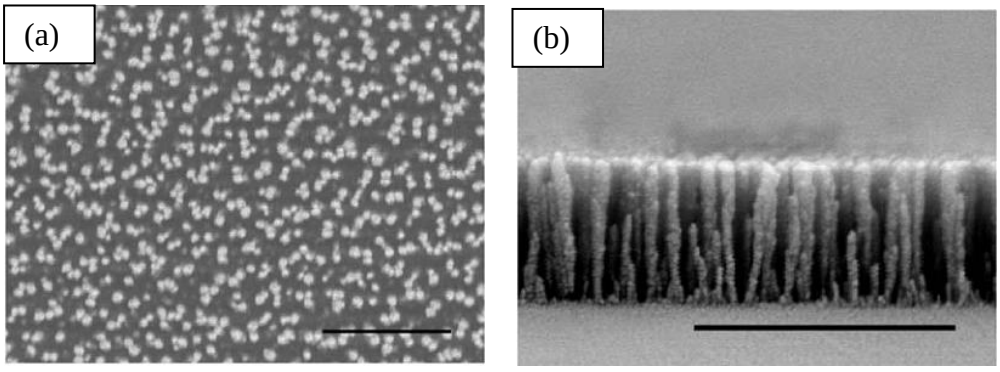

Figure 2.5 (a) Top-view and (b) side-view of silicon nanowires fabricated by the glancing angle deposition technique.[31]

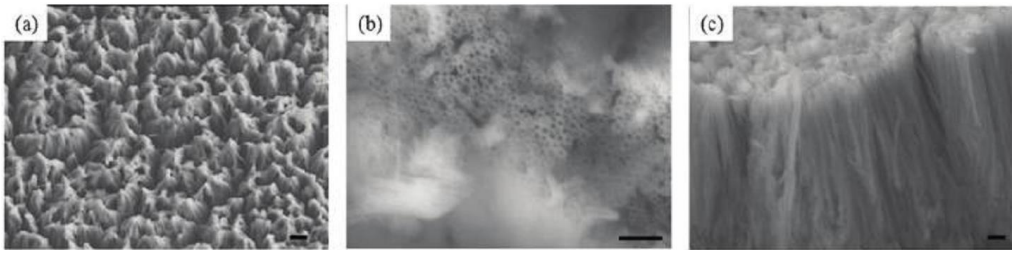

Figure 2.6 Various arrays of nanotubes on glass fabricated by the anodic oxidation technique.[32]

One example of the wicking of liquid in the treated surface is shown in Figure 2.7. Interestingly, prior to the surface treatment, the solid surfaces did not exhibit wicking property. This proves that surface topography has a key role in determining the wicking characteristics of the surface. The conditions for wicking will be discussed further in the next section.

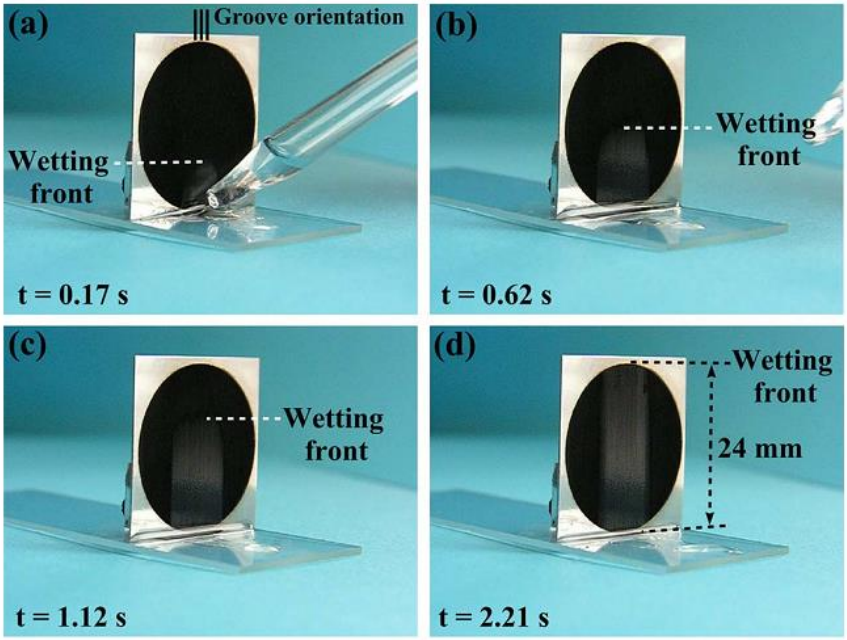

Figure 2.7 Photographs showing methanol running uphill on a vertically standing platinum sample.[29]

The wicking distance follows a diffusion-like process similar to that dictated by Washburn's equation. The wicking distance is plotted against the square root of time (Figure 2.8) and a linear relationship is observed.

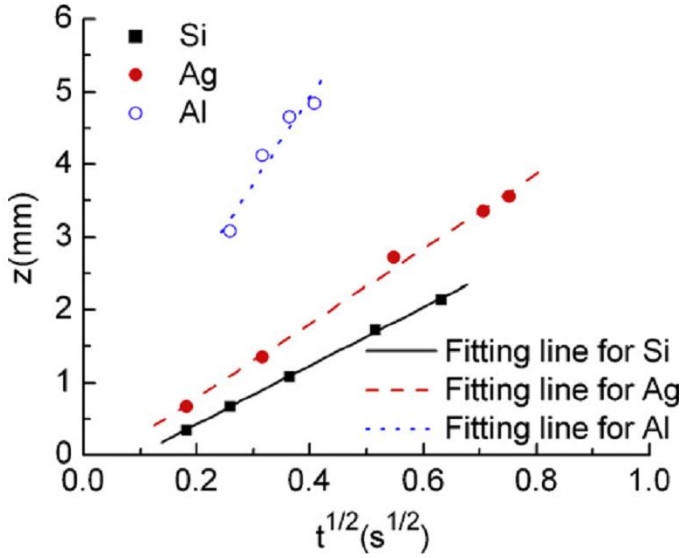

Figure 2.8 Plot of the experimental results of the spreading distance *z* versus the square root of time $t^{1/2}$ of different materials being treated by a nano-second laser. [30]

At the same time, regular structures were also fabricated for the wicking study. The most common structure investigated is the square array of micropillar or micropost due to the ease of fabrication and analysis.[5,33-35] Examples of such structures are illustrated in Figure 2.9.

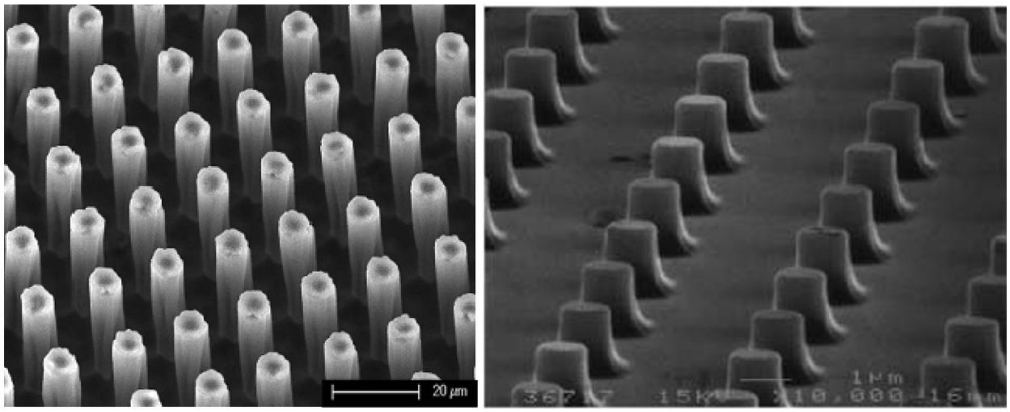

(a) (b)

Figure 2.9 Examples of micropillar structures fabricated for wicking study by (a) inductively coupled plasma etching[36] and (b) micro-imprinting.[37] The latter structure was utilized in Bico *et al.*[9]'s study.

2.4 Dynamics of Wicking

Although random micro-/nano-structures have the advantage of simple fabrication process, quantitative analysis requires well-defined structures. For these reasons, only analyses of the wicking characteristic, i.e. the dependence of the wicking distance on time, on regular microstructures were reported in the literature.

Bico *et al.*[9] examined wicking on silicon micropillars and characterized the dynamics of invasion by balancing the capillary and viscous forces. Bico *et al.*[9] treated the viscous force as that of flow on a free plane without any structures, and then, to take into account the effect of the micropillars, the viscous force was enhanced by an empirical value β. There were a few attempts to express β, such as a work by Hay *et al.*[38] in which the dynamics of wicking was found using a hydraulic diameter approximation.

However, in this model, a fitting parameter, i.e. the tapered angle of the pillars, was introduced in order to fit Bico's data.

In another study, Xiao *et al.*[39] utilized the Brinkman equation for flow through porous media and numerical simulations to arrive at a semianalytical equation describing the dynamics of wicking in silicon micropillars. However, the author claimed that this model only fitted well with the experimental data for a limited range of dimensional parameters. For instance, the estimation of the average driving pressure requires the height-to-period ratios to be greater than 1; and the approximation of permeability requires that the diameter-to-period ratios must be less than 0.5. Even so, the theoretical result for diameter-to-period ratios = 0.348 sample shows deviation from experimental measurement; and the propagation coefficients are underestimated for one third of the tested samples. In addition, while adopting the numerical method, Xiao *et al.*[39]'s model was not capable of explaining the contributions of different terms in the dynamic equation and hence not many insights can be deduced.

As Bico *et al.*[9]'s study includes of background knowledge that the current research work was built upon, it will be discussed in detailed in Section 2.4.1. This will be followed by an introduction to another well-known theory by Ishino *et al.*[10] who were able to come up with mathematical expressions to predict the dynamics of wicking without use of empirical factors.

2.4.1 Bico's Theory

Wicking occurs when the imbibition of liquid thin film further reduces the interfacial energy of the system. When the liquid invades the solid by a small distance *dz*, the change of surface energy can be expressed as

$$dE = (\gamma_{SL} - \gamma_{SV})(r - \phi_s)dz + \gamma_{LV}(1 - \phi_s)dz\,, \tag{2.6}$$

where ϕ_s is the solid fraction that remains dry during wicking, and r is the surface roughness. The expressions for ϕ_s and r vary for different structures and will be introduced in Chapters 4 and 5. The first term on the right hand side of Eqn. (2.6) describes the energy change when the liquid-solid interface replaces the vapor - solid interface. The remaining term describes the increase in energy by the creation of the liquid - vapor interface.

Substitute γ_{SL} and γ_{SV} by applying Young's law (Eqn. (2.1)) to obtain

$$dE = -\gamma_{LV}\cos\theta(r - \phi_s)dz + \gamma_{LV}(1 - \phi_s)dz \tag{2.7}$$

For wicking to happen, the energy change must be negative since lower energy is more favorable. Set $dE < 0$ to obtain the following condition for wicking

$$\cos\theta > \cos\theta_c = \frac{1 - \phi_s}{r - \phi_s}\,, \tag{2.8}$$

where θ is the equilibrium contact angle on a flat surface as dictated by the Young's law and θ_c is defined as the critical angle that can be determined by structural parameters ϕ_s and r. Additionally, by definition, $\phi_s < 1$ and $r \geq 1$, and

thus, $\cos\theta > 0$. In other words, Eqn. (2.8) also implies that the solid surface is hydrophilic ($\theta < 90^o$).

Bico *et al.*[9] also examined the dynamics of wicking and found that the displacement of the wicking front with time followed Washburn's diffusive relation

$$z = (Dt)^{\frac{1}{2}}, \tag{2.9}$$

where D is a coefficient of wicking and is independent of z and t.

Bico *et al.*[9] assumed that wicking in an array of micropillars of height h is equivalent to the Poiseuille's flow of liquid of thickness h on a flat surface. Therefore D can be derived by equating the driving capillary pressure

$$\Delta P_L = \frac{(\gamma_{SL} - \gamma_{SV})(r - \phi_s) + \gamma(1 - \phi_s)}{(1 - \phi_s)h} = \frac{\gamma}{h}\frac{(\cos\theta - \cos\theta_c)}{\cos\theta_c}, \tag{2.10}$$

with the retarding pressure associated with viscous loss

$$\Delta P_V = \frac{3\mu z}{h^2}\frac{dz}{dt} \tag{2.11}$$

The existence of the micropillars on the silicon surface effectively increases the surface areas and in turn, increases the frictional viscous force between fluid and solid. However, Bico *et al.* did not study the effect of the micro-structures on wicking and thus, the extent to which the viscous loss are enhanced is unknown. Instead, to approximately account for this enhancement of viscous loss, the retarding pressure ΔP_V in Eqn. (2.11) is multiplied by a fitting parameter β – which is dubbed as the *viscous enhancement factor*. Balancing Eqns. (2.10) and (2.11) to arrive at

$$zdz = \frac{\gamma h}{3\mu\beta}\frac{\cos\theta - \cos\theta_c}{\cos\theta_c}dt \tag{2.12}$$

Integrating the two sides of Eqn. (2.12) and comparing to Eqn. (2.9) we arrive at

$$D = \frac{2\gamma h}{3\mu\beta}\frac{\cos\theta - \cos\theta_c}{\cos\theta_c} \tag{2.13}$$

From Eqn. (2.13) it can be seen that because β is only a fitting parameter and has to be experimentally determined, the coefficient of wicking, D, cannot be fully predicted with theory alone. Thus it is impossible to understand what role geometrical parameters of the micropillars play as well as how they affect D. Therefore, the wicking kinematics (i.e. distance and velocity) are still unattainable for a fabricated structure.

2.4.2 Ishino's Model

Ishino *et al.*[10] offered another theory of wicking in silicon micropillar surface and came up with equations describing the wicking dynamics without any empirical factors. Ishino *at al.* had to divide the wicking of silicon micropillars into 2 regions, namely, the short pillars (where the height of the pillars was smaller than the period of separation) and long pillars (where the pillars height was larger than the period) regimes. The coefficients of wicking for short pillar (D_1) and long pillar (D_2) regimes are found to be

$$D_1 = \frac{4\pi}{6}\frac{\gamma}{\mu}\frac{h^2 d}{p^2}, \tag{2.14}$$

$$D_2 = \frac{\gamma d}{2\mu}(\ln\frac{2p}{d} - 1.31), \quad (2.15)$$

where *h*, *d* and *p* are the height, diameter and period of the pillars, respectively.

However, the theory is not free of shortcomings. For instance, in the short pillars regime, the effect of viscous dissipation on the pillar walls was deemed insignificant. In the long pillars regime, the viscous force was derived using a questionable approximation that the cut-off distance (the distance beyond which the effect of pillars was negligible) was equal to the period. Consequently, although the proposed equations fitted the experimental data in the second regime, the result in the first regime showed a large deviation from the theory.

2.5 Initial Stage of Wicking

Whenever a drop of liquid is placed on the surface of a substrate, the liquid is expected to evolve until it reaches an equilibrium state. This may require the drop to spread over the surface, remain as a drop, or in some cases to leave the surface. Such process depends on the properties of the surfaces involved.

In a study of wicking in random zircaloy nanotubes, Ahn *et al.*[32] observed that the wetting process is actually separated into two stages (Figure 2.10). The wetting in the first stage is significantly faster than in the second stage. This can be seen as the difference in the slopes in the spreading distance versus time plot.

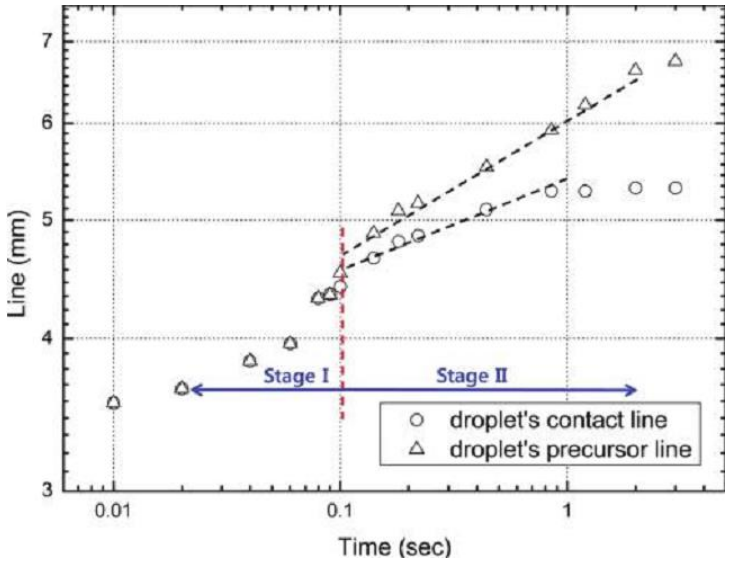

Figure 2.10 Variation of the contact line and precursor rim diameters with respect to time. In Stage I, both the contact line and precursor rim expand at the same velocity, $D \sim t$. However, in Stage II, the contact line stops expanding, and the precursor rim continues to expand at a lower velocity than Stage I, $D \sim t^{1/2}$.[32]

It is noticeable that during the first stage, there is insignificant difference between the spreading of the liquid bulk (denoted as 'contact line' in Fi. 2.10) and the thin film (denoted as 'precursor line'). In the second stage, the thin film expands much quicker while the liquid bulk reaches the maximum and then expands very slowly. A separate work by Zhou *et al.*[30] (Figure 2.11) and others[9,40] showed similar behaviors. One common observation from those studies is that at the second stage, the spreading distance follows the diffusive process $r \sim t^{1/2}$, which is similar to the capillary rise action.

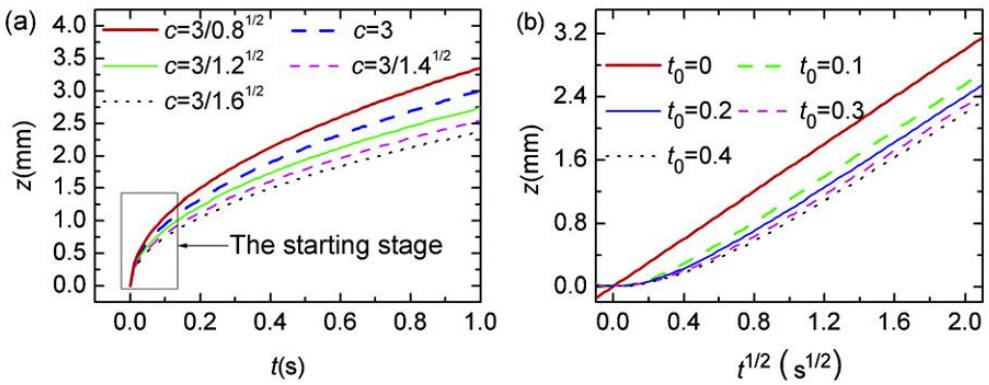

Figure 2.11 Variation of the spreading distance with respect to time. (a) shows the characteristics of the starting stage where the spreading distance increases with time very quickly, while in the following stage the spreading distance increases slowly. (b) shows the influence of the initial spreading time t_0, where clearly once $t > t_0$, the slopes of these lines are almost similar to each other.[30]

The second stage is deemed to be caused by the wicking process because of the appearance of the thin film. However the dynamics of wetting in the first stage is still questionable. In an attempt to explain this behavior, Bico *et al.*[9] suggested that when the condition for wicking is satisfied (Eqn. (2.7)) and once the droplet comes in contact with the solid surface, the drop takes the shape of the spherical cap and expands until it reaches a new effective contact angle θ^* (Figure 2.12), which is calculated as:

$$\cos\theta^* = 1 - \phi_s(1-\cos\theta) \tag{2.16}$$

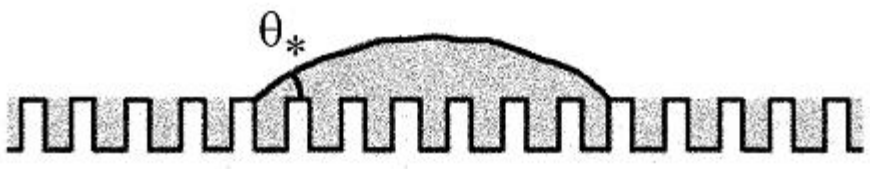

Figure 2.12 Illustration of Bico's theory on the effective contact angle θ^*.[9]

It can easily be seen in this approach that not all structural parameters were taken into account. For instance, while the pillar diameter is considered via the solid fraction Φ_s, the pillar height is ignored. Additionally, it is counter-intuitive that the droplet maintains a constant effective contact angle, given that the thin film's diameter keeps expanding due to wicking. The contact angle of the spherical cap is expected to decrease due to the conservation of mass.

In a more recent work published in 2013, Eddi *et al.*[41] looked at the short time dynamics of drop spreading at very early stages (t in millisecond range) and investigated the effects of droplet initial radius R, the liquid viscosity, and the surface wettability. The authors found that at short time, the radius of the liquid droplet followed the same dynamics for all drop radii R (ranging from 0.37 - 0.82mm) and concluded that the time evolution of the droplet's radius $r(t)$ did not depend on the drop size. The spreading dynamics is characterized by a power law $r(t) \approx Dt^{\alpha}$, where D is an empirical value with no physical meaning and the exponent α is not a constant, instead it slowly decreases from 1 to 0.5 as time increases. The obtained value for α agrees with the experimental data and therefore indicates that the initial dynamics of drop spreading is similar to the coalescence of freely suspended spherical drops. In addition, by testing the spreading for different surfaces with different equilibrium contact angles, Eddi *et al.*[41] found no correlation between the wettability of the surface and the spreading which resembles the initial spreading dynamics of the coalescence of the two drops. Eddi *et al.*[41], however, were not able to explain why the spreading of liquid is analogous to

the coalescence of the two drops and why the application of the coalescence model can provide such accurate prediction.

2.6 Basic Equations

This section introduces some key equations that will be used in subsequent chapters and their physical meanings.

2.6.1 Capillary length

In flows at a very small scale, volume forces are usually less important. A measure of the influence of gravity is the capillary length, which is given as

$$lc = \sqrt{\frac{\gamma}{\rho g}}, \tag{2.17}$$

where ρ is the liquid density, γ is the surface tension of the liquid and g is the standard acceleration of gravity. The capillary length is derived from the Bond number *Bo* which measures the importance of surface tension forces compared to body forces

$$Bo = \sqrt{\frac{\rho g L^2}{\gamma}}, \tag{2.18}$$

where L is the characteristic length and usually taken as the drop radius.

A high Bond number indicates that the system is relatively unaffected by surface tension effects; a low number (typically less than one) indicates that

surface tension dominates. By assuming Bo = 1, the capillary length can be defined as in Eqn. (2.17). The significance of Eqns. (2.17 - 18) is that when the drop size is $L < l_c$ or $Bo < 1$, gravity can be excluded from the analysis, as it gives a small contribution to the flow compared to the surface tension.

For example, the capillary length of water can be computed by introducing its material properties at room temperature ($\rho = 10^3$ kg/m^3, $\gamma = 73\text{x}10^{-3}$N/m, $g = 9.81$m/s^2), giving $l_c \approx 2$mm. This tells us that water drops with a radius less than 2mm will be almost unaffected by gravitational effects and will take a spherical shape. Similarly, for one type of silicone oil ($\rho = 1.065^3$ kg/m^3, $\gamma = 3.399\text{x}10^{-2}$N/m, $g = 9.81$m/s^2) used in this study, $l_c \approx 1.8$ mm.

2.6.2 Reynold's Number

In fluid mechanics, the Reynolds number (*Re*) is a dimensionless number that quantifies the relative importance of inertial forces and viscous forces for given flow conditions. Reynolds number is used to characterize different flow regimes (Figure 2.13). Laminar flow occurs at a very low Reynolds number, i.e. $Re < 1$.

The Reynolds number can be estimated by the expression

$$\mathrm{Re} = \frac{\rho v L}{\mu}, \tag{2.19}$$

where v is the average velocity of the fluid and L is the characteristic linear dimension and is taken as the travelled length of the fluid.

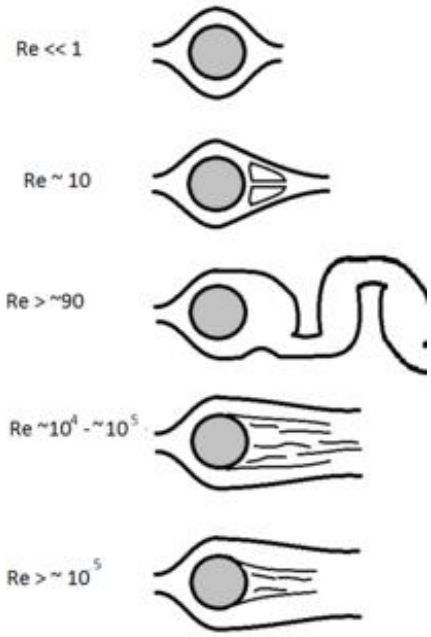

Figure 2.13 Qualitative behaviors of fluid flow over a cylinder depend on different Reynolds number.

The Reynolds number for wicking of silicone oil in this study can be estimated as

$$\mathrm{Re} = \frac{\rho v L}{\mu} \approx \frac{1065 * \frac{10^{-2}}{300} * 10^{-2}}{3.94 * 10^{-2}} \approx 10^{-2},$$

where v can be calculated by the taking the ratio of distance over the time which it takes for the wicking front to reach the end of the sample (please refer to Chapter 4 for the wicking data), and L can be taken as the length of the sample (~1cm).

2.7 Summary

To summarize, this chapter provides a brief background on the physics laws that control wicking. The wicking characteristics on micro-/nano-structures surfaces were introduced. It was found that wicking dynamics follow a diffusion-like process in which the wetting distance is directly proportional to the square root of time. Analytical solutions proposed by various research groups were presented. Lastly, it was noted that the wicking process actually consisted of two stages, in which the latter corresponded to the wicking phenomenon. The dynamics of wetting in the first stage, however, is still unclear.

2.8 References

1. E. Bertrand, D. Bonn, D. Broseta, H. Dobbs, J. O. Indekeu, J. Meunier, K. Ragil, and N. Shahidzadeh. Wetting of alkanes on water. *J Petrol Sci Eng* **2002**, 33[1-3] 217-222.

2. V. Bergeron, D. Bonn, J. Y. Martin, and L. Vovelle. Controlling droplet deposition with polymer additives. *Nature* **2000**, 405[6788] 772-775.

3. N. Shahidzadeh, E. Bertrand, J. P. Dauplait, J. C. Borgotti, P. Vie, and D. Bonn. Effect of wetting on gravity drainage in porous media. *Transport Porous Med* **2003**, 52[2] 213-227.

4. D. Kannangara, H. L. Zhang, and W. Shen. Liquid-paper interactions during liquid drop impact and recoil on paper surfaces. *Colloid Surface A* **2006**, 280[1-3] 203-215.

5. R. Ranjan, A. Patel, S. V. Garimella, and J. Y. Murthy. Wicking and thermal characteristics of micropillared structures for use in passive heat spreaders. *International Journal of Heat and Mass Transfer* **2012**, 55[4] 586-596.

6. J. Roine, M. Murtomaa, M. Myllys, and J. Salonen. Dual-capillary electroencapsulation of mesoporous silicon drug carrier particles for controlled oral drug delivery. *J Electrostat* **2012**, 70[5] 428-437.

7. E. W. Washburn. The Dynamics of Capillary Flow. *Physical Review* **1921**, 17[3] 273-283.

8. L. H. Tanner. The spreading of silicone oil drops on horizontal surfaces. *Journal of Physics D: Applied Physics* **1979**, 12[9] 1473.

9. J. Bico, C. Tordeux, and D. Quéré. Rough wetting. *Europhysics Letters* **2001**, 55[2] 214.

10. C. Ishino, M. Reyssat, E. Reyssat, K. Okumura, and D. Quéré. Wicking within forests of micropillars. *Europhysics Letters* **2007**, 79 56005.

11. R. Fürstner, W. Barthlott, C. Neinhuis, and P. Walzel. Wetting and Self-Cleaning Properties of Artificial Superhydrophobic Surfaces. *Langmuir* **2005**, 21[3] 956-961.

12. Y. Zhiqing, C. Hong, Z. Jide, Z. Dejian, L. Yuejun, Z. Xiaoyuan, L. Song, S. Pu, T. Jianxin, and C. Xin. Preparation and characterization of self-cleaning stable superhydrophobic linear low-density polyethylene. *Science and Technology of Advanced Materials* **2008**, 9[4] 045007.

13. S. P. Sutera and R. Skalak. The History of Poiseuille Law. *Annu Rev Fluid Mech* **1993**, 25 1-19.

14. T. Cambau, J. Bico, and E. Reyssat. Capillary rise between flexible walls. *Europhysics Letters* **2011**, 96[2] 24001.

15. M. S. Khan, D. Kannangara, G. Garnier, and W. Shen. Effect of liquid droplet impact velocity on liquid wicking kinetics in surface V-grooves. *Chemical Engineering Science* **2011**, 66[23] 6120-6127.

16. M. Reyssat, L. Courbin, E. Reyssat, and H. A. Stone. Imbibition in geometries with axial variations. *Journal of Fluid Mechanics* **2008**, 615 335-344.

17. L. Courbin, E. Denieul, E. Dressaire, M. Roper, A. Ajdari, and H. a. Stone. Imbibition by polygonal spreading on microdecorated surfaces. *Nature materials* **2007**, 6[9] 661-664.

18. J. Kim and H. Y. Kim. On the dynamics of capillary imbibition. *J Mech Sci Technol* **2012**, 26[12] 3795-3801.

19. A. M. Cazabat and M. A. C. Stuart. Dynamics of wetting: effects of surface roughness. *The Journal of Physical Chemistry* **1986**, 90[22] 5845-5849.

20. P. Levinson, A. M. Cazabat, M. A. C. Stuart, F. Heslot, and S. Nicolet. The Spreading of Macroscopic Droplets. *Rev Phys Appl* **1988**, 23[6] 1009-1016.

21. M. Ramiasa, J. Ralston, R. Fetzer, and R. Sedev. The influence of topography on dynamic wetting. *Advances in Colloid and Interface Science* [0].

22. J. Eggers and H. A. Stone. Characteristic lengths at moving contact lines for a perfectly wetting fluid: the influence of speed on the dynamic contact angle. *Journal of Fluid Mechanics* **2004**, 505 309-321.

23. D. Bonn, J. Eggers, J. Indekeu, J. Meunier, and E. Rolley. Wetting and spreading. *Rev Mod Phys* **2009**, 81[2] 739-805.

24. A. L. Biance, C. Clanet, and D. Quere. First steps in the spreading of a liquid droplet. *Physical Review E* **2004**, 69[1].

25. K. N. Pandiyaraj and V. Selvarajan. Non-thermal plasma treatment for hydrophilicity improvement of grey cotton fabrics. *Journal of Materials Processing Technology* **2008**, 199[1–3] 130-139.

26. V. Shkolnikov, D. G. Strickland, D. P. Fenning, and J. G. Santiago. Design and fabrication of porous polymer wick structures. *Sensors and Actuators B: Chemical* **2010**, 150[2] 556-563.

27. A. Y. Vorobyev and C. Guo. Laser turns silicon superwicking. *Opt. Express* **2010**, 18[7] 6455-6460.

28. A. Y. Vorobyev and C. Guo. Water sprints uphill on glass. *Journal of Applied Physics* **2010**, 108[12] 123512-123514.

29. A. Y. Vorobyev and C. L. Guo. Metal pumps liquid uphill. *Applied Physics Letters* **2009**, 94[22].

30. M. Zhou, J. Yu, J. Li, B. Wu, and W. Zhang. Wetting induced fluid spread on structured surfaces at micro scale. *Applied Surface Science* **2012**, 258[19] 7596-7600.

31. J. G. Fan and Y. P. Zhao. Spreading of a water droplet on a vertically aligned Si nanorod array surface. *Applied Physics Letters* **2007**, 90[1] 013102-013102.

32. H. S. Ahn, G. Park, J. Kim, and M. H. Kim. Wicking and Spreading of Water Droplets on Nanotubes. *Langmuir* **2012**, 28[5] 2614-2619.

33. L. Courbin, J. C. Bird, M. Reyssat, and H. A. Stone. Dynamics of wetting: from inertial spreading to viscous imbibition. *Journal of Physics: Condensed Matter* **2009**, 21[46].

34. X. Li, L. Mao, and X. Ma. Dynamic Behavior of Water Droplet Impact on Microtextured Surfaces: The Effect of Geometrical Parameters on Anisotropic Wetting and the Maximum Spreading Diameter. *Langmuir* **2012**, 29[4] 1129-1138.

35. C. Zhang and C. H. Hidrovo, "Investigation of Nanopillar Wicking Capabilities for Heat Pipes Applications," pp. 423-437 in ASME 2009 Second Inter. Conf. on Micro/Nanoscale Heat and Mass Transfer

36. D. Changsong, G. Soni, P. Bozorgi, B. D. Piorek, C. D. Meinhart, and N. C. MacDonald. A Flat Heat Pipe Architecture Based on Nanostructured Titania. *J Microelectromech S* **2010**, 19[4] 878-884.

37. C. Marzolin, S. P. Smith, M. Prentiss, and G. M. Whitesides. Fabrication of glass microstructures by micro-molding of sol-gel precursors. *Adv Mater* **1998**, 10[8] 571-+.

38. K. M. Hay, M. I. Dragila, and J. Liburdy. Theoretical model for the wetting of a rough surface. *Journal of Colloid and Interface Science* **2008**, 325[2] 472-477.

39. R. Xiao, R. Enright, and E. N. Wang. Prediction and optimization of liquid propagation in micropillar arrays. *Langmuir : the ACS journal of surfaces and colloids* **2010**, 26[19] 15070-15075.

40. M. Harth and D. W. Schubert. Simple Approach for Spreading Dynamics of Polymeric Fluids. *Macromol Chem Phys* **2012**, 213[6] 654-665.

41. A. Eddi, K. G. Winkels, and J. H. Snoeijer. Short time dynamics of viscous drop spreading. *Physics of Fluids* **2013**, 25[1].

Chapter 3

Experimental Techniques

3.1 Introduction

Recently, colleagues in our research group have discovered a simple method of creating ordered arrays of silicon nanopillars and nanofins over large areas (~ 1 cm^2) by means of interference lithography and metal-assisted chemical etching (IL-MACE) method.[1,2] To the best of the author's knowledge, there has not been a report in the literature studying wicking on fins structure or pillar structure at nanometer scale. Furthermore, the fabrication method is versatile in creating nanostructures of different sizes. Dimensional parameters such as nanostructure width, length and spacing can be adjusted in the lithography step, while the nanostructure height can be easily varied by controlling the etching time.

This chapter will describe the experimental procedures employed in the preparation and characterization of these silicon nanostructures. Firstly, the procedures for wafer cleaning will firstly be highlighted. Then the experimental details of various fabrication processes will be discussed. These processes include thermal oxidation, spin-coating of photo-resist, Lloyd's

Mirror interference lithography, plasma-assisted etching, thermal evaporation, lift-off, and metal-assisted chemical etching. Finally, the details of the structural characterization techniques such as scanning electron microscopy (SEM) and contact angle goniometry used in this work will be presented.

3.2 Wafer Cleaning

Two-inch p-type silicon wafers were used as substrates in this work. The wafers were of <100> orientation and had a resistivity of 8 – 12 Ωcm. In order to eliminate the samples from possible impurities, such as organic or ionic contaminants, the wafers were cleaned by immersing them into cleaning solutions RCA I and II before all fabrication steps.

The wafers were firstly cleaned using RCA I solution consisting of hydrogen peroxide (H_2O_2), ammonium hydroxide (NH_4OH) and de-ionized (DI) water in the proportion of 1:1:5 by volume. This oxidizes organic films and complexes Group I, II metals as well as other metals, such as Au, Ag, Cu, Ni, Zn, Cd, Co and Cr.[31] The mixture was heated to 80 – 90 °C on a hot plate before the wafers were immersed in the solution for 15 min. The RCA I solution slowly dissolved the thin native oxide layer on silicon and continuously grew a new oxide layer by re-oxidation. This combination of etching and re-oxidation dislodged particles from the wafer surface.[3] The wafers were then rinsed in DI water with a nitrogen (N_2) bubbler for another 10 – 15 min.

In contrast to RCA I, RCA II solution consisting of hydrochloric acid (HCl), H_2O_2 and DI water in the proportion of 1:1:6 by volume. Again, the solution was then heated to 80 – 90°C on a hot plate before the wafers were immersed in the solution for 15 min. This solution removed alkalis ions and cations (ionic and heavy metal atomic contaminants) like Fe^{3+}, Al^{3+}, and Mg^{2+} which formed insoluble hydroxides in basic solutions of RCA I.[1] The wafers were then rinsed with DI water with a nitrogen bubbler for another 10 – 15 min.

The hydrogen peroxides in the RCA I and RCA II cleaning solution caused the surfaces of the wafers to be coated with a thin layer of silicon dioxide of 1-2 nm thick due to its high oxidizing nature. To remove this layer of oxide prior to subsequent processing, the wafers were immersed in a diluted hydrofluoric acid (10% HF) for around 20 sec. Then, the wafers were rinsed in DI water with a nitrogen bubbler for 10 min to remove the remaining HF acid. The wafers were blown dry using a nitrogen gun and were ready for the next processing step.

Note that wafers that exhibited scratches or visible surface defects after the entire cleaning process would not be used in order to maintain the experimental reproducibility and comparability.

3.3 Interference Lithography

The positive photoresist (Ultra-i 123) was coated onto the substrate by the spin coating method. Prior to the spinning, a few droplets of photoresist were applied on the surface of the silicon substrate until it was sufficient to cover the entire surface area of a 10 mm x 10 mm. The spin coating method is basically a two-step process. The first step consists of a 6 sec spinning interval at 3000 rotations per minute (rpm) to ensure that the deposited photoresist spreads out uniformly over the entire surface of the sample. The second step consists of a 50 sec spin coating at 6000 rpm, which determines the final thickness of the photoresist. In this study, the resist thickness was calibrated by a surface profiler to ensure the consistency in the thickness of the resist layer. This was then followed by a soft-bake process on a hot plate at 90°C for 1 min. The purpose of the soft-bake process is to evaporate excess solvent within the photoresist, as well as improve the adhesion of the photoresist to the sample.

After the spin coating process, interference lithography was used to define the pattern on the photoresist layer. This process was carried out by the Lloyd's mirror setup with a 325 nm helium-cadmium (He-Cd) continuous wave laser as the light source. The He-Cd laser offered a long coherence length at a mid UV wavelength and at a lower cost than other available options, such as an excimer laser. The Lloyd's mirror setup allowed the laser to cover a large area of substrate within a short period of time. No mask was required as it was based on the principle of constructive and destructive

interferences, which produced the periodic fringes. Figure 3.1 shows the experimental setup for this Lloyd's mirror interferometer. The laser beam was directed at the spatial filter which allowed noise to be removed away from the beam to provide a clean Gaussian profile. As the Gaussian beam expanded, it changed threefold: the intensity of the beam decreased, the diameter of the beam increased, and the radius of the phase front increased. Firstly, lowering the intensity required an increase in exposure time to maintain the required dosage, but this did not cause any issues due to the inherent stability of the system. Besides, because of the Gaussian intensity profile, increasing the beam diameter meant that the intensity would become more uniform over the exposed area. Finally, the increase in diameter made the beam more closely resemble a plane wave over the exposure area.

An aluminum square mirror was used to reflect the beam to the substrate because of its enhanced UV reflectivity compared to other metals, and for its essentially constant reflectivity over a broad range of angles. Though a higher reflectivity could be obtained with a dielectric mirror, the variation in the reflectivity with angle could be significant. The intersection point of the mirror and wafer was aligned with the axis of a rotation stage, and this allowed for easy variation of the gratings' spatial period. Because the center of the mirror/substrate assembly remained on the optical axis, further alignment of the optics was unnecessary. This feature was a distinct advantage over the Mach-Zehnder style system, where changing the period required physically moving and re-aligning the two arms of the interferometer.[4] The light from the original beam would interfere with the light reflected off the

mirror to form a standing wave pattern, which could be recorded in the photoresist. This generated a pattern of lines in the photoresist layer with a period equal to $\frac{\lambda}{2}\sin\alpha$, where λ is the wavelength of the laser source, and α is the in-plane rotation angle. As such, for a 1 μm period, the stage was rotated at an angle $\alpha \approx 10^{o}$. In this experiment, the laser power was fixed at 6 mW and one single exposure lasted for 60 sec.

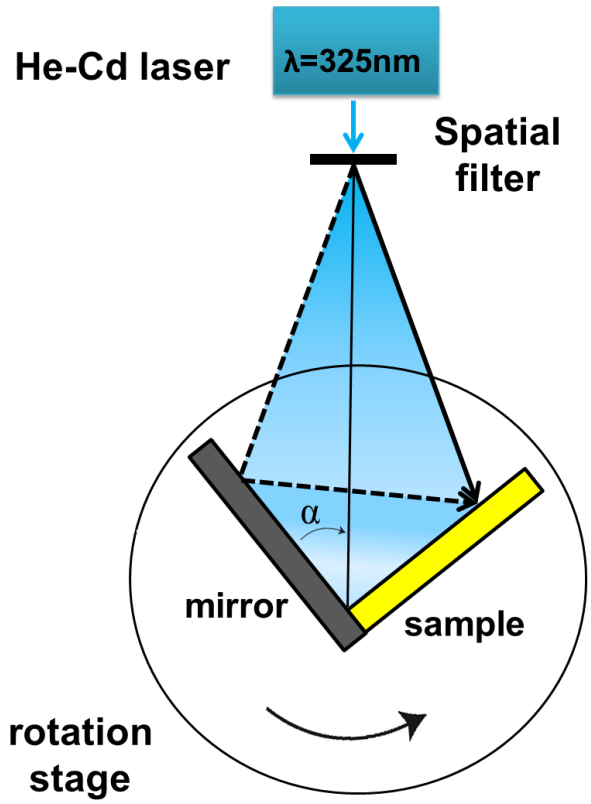

Figure 3.1 Experimental setup for Lloyd's Mirror Interference Lithography. The He-Cd laser beam is directed at the spatial filter and either reaches the sample surface directly (the solid arrow) or reflects off the mirror before reaching the sample surface (the dotted arrow). Periodic fringes are produced based on the principle of constructive and destructive waves.

Different structures could be created by carefully aligning the samples for a second exposure. For instance, the nanopillar structure was made with a double exposure technique. For the second exposure, the sample was tilted by an angle of exactly 90^o with respect to the first exposure. Ideally, after the second exposure, the resulting photoresist dots would have a square shape. However because the sharp corners at the junction of the two exposures were over-exposed compared to other areas, the corners of the square became rounded. After developing and etching, the nanopillar structures with rounded edge would be obtained. Similarly, the nanofins could be made by rotating the sample by an acute angle ($< 90^o$) for the second exposure.

After the exposure, the samples were subjected to a post-exposure bake on hot plate at 110^oC to complete the photo-reaction initiated during exposure as well as improve photoresist adhesion to the substrate. Development of the exposed photo-resist was performed using the Microposit MF CD-26 developer. The exposed samples were immersed in the developer for ~60 sec and rinsed in DI water. The final step was blowing the samples with N_2 gas to drive off any remaining solutions and clean the sample surface.

3.4 Plasma-Assisted Etching

After the lithography step, there might be a certain amount of photoresist residues left on the silicon surface. Those residues, if existing, would act as an unwanted masking layer for the etching process later and

would therefore need to be removed. An oxygen plasma etching process was utilized for this purpose.

The samples were put inside a chamber, where low-pressure glow-discharge plasma was introduced. Oxygen was chosen as the reactive gas for a selective etching process. The ions produced in oxygen plasma can convert the photoresist into carbon dioxide and water vapor – which could easily be flushed away by the vacuum pump. To avoid over-etching of the photoresists dots, three parameters needed to be controlled carefully: the plasma power, the oxygen flow rate and the duration of etching.

One side effect of this process was that the exposed silicon surface was also oxidized. Therefore after this experiment, the samples were dipped inside 10% HF solution to remove the silicon dioxide layer. After being rinsed in DI water, the samples were ready for the next processing step.

3.5 Thermal Evaporation

To prepare the sample for the catalytic etching in the next step, a thin layer of gold (Au) was coated on the sample surface through a thermal evaporation process. The deposition material was placed on a filament or a metal plate where it was heated until fusion by a strong electrical current. Once the required evaporation temperature (1000 ~ 2000 °C) is reached, the evaporated material was then condensed on the substrate under high-vacuum

condition (pressure ~ 10^{-6} Torr). This technique was simple and appropriate for depositing metals and compounds with low fusion temperature (such as Al, Ag, and Au etc…). Typical materials used for the crucible to contain the deposition material (i.e. the source) are metals with very high melting point so that vapor pressure is practically zero at the evaporation temperature. A few examples are tantalum (Ta), molybdenum (Mo) and tungsten (W). A schematic drawing of the deposition equipment used in the laboratory is shown in Figure 3.2.

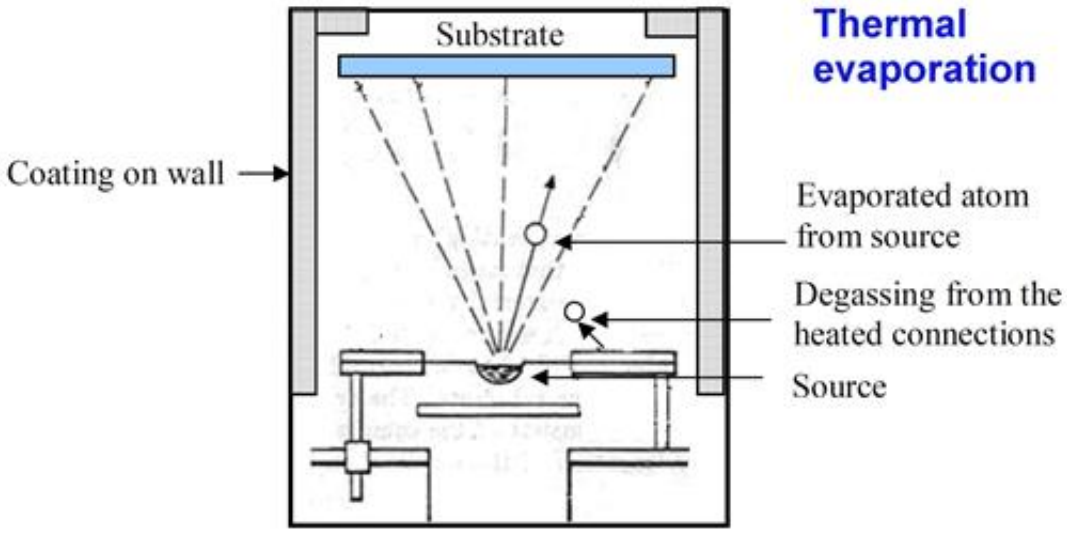

Figure 3.2 Schematic drawing of a typical Thermal Evaporator.

3.6 Metal-assisted Chemical Etching

A lift-off process was performed prior to the metal-assisted chemical etching (MACE) of silicon to transfer the pattern on the resist layer down to the metal film layer. This was carried out by dipping the samples in a beaker

containing acetone solution at room temperature with the help of ultrasonic agitation. An illustration of the lift-off process is shown in Figure 3.3.

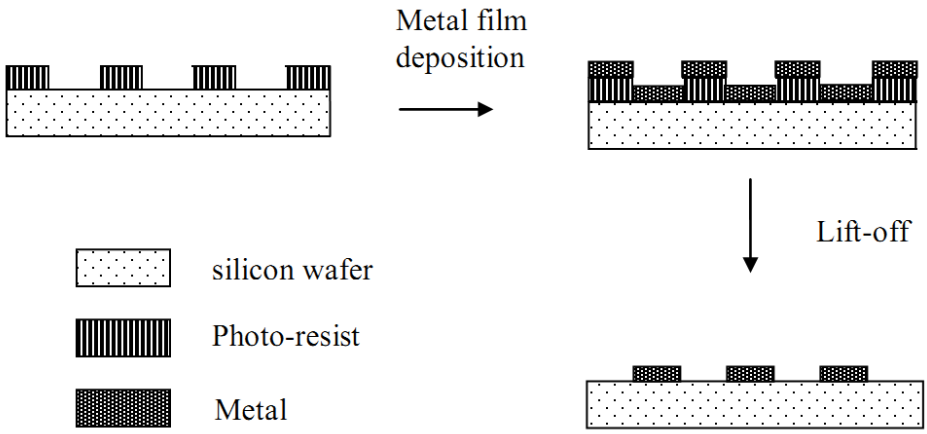

Figure 3.3 Before etching, the samples went through the lift-off process to transfer the negative image of the photoresist to the metal film.

Finally after lift-off, MACE process was carried out to selectively etch the silicon substrate covered by a noble metal (Au, Ag or Pt) layer. It was well-accepted that the silicon in direct contact with an isolated noble metal particle would be etched at a much faster rate compared to the silicon surface that was exposed directly to the etching solution,[5] allowing the fabrication of silicon nanostructures with high aspect ratios.

The MACE solution was created by mixing of H_2O, HF and H_2O_2 at room temperature. Two important parameters controlling the etching process are the concentration of HF and H_2O_2 and the etching duration. The concentrations of HF and H_2O_2 were optimized to be 4.6 Molar (M) and 0.44 M, respectively. The duration of etching varied depending on the required etch

depths. Normally, etching lasted for 5 to 30 min. Note that for this study, the noble metal used was gold (Au). The sample was then rinsed in DI water for 10 min to remove the remaining HF and H_2O_2 and was blown dry by a N_2 gun.

The chemistry behind the metal-assisted chemical etching was still an ongoing discussion. Various possible cathode and anode reactions were proposed in the literature to describe the etching process.[6] The most accepted chemical reaction sequence consisted of two continuous reaction stages as illustrated in Figure 3.4.[7]

Firstly, the positive holes were injected into silicon through the metal/silicon interface and the positive holes were attracted to the noble metal particles because its electrochemical potential was more positive than the valence band of silicon. These oxidation–reduction reactions would result in the precipitation of the noble metal particles and the oxidization of the silicon. The silicon dioxide would then react with HF to form a soluble silicon complex and water. The chemical reactions which occurred in this stage could be described as below

$$Au^+ + e^- \rightarrow Au,$$

$$Si + H_2O \rightarrow SiO_2 + 4H^+ + 4e^-,$$

$$SiO_2 + 6HF \rightarrow H_2SiF_6 + 2H_2O$$

During the second stage, the noble metal particles would not participate chemically in the reaction. The oxidant in this stage was H_2O_2 and the chemical reactions can be written as

$$H_2O_2 + 2H^+ + 2e^- \rightarrow 2H_2O$$

$$Si + H_2O \rightarrow SiO_2 + 4H^+ + 4e^-$$

$$SiO_2 + 6HF \rightarrow H_2SiF_6 + 2H_2O$$

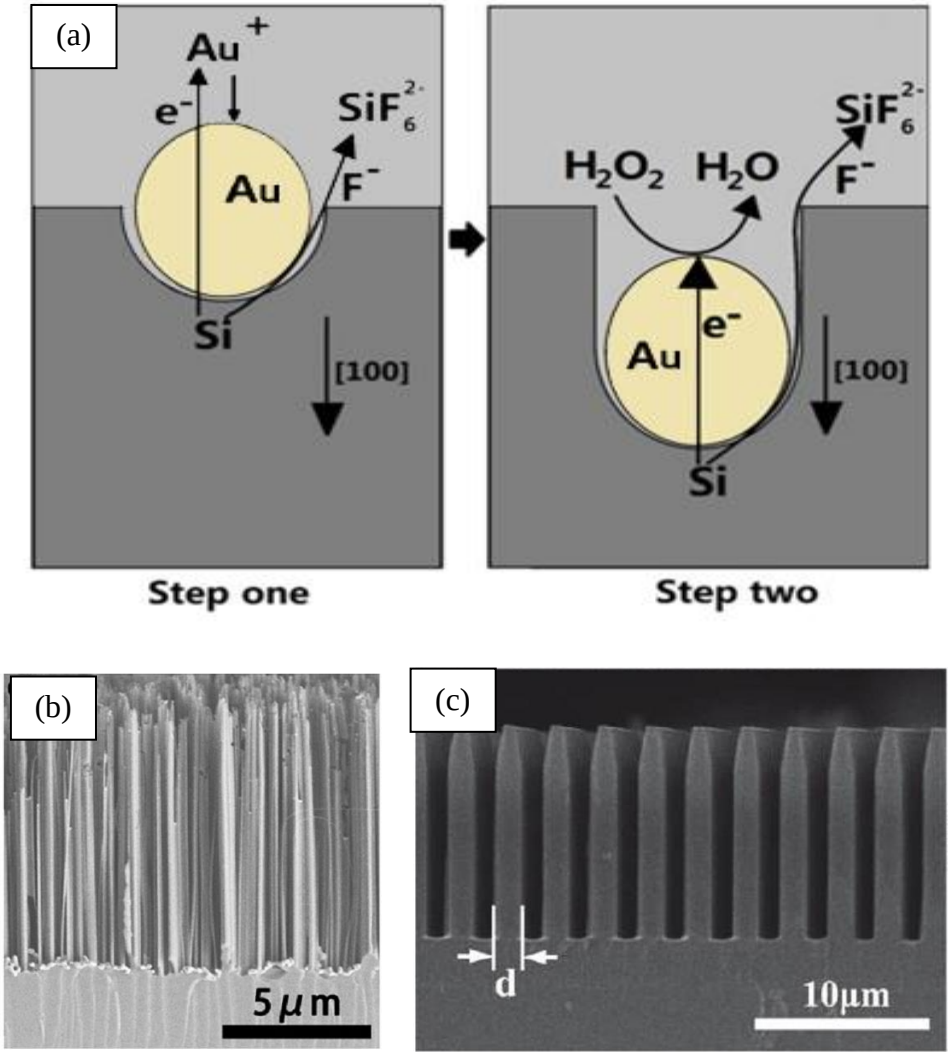

Figure 3.4 (a) Schematic drawing of the two stages of the metal-assisted chemical etching process. The location of the metal catalyst determines the regularity of the nanostructures. (b) Precipated Ag particles produced a forest of randomly located nanowires.[7] (c) Regular array of nanowires was obtained with carefully designed Au particles by means of photolithography. [8]

After the etching, the metal catalyst layer was removed by different methods depending on the type of metal. Gold can be removed by a gold

etchant solution which consists of KI and I_2. Silver can be taken away by 30% HNO_3 solution. Finally the samples were rinsed with DI water to dislodge the residues on the surface.

The profile and regularity of the obtained nanostructures are determined by the shape and the distribution of the catalyst metal on the silicon surface. In Liu *et al.*[7]'s study, the sample was immersed in an aqueous solution containing 10% HF and 0.02M $AgNO_3$. This allowed the Ag particles to precipitate randomly on the silicon surface. Consequently, the MACE process resulted in a forest of irregular nanowires as seen in Figure 3.4 (b). In another study, Pan *et al.*[8] used photolithography to pattern the silicon surface with a square array of photoresist dots with sizes and spacing determined by the lithography masks. This enabled the author to precisely deposit the gold particles at designed locations. Consequently, the MACE process resulted in a regular silicon wires as seen in Figure 3.4 (c). The purpose of the IL step in Section 3.3 is similar to Pan *et al.*[8]'s lithography step in terms of controlling the location of the metal catalyst. Combining IL and MACE techniques, Choi *et al.*[9] was able to fabricate regular silicon nanowires and nanofins array over large areas. The IL step to fabricate these two types of nanostructures will be discussed in detail in Chapters 4 & 5.

3.7 Characterization Techniques

3.7.1 Scanning Electron Microscopy (SEM)

A scanning electron microscope (SEM) is a type of electron microscope that produces images of a sample by scanning it with a focused beam of electrons (see Figure 3.5). Electrons from a thermionic, or field-emission cathode are accelerated through a voltage difference between cathode and anode (from as low as 0.1 keV to as high as 30 keV). The smallest beam size at the virtual source with a diameter in the order of 10 ~ 50 μm for thermionic emission, and a diameter of 10 ~ 100 nm for field emission guns, is de-magnified by a two or three stage electron lens system so that an electron probe of diameter 1 ~ 10 nm is formed at the specimen surface.

Primary electrons after striking the sample surface generate backscattered electrons (BSE), secondary electrons (SE) and Auger electrons (AE) (see Figure 3.6). BSE are electrons generated from elastic collisions and lose only a small fraction of their original energy, but undergo large angle deflection. SE are in-elastically scattered electrons that lose much of their original energy and generally have energy less than 50 eV. SE and BSE are usually collected, amplified and detected with a scintillator-photomultiplier detector. SE provide information on surface topography, and are also used in voltage contrast imaging. BSE, on the other hand, provide information on topography and material. Lastly, AE carry information of the chemical composition of thin film and are usually used for surface analysis.

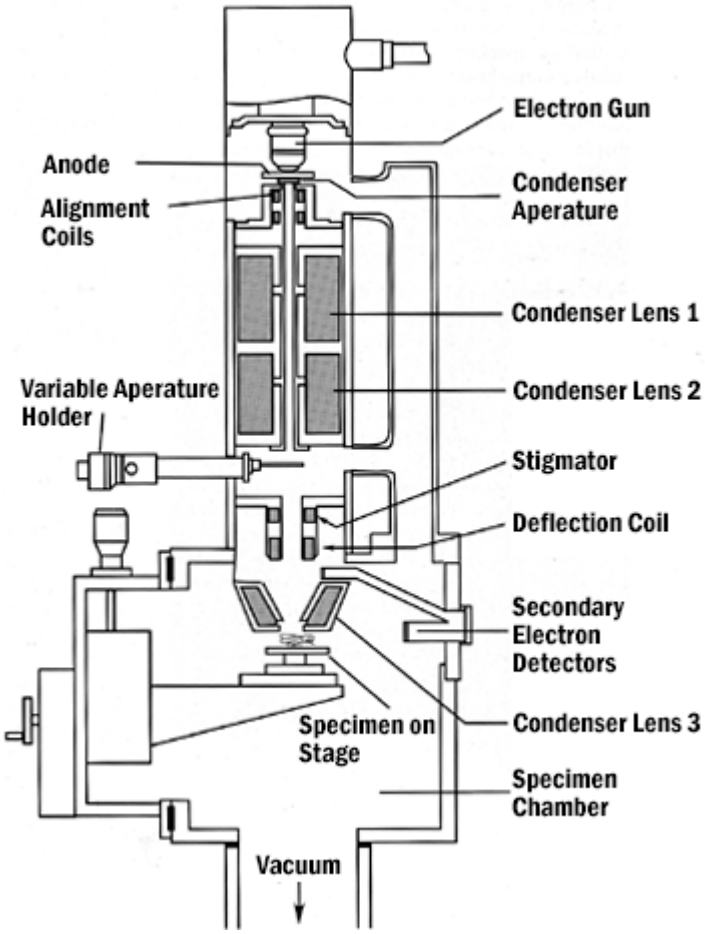

Figure 3.5 Schematic diagram of the Scanning Electron Microscopy.[b]

Separate detectors are required for secondary and backscattered electrons. To produce images, these electron signals are measured as a function of primary beam position while the beam is scanned in a raster pattern over the sample. Interaction of the primary beam with the sample creates an excitation volume, in which electrons are scattered through elastic and inelastic scattering. The SEM resolution depends on the smallest electron probe spot achievable, while the signal-to-noise ratio is determined by the electron probe current, which decreases with probe spot size. Therefore, electron optics in SEM are designed to achieve the smallest electron spot with

[b] Image courtesy from http://cmrf.research.uiowa.edu/scanning-electron-microscopy

the maximum current. The SEM analysis in this work was performed using NOVA NanoSEM 230. An accelerating voltage of 5 keV with a working distance of 5 mm was normally used for conducting samples.

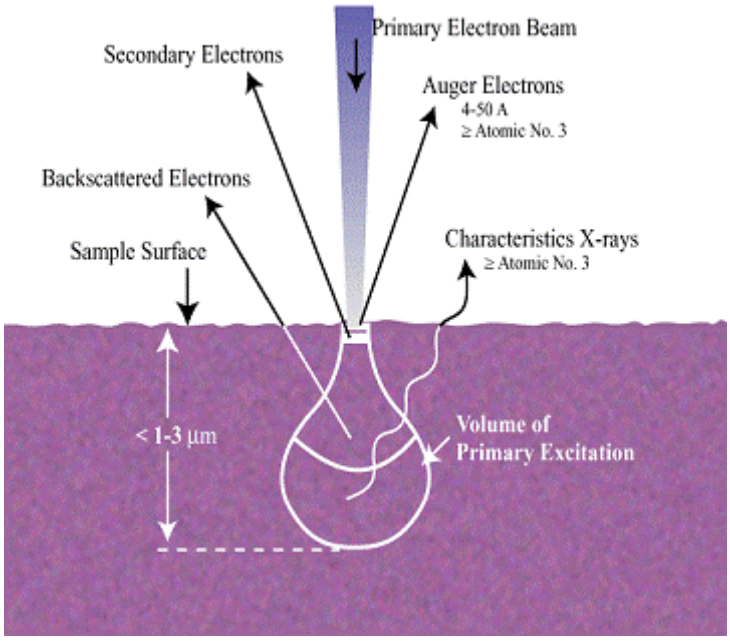

Figure 3.6 Interaction between primary electrons and the sample surface generates backscattered electrons, secondary electrons, Auger electrons and X-rays.[c]

3.7.2 Contact Angle Measurements

The contact angle measurement system consists of a droplet volume control and an optical system to capture the profile of the droplet formed on the surface. The contact angle analysis in this experiment was performed using the VCA Optima System. It consists of a sample stage, a volume controlled syringe/needle and a CCD camera as shown in Figure 3.7. To measure the

[c] Image courtesy from http://cc.usst.edu.cn/Able.acc2.web/Template/office/9f756afe-9a18-4195-8524-f0761f492e37.html

contact angle, a droplet of known volume is dispensed on the sample surface via the needle. The shape profile of the liquid drop is then captured by the CCD camera. The contact angle is then obtained by calculating the slope of the tangent to the liquid drop at the triple phase contact line where the liquid, solid and vapor phase intersect.

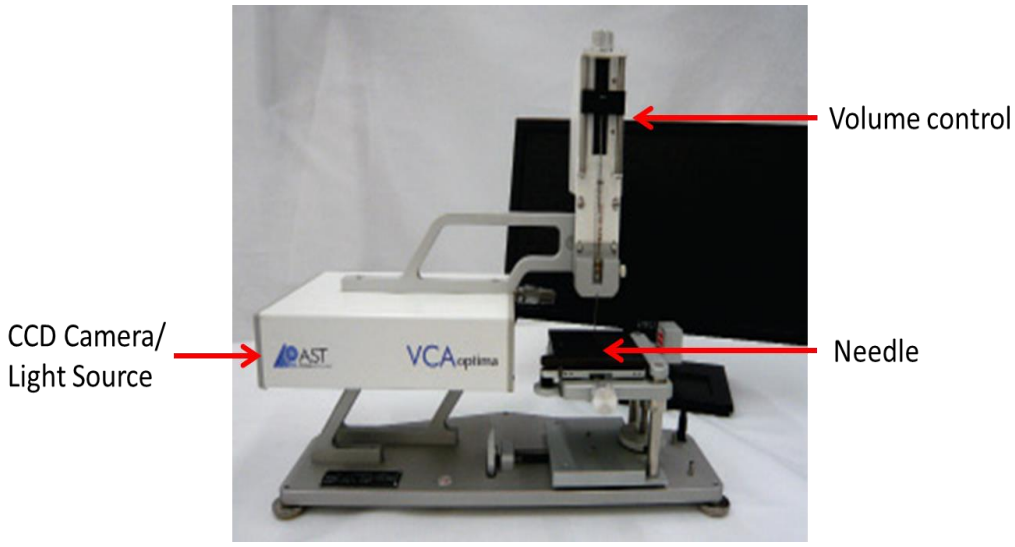

Figure 3.7 The setup of a contact angle measurement experiment. The VCA Optima system consists of a stage, a volume control syringe/needle and a CCD camera.

3.7.3 High Speed Camera Experiment

To capture the wicking action, a high speed camera modeled Photron Fastcam SA5 was utilized. The camera had the capacity to measure up to 775,000 frames per second (fps). Considering the relatively slow speed of wicking, the camera was setup to operate at 1000 fps. After the images had been captured, the wicking distance with respect to time was extracted using

the integrated software Photron Fastcam Viewer. The experiment setup for the wicking dynamics is illustrated in Figure 3.8.

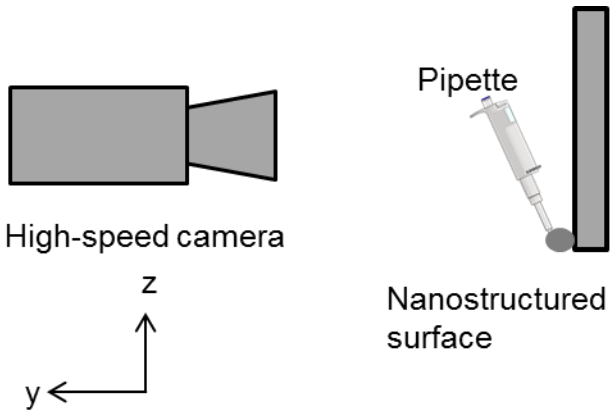

Figure 3.8 Illustration of the high-speed camera experiment. A nanostructured sample was placed vertically on a flat surface and a droplet was delivered to the bottom of the sample. The whole wicking action was captured by the camera.

3.8 References

1. M. K. Dawood, T. H. Liew, P. Lianto, M. H. Hong, S. Tripathy, J. T. L. Thong, and W. K. Choi. Interference lithographically defined and catalytically etched, large-area silicon nanocones from nanowires. *Nanotechnology* **2010**, 21[20] 205305.

2. T. A. Savas, M. L. Schattenburg, J. M. Carter, and H. I. Smith, "Large-area achromatic interferometric lithography for 100 nm period gratings and grids," pp. 4167-4170. **Vol. 14**.

3. S. Wolf and R. N. Tauber, "Silicon Processing for the VLSI Era, vol. 1: Process Technology," 2 ed. **Vol. 1**. Lattice Press.

4. M. E. Walsh, "On the design of lithographic interferometers and their application," pp. 300. in Dept. of Electrical Engineering and Computer Science, **Vol. Ph. D.** Massachusetts Institute of Technology, 2004.

5. Z. Huang, H. Fang, and J. Zhu. Fabrication of Silicon Nanowire Arrays with Controlled Diameter, Length, and Density. *Adv Mater* **2007**, 19[5] 744-748.

6. Z. Huang, N. Geyer, P. Werner, J. de Boor, and U. Gösele. Metal-Assisted Chemical Etching of Silicon: A Review. *Adv Mater* **2011**, 23[2] 285-308.

7. K. Liu, S. Qu, X. Zhang, and Z. Wang. Anisotropic characteristics and morphological control of silicon nanowires fabricated by metal-assisted chemical etching. *Journal of Materials Science* **2013**, 48[4] 1755-1762.

8. C. Pan, Z. Luo, C. Xu, J. Luo, R. Liang, G. Zhu, W. Wu, W. Guo, X. Yan, J. Xu, Z. L. Wang, and J. Zhu. Wafer-Scale High-Throughput Ordered Arrays of Si and Coaxial Si/Si1–xGex Wires: Fabrication, Characterization, and Photovoltaic Application. *ACS Nano* **2011**, 5[8] 6629-6636.

9. W. K. Choi, T. H. Liew, M. K. Dawood, H. I. Smith, C. V. Thompson, and M. H. Hong. Synthesis of Silicon Nanowires and Nanofin Arrays Using Interference Lithography and Catalytic Etching. *Nano Letters* **2008**, 8[11] 3799-3802.

Chapter 4

Results and Discussion I: Wicking in silicon nanopillars surface

4.1 Introduction

The ultimate goal of this study is to achieve control of the wicking flow by tailoring the surface topography. In other words, we aim to identify crucial structural parameters that can control the wicking speed. The results would have tremendous potential for the development of engineering applications based on the wicking phenomenon.

Designing micro-/nano-structures for this purpose requires careful considerations of multiple effects that each structural parameter introduces. For instance, on one hand, the existence of micro-/nano-structures increases the wetting property of the surface,[1,2] and in turn amplifies the capillary force that drives the liquid up against gravity. On the other hand, it enhances the frictional viscous force because of the larger contact surface created. It is therefore interesting to investigate the influence of structural geometry on the balance between the capillary driving force and the frictional viscous force.

Although wicking has been shown to take place on both regular[1,3-7] and irregular[8-10] patterns of structures, quantitative models have only been proposed on ordered array surfaces, with the rectangular arrangement of micropillar arrays as the most studied system due to the ease of fabrication and analysis. However, the best of the author's knowledge, these studies involves either fitting parameters or rough approximation that lead to inaccurate results. For instance, Bico *et al.*[3] examined the dynamics of wicking and found that the displacement of the wicking front with time followed Washburn's diffusive relation. However in his study, the coefficient of wicking D contained fitting parameter β (see Eqn. (2.13) which hinders prediction of the wicking dynamics. Ishino *et al.*[4] offered another theory on wicking and came up with equations describing the wicking dynamics without any empirical factors. However, the theory contains many problems as pointed out in Chapter 2.

Therefore, the objective of this chapter is to derive an analytical solution for the viscous enhancement factor β which does not require any fitting parameters. The subject of this study of wicking will firstly be the ordered array of nanopillars with varying height. As mentioned in Chapter 3, the height of the nanopillars can be easily varied by controlling the etching time. The theory is validated with experimental data and also extended to fit other data published in the literature.

Success in describing the wicking dynamics in simple structures such as nanopillars will form a basis to tackle more complicated structures such as the nanofins in Chapter 5.

4.2 Experimental Details

The process flow for the synthesis of silicon nanopillars using IL-MACE technique is illustrated in Figure 4.1(a). P-type (100) silicon wafers were first cleaned by standard RCA I and RCA II processes and dipped in 10% HF for 1 min to remove the native oxide layer. The silicon wafers were then coated with positive photoresist (Ultra-i 123) of approximate 300 nm thickness, and cured at 90°C for 90 sec. The photoresist was exposed using a Lloyd's mirror-type interference lithography with a He-Cd laser source at a wavelength λ of 325 nm.[11] Two perpendicular exposures of 60 sec duration each were then performed on the samples and followed by a post-bake at 110^{o}C for 60 sec. The exposed photoresist was removed using a photoresist developer (Microposit MF CD-26). After this step, circular photoresist dots were formed on the silicon sample surface. The samples were then subjected to an oxygen plasma etching (power of 200 W, oxygen pressure of 0.2 mbar, etching time of 30 to 45 sec) to remove the residual photoresist on the surface. Au was thermally evaporated on the substrate to a thickness of ~30 nm, at a pressure of ~10^{-6} Torr. The photoresist dots were lifted off by ultrasonic bath in acetone for 15-20 min, leaving an Au mesh on the silicon surface. Finally, the samples were etched in a solution of H_2O, HF and H_2O_2 at room

temperature for 5-30 min. The concentrations of HF and H_2O_2 were 4.6 M and 0.44 M, respectively. The samples were then immersed in a standard Au etchant for 5 min to remove Au and dried by N_2 gun after being rinsed in DI water.

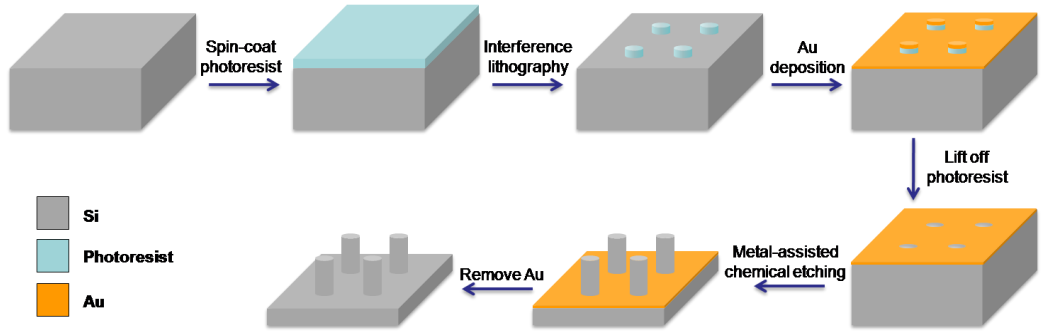

(a)

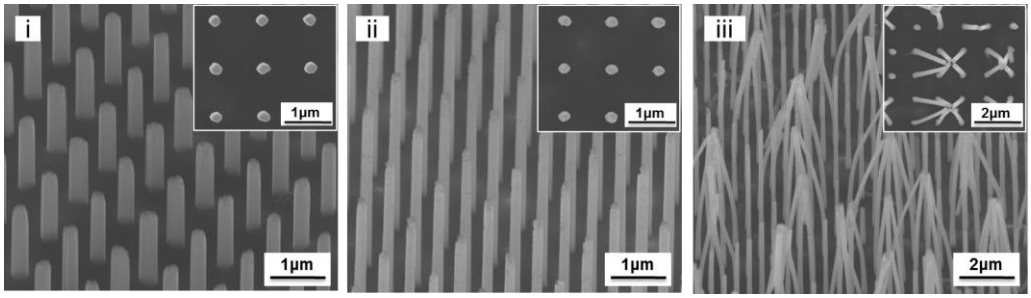

(b)

Figure 4.1 (a) Schematic diagram of the process flow to fabricate Si nanopillars using the IL-MACE method, (b) SEM images of Si nanopillars at a height of (i) ~2 μm, (ii) ~4 μm and (iii) ~7 μm, respectively. The insets are top-view SEM images of the respective samples. All samples in Figure 1(b) have the same period of 1μm.

Figure 4.1(b) shows the SEM images of silicon nanopillars at various heights. All samples were fabricated with exactly the same conditions except etching duration (5 to 30 min) that resulted in different heights. Nanopillars from samples etched for 5 to 20 min are perfectly straight (Figure 4.1(b) i, ii). However as the nanopillar become taller (~7 μm), the high aspect ratio reduces its mechanical strength significantly such that capillary forces can

overcome the elastic forces and cause sufficient permanent deformation/clumping of the nanopillars (Figure 4.1(b) iii).[12]

To examine the wicking characteristics, the samples were placed vertically and an 1μl droplet of deionized water or silicone oil (HIVAC F-4) was deposited at the bottom of the sample surface. The wicking process was recorded using a high speed camera at a speed of 1000 frames per second and the videos were analyzed with the embedded Photron FASTCAM Viewer software.

4.3 Theoretical Model

4.3.1 Approximation of a Unit Cell of Nanopillar

Firstly, to simplify the derivation, we approximate the flow of fluid through the nanopillars as a flow through open nanochannels that are of the same height, h, and length, $(d+s)$, as a unit cell of nanopillar. Note that d and s are the pillar diameter and the distance between two neighboring pillars, respectively (see Figure 4.2).

A unit cell of nanochannel (Figure 4.2.b) can hold the same volume of fluid as a unit cell of nanopillar (Figure 4.2.a) and thus the width of the nanochannel, w, can be calculated as

$$w = \frac{\left[(d+s)^2 - \frac{\pi}{4}d^2\right]h}{(d+s)h} = \frac{(4-\pi)d^2 + 8ds + 4s^2}{4(d+s)} \tag{4.1}$$

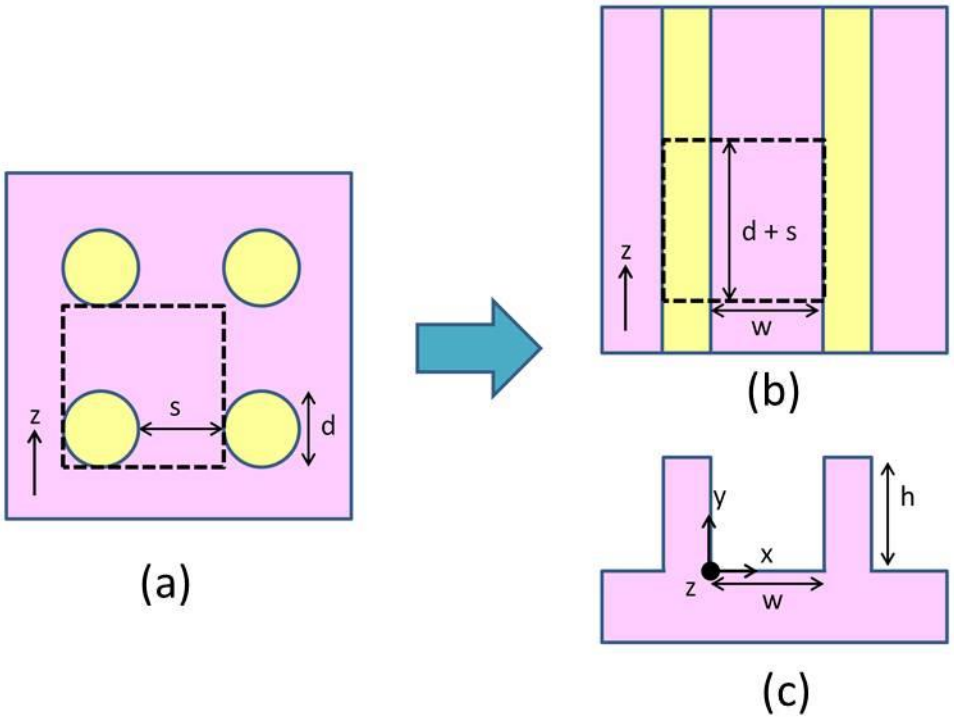

Figure 4.2 Approximating a unit cell (indicated by dashed black rectangle) of nanopillars as a unit cell of nanochannels that holds the same volume of liquid. (a) shows the top view of a unit cell of nanopillars while (b) and (c) show the top view and side view of a nanochannel. The yellow regions indicate the top of the nanostructures at $y = h$, which remain dry throughout the wicking process, while the violet regions indicate the bottom regions at $y = 0$. Flow of fluid is in the z-direction in all cases.

The justification of the seemingly 'rough' estimation above can be shown in the COMSOL simulation of the flow inside an array of nanopillars (Figure 4.3.a). It can be deduced from this figure that the liquid in between the 2 adjacent nanopillars in the flow direction (z-direction) is stagnant, i.e. has zero velocity. This stagnancy is analogous to a wake behind an obstruction (in this case, a nanopillar) in the flow direction where there is no fluid, or the fluid

cannot move. Most of the liquid is only able to sweep through the space between the two adjacent rows made of nanopillars in *z*-direction. These rows of nanopillars can therefore be seen to act like solid walls which encompass the fluid, and effectively make the flow through nanopillars arrays similar to that inside a nanochannel (Figure 4.3.b).

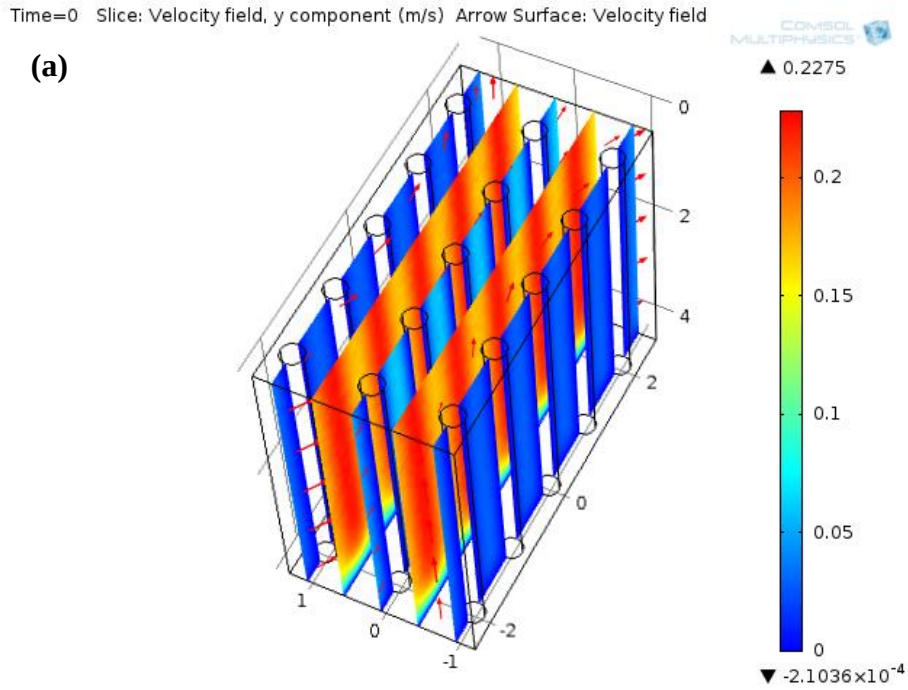

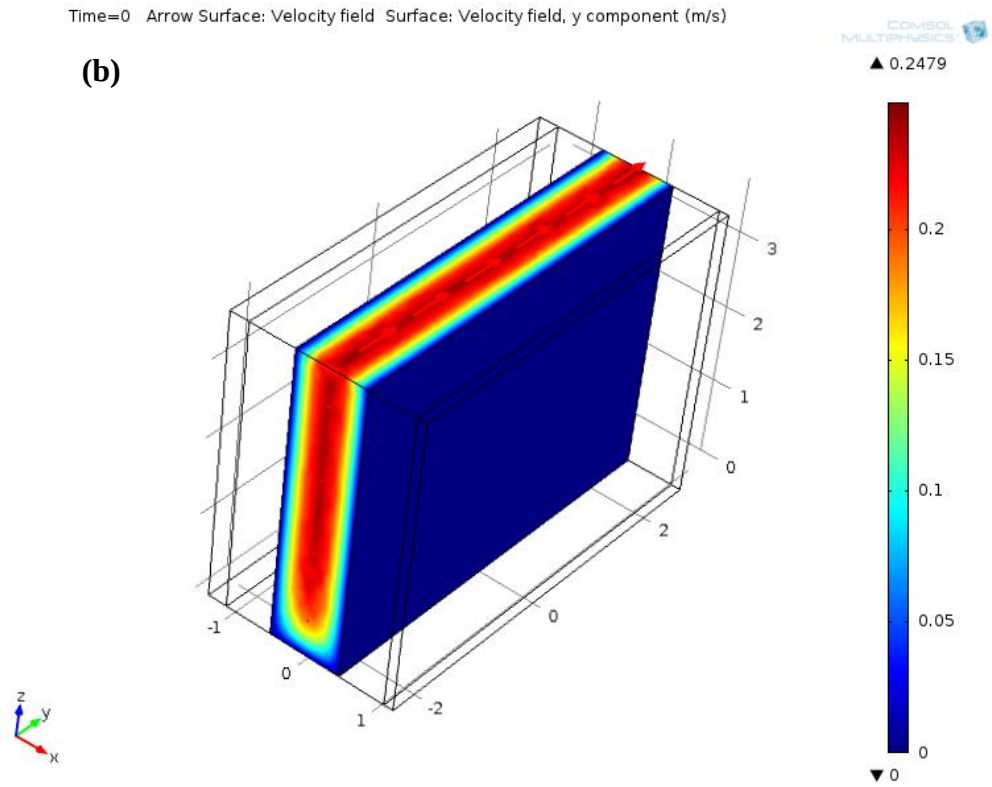

Figure 4.3 Simulation of flow inside (a) an array of nanopillars and (b) a nanochannel. The color bar represents the magnitude of velocity where blue stands for zero velocity (stagnant flow) and red means maximum velocity. The red arrows indicate the flow direction. The parameters used in the simulation are: d = 0.3 µm, s = 0.7 µm, h = 4 µm and w = 0.93 µm. Similar results were obtained by varying h from 1 to 7 µm.

4.3.2 Navier-Stokes Equations

The set of basic governing equations that describe all viscous and heat conducting fluid motion are called the Navier-Stokes (N-S) equations. These equations arise from applying Newton's second law to fluid motion, together with the assumption that the fluid stress is the sum of a diffusing viscous term (proportional to the gradient of velocity) and a pressure term. The N-S equations include a set of 3 nonlinear partial differential equations for flow in 3-dimensional structures

$$\rho\frac{DU_x}{Dt} = -\frac{\partial P}{\partial x} + \rho g_x + \mu\left(\frac{\partial^2 U_x}{\partial x^2} + \frac{\partial^2 U_x}{\partial y^2} + \frac{\partial^2 U_x}{\partial z^2}\right), \tag{4.2}$$

$$\rho\frac{DU_y}{Dt} = -\frac{\partial P}{\partial y} + \rho g_y + \mu\left(\frac{\partial^2 U_y}{\partial x^2} + \frac{\partial^2 U_y}{\partial y^2} + \frac{\partial^2 U_y}{\partial z^2}\right), \tag{4.3}$$

$$\rho\frac{DU_z}{Dt} = -\frac{\partial P}{\partial z} + \rho g_z + \mu\left(\frac{\partial^2 U_z}{\partial x^2} + \frac{\partial^2 U_z}{\partial y^2} + \frac{\partial^2 U_z}{\partial z^2}\right), \tag{4.4}$$

where U_x, U_y, U_z are the components of velocity in x, y and z-direction respectively. Similarly, g_x, g_y, g_z are the components of gravitational force in the 3 dimensions. P indicates the driving pressure acting on the fluid. The substantial derivative D/Dt can be expressed in Cartesian coordinates as

$$\frac{D}{Dt} = U_x\frac{\partial}{\partial x} + U_y\frac{\partial}{\partial y} + U_z\frac{\partial}{\partial z} + \frac{\partial}{\partial t} \tag{4.5}$$

The N-S equations are often combined with the differential continuity equation, which is a direct interpretation from the conservation of mass theory, to fully describe the kinematics of fluidic flow. This continuity equation can be expressed as

$$\frac{D\rho}{Dt} + \rho\left(\frac{\partial U_x}{\partial x} + \frac{\partial U_y}{\partial x} + \frac{\partial U_z}{\partial x}\right) = 0 \tag{4.6}$$

For incompressible flow in z-direction through an open channel such as that shown in Figure 4.2.c, the density of the fluid particle does not change as it travels, therefore

$$\frac{D\rho}{Dt} = \frac{\partial\rho}{\partial x} + U_x\frac{\partial\rho}{\partial x} + U_y\frac{\partial\rho}{\partial y} + U_z\frac{\partial\rho}{\partial z} = 0 \tag{4.7}$$

Note that to deduce Eqn. (4.7) we have assumed that the fluids used in this study (water and silicone oil) are incompressible liquids. In reality, all fluids are compressible to some extent. In other words, the density varies with changes in pressure or temperature. In this situation, the changes in pressure and room temperature are sufficiently small that the changes in density are negligible. For instance, according to the Handbook of Tables for Applied Engineering ScienceBolz[13] and the silicone oil data sheet[14], compressibility of water and silicon oil at room temperature is 0.0046% and less than 0.1% respectively. Therefore, in this study the flows can be modeled as incompressible flows.

Eqn. (4.6) can then be simplified as

$$\frac{\partial U_x}{\partial x} + \frac{\partial U_y}{\partial y} + \frac{\partial U_z}{\partial z} = 0 \qquad (4.8)$$

To summarize, for the wicking flow in this research, there is a set of four equations (Eqns. (4.2), (4.3), (4.4), and (4.8)) with four unknowns U_x, U_y, U_z and P. With appropriate boundary and initial conditions, the equations can be solved.

Going back to our case, gravitational effect can be ignored at the scale of the experiment.[7,15,16] Indeed the capillary length of the liquids in the experiment, which is the characteristic length beyond which gravity becomes important, is much larger than the dimension of the nanostructures (see Chapter 2.6).

Furthermore, as the streamlines are parallel to the nanochannels walls in the *z*-direction, only the *z*-component of the velocity will be non-zero (i.e. $U_x = U_y = 0$). The continuity equation (Eqn. (4.8)) becomes

$$\frac{\partial U_z}{\partial z} = 0 \tag{4.9}$$

This shows that U_z only has x- and y-component, i.e. $U_z = U(x,y)$. The substantial derivative DU_z/Dt can then be described as

$$\frac{DU_z}{Dt} = U_x \frac{\partial U_z}{\partial x} + U_y \frac{\partial U_z}{\partial y} + U_z \frac{\partial U_z}{\partial z} + \frac{\partial U_z}{\partial t} = 0 \times \frac{\partial U_z}{\partial x} + 0 \times \frac{\partial U_z}{\partial y} + U_z \times 0 + 0 = 0 \tag{4.10}$$

Note that here we have assumed that $\frac{\partial U_z}{\partial t} = 0$. This is justifiable because the flow of liquid in wicking can be classified as a laminar flow. As it can be seen from Section 2.6.2, the Reynolds number of the wicking flow is very small and indeed satisfies the condition for laminar flow ($Re < 1$). In other words, the fluid flows at low velocities in parallel layers, with no disruption between the layers. There are also no cross currents perpendicular to the direction of flow, or eddies or swirls of fluids like turbulent flow. Thus we can ignore the time-derivative term, i.e. $\frac{\partial U_z}{\partial t} = 0$.

With the above reasoning, the N-S equation (Eqn. (4.4)) can be reduced to

$$0 = -\frac{\partial P}{\partial z} + 0 + \mu(0 + \frac{\partial^2 U_z}{\partial y^2} + \frac{\partial^2 U_z}{\partial z^2}) \tag{4.11}$$

or

$$\frac{\partial P}{\mu \partial z} = (\frac{\partial^2 U_z}{\partial y^2} + \frac{\partial^2 U_z}{\partial z^2}) \tag{4.12}$$

Finally, a straightforward integration gives us a simplified version of the N-S equation as

$$-\frac{\Delta P}{\mu z} = \left(\frac{\partial^2 U}{\partial x^2} + \frac{\partial^2 U}{\partial y^2} \right) \tag{4.13}$$

Also note that we have implied here that all the testing liquids are Newtonian fluids whose viscosities constant and independent on the velocity of flow. Water is generally accepted to be Newtonian[17], and so is silicon oil[18]. In fact, silicone oil shows extremely good shear stability and retains their original viscosity characteristics as they are not affected by mechanical working. Furthermore, there was no chemical reaction occurred between the solid (silicon) and liquid (water and silicone oil). According to the datasheet, silicone fluid is nearly chemically inert and is virtually unaffected by 10% alkaline aqueous solutions or 30% acid aqueous solutions at ambient temperatures.

4.3.3 Solving Navier-Stokes Equation

To solve the simplified N-S equation, we start by considering a similar but simpler second-ordered partial differential equation (Laplace's equation) below

$$\frac{\partial^2 U}{\partial x^2} + \frac{\partial^2 U}{\partial y^2} = 0 \tag{4.14}$$

As shown above, the velocity U is independent of x and y and thus allows us to use the Method of Separation of Variables. We expect

$$U(x,y) = X(x)Y(y) \tag{4.15}$$

Substituting Eqn. (4.15) into Eqn. (4.14) to obtain:

$$X'' - \psi X = 0 \tag{4.16}$$

$$Y'' + \psi Y = 0 \tag{4.17}$$

where $\psi = \frac{X''}{X} = -\frac{Y''}{Y}$ and therefore must be a constant. Eqn. (4.16) can be solved with appropriate boundary conditions for no-slip flow at the sidewalls of the nanochannels (Figure 4.5):

$$U(0,y) = X(0) = 0 \tag{4.18}$$

$$U(w,y) = X(w) = 0 \tag{4.19}$$

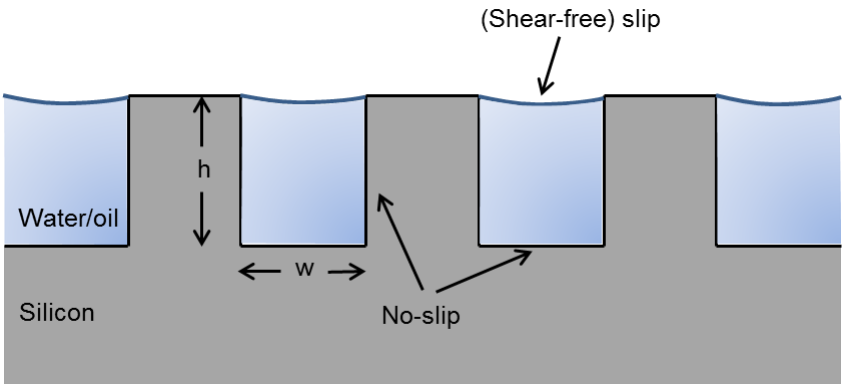

Figure 4.5 Boundary conditions for wicking flow on silicon nanopillars surface.

The justifications of the boundary conditions are as follow. For the case of zero-viscosity fluid, there is no restriction on the tangential component of the velocity, and thus the fluid can slip parallel to the solid surface.[19]

However, for the case of real fluid, the viscosity stress prevents any slipping of the fluid relative to the solid surface. This implies that at the solid surface, the velocity of the liquid is zero such as indicated in Eqns. (4.18-19). The theory of surface tension also supports this boundary condition. Since the solid is hydrophilic, the adhesive force (solid-liquid) is stronger than the cohesive force (liquid-liquid). Therefore, the liquid molecules in contact with the solid are held by the solid molecules, which reduce the velocity of flow to zero.

The non-trivial solution for *X(x)* is

$$X(x) = \sum_{m=0}^{\infty} B_1 \sin \frac{(m+1)\pi x}{w} \tag{4.20}$$

where B_1 is a constant coefficient.

Similarly, solving Eqn. (4.17) with the no-slip conditions for velocity at the bottom plane and the shear-free stress at the top plane

$$U(x,0) = Y(0) = 0 \tag{4.21}$$

$$U(x,2h) = Y(2h) = 0 \tag{4.22}$$

Note that the shear-free stress at the top plane is justified by Bico *et al.*[3] because the vapor-liquid interface can be considered a free interface with no stress.

Y(y) can be found to be

$$Y(y) = \sum_{n=0}^{\infty} B_2 \sin \frac{(n+1)\pi y}{2h} \tag{4.23}$$

Combining Eqns. (4.20) and (4.22) to obtain

$$U(x,y)=\sum_{m,n=0}^{\infty} B\sin\frac{(m+1)\pi x}{w}\sin\frac{(n+1)\pi y}{2h} \tag{4.24}$$

Substituting Eqn. (4.24) into Eqn. (4.23), we have

$$\frac{\Delta P}{\mu z}=\sum_{m,n=0}^{\infty} B\left[\frac{(m+1)^2\pi^2}{w^2}+\frac{(n+1)^2\pi^2}{4h^2}\right]\sin\frac{(m+1)\pi x}{w}\sin\frac{(n+1)\pi y}{2h} \tag{4.25}$$

To find *B*, we multiply both sides of Eqn. (4.25) with $\sin\frac{(m+1)\pi x}{w}\sin\frac{(n+1)\pi y}{2h}$ and integrate it from $x = 0$ to $x = w$ and $y = 0$ to $y = 2h$ to get

$$B\left[\frac{(m+1)^2\pi^2}{w^2}+\frac{(n+1)^2\pi^2}{4h^2}\right]=\frac{\frac{\Delta P}{\mu z}\int_0^{2h}\int_0^{w}\sin\frac{(m+1)\pi x}{w}\sin\frac{(n+1)\pi y}{2h}dxdy}{\int_0^{w}\sin^2\frac{(m+1)\pi x}{w}dx\int_0^{2h}\sin^2\frac{(n+1)\pi y}{2h}dy} \tag{4.26}$$

Eqn. (4.26) can be reduced to:

$$B=\frac{\Delta P}{\mu z}\frac{16}{\left[\frac{(2m+1)^2}{w^2}+\frac{(2n+1)^2}{4h^2}\right](2m+1)(2n+1)\pi^4} \tag{4.27}$$

Note the change of $(m+1)$ and $(n+1)$ to $(2m+1)$ and $(2n+1)$ respectively as only odd numbers of $(m+1)$ and $(n+1)$ would give a non-zero term. Substituting the expression for *B* above into Eqn. (4.24), we can express the velocity profile as

$$U(x,y)=\sum_{m,n=0}^{\infty}\frac{16\Delta P}{\left[\frac{(2m+1)^2}{w^2}+\frac{(2n+1)^2}{4h^2}\right](2m+1)(2n+1)\pi^4\mu z}\sin\frac{(2m+1)\pi x}{w}\sin\frac{(2n+1)\pi y}{2h} \tag{4.28}$$

Averaging $U(x,y)$ over the area of $(w \times h)$ to find the mean velocity U_{mean}

$$U_{mean} = \frac{\int_0^h \int_0^w U(x,y)dxdy}{wh} = \sum_{m,n=0}^{\infty} \frac{64\Delta P}{\left[\frac{(2m+1)^2}{w^2} + \frac{(2n+1)^2}{4h^2}\right](2m+1)^2(2n+1)^2\pi^6\mu z}$$

$$= \frac{64\Delta P}{\pi^6 \mu z} \sum_{m,n=0}^{\infty} E \qquad (4.29)$$

Note that as the value of each term in the summation series E in Eqn. (4.29) exponentially decreases as m or n increases, we can approximate U_{mean} by considering only the first term ($m=0$, $n=0$) of the summation series which contributes the most to the value of U_{mean}. Then, to take into account the value added to U_{mean} by the rest of the terms, we multiply a constant C to the approximate the value of U_{mean}. Thus, we have

$$U_{mean} \approx C \frac{64\Delta P}{\left[\frac{1}{w^2} + \frac{1}{4h^2}\right]\pi^6 \mu z} \qquad (4.30)$$

To find C, we consider the extreme case where w approaches infinity. In this instance, the flow of fluid is equivalent to the flow on a flat plane and thus Eqn. (4.30) will be reduced to Poiseuille's flow over a flat plane which is given by Bico *et al.*[3] as

$$U_{mean} = \frac{\Delta P h^2}{3\mu z} \qquad (4.31)$$

Equating Eqn. (4.28) when $w \rightarrow \infty$ with Eqn. (4. 31):

$$C\frac{64\Delta P}{\frac{1}{4h^2}\pi^6\mu z}=\frac{\Delta P h^2}{3\mu z}$$

to find $C = \frac{\pi^6}{768}$. Substituting this into Eqn. (4.30) we obtain

$$U_{mean}\approx\frac{\Delta P h^2 w^2}{3\mu z\left[w^2+4h^2\right]} \tag{4.32}$$

Finally, by comparing the mean velocity in Eqn. (4.32) with Eqn. (4.31) we arrive at an expression for β as

$$\beta=\frac{4h^2}{w^2}+1 \tag{4.33}$$

Note that we have carried out a systematic analysis on the effect of the contribution of other terms (where m > 1 and n > 1) in Eqn. (4.29) and justified our assumption to only consider the first term in the summation series. Please refer to Appendix A for this detailed analysis.

4.4 Results and Discussion

4.4.1 Validation of Wicking Criteria

From Chapter 2, we already know that Bico *et al.*[3] had established the condition for wicking $\cos\theta > \cos\theta_c = \frac{1-\phi_s}{r-\phi_s}$ (see Eqn. (2.8)). In this equation, θ is the equilibrium contact angle, Φ_s and r are the pillars fraction and the

surface roughness, respectively. In the case of nanopillars, they can be calculated as

$$r = \frac{\pi dh}{(d+s)^2} + 1, \tag{4.34}$$

$$\phi_s = \frac{\pi d^2}{4(d+s)^2}, \tag{4.35}$$

where structural parameters *d*, *h*, *s* are depicted in Figure 4.2.

A contact angle analysis has been conducted to obtain the equilibrium contact angles of water, θ_{water}, and silicone oil, θ_{oil}, on a flat silicon surface. The images captured from the contact angle goniometer (Figure 4.6) reveal θ_{water} = 56° and θ_{oil} = 18.0°.

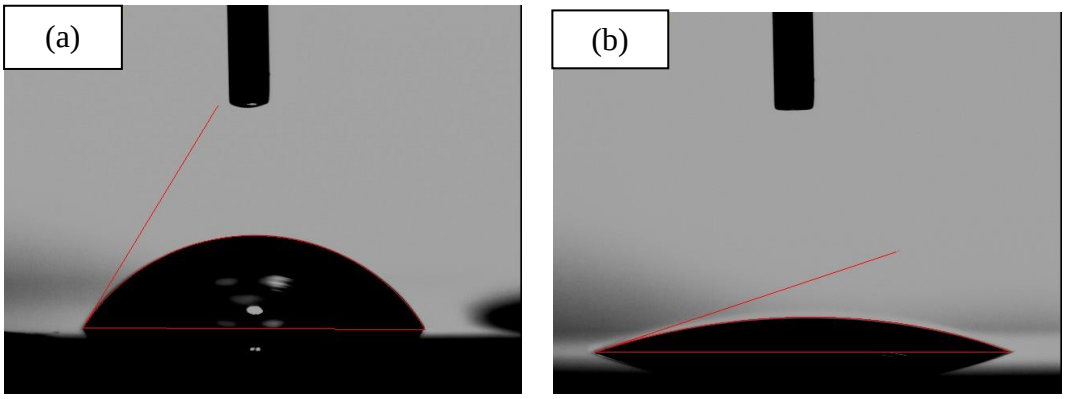

Figure 4.6 Contact angle of (a) water and (b) silicone oil estimated using a contact angle goniometer

Based on Eqns. (2.8), (4.34) and (4.35), we have calculated the critical contact angles for our samples and the values are listed in Table 4.1. From these results, we are able to verify that Bico's condition for wicking ($\theta_c > \theta$)

agrees with our experiments. Water and silicone oil were able to wick in all the samples except for sample A (for water only) which had a critical angle fairly close to the contact angle of water on a flat silicon surface.

Table 4.1 Dimensions of silicon nanopillar samples fabricated by the IL-MACE method. Crucial parameters such as surface roughness *r*, pillars fraction ϕ_s and the critical contact angles θ_c were calculated.

	Etch Time (mins)	**Pillars Diameter (μm)**	**Pillars Height (μm)**	ϕ_s	*r*	θ_c (°)
Pillars A	5	0.28	0.75	0.043	1.90	59.62
Pillars B	10	0.30	2.00	0.064	2.71	69.28
Pillars C	20	0.30	4.20	0.064	4.59	78.07
Pillars D	30	0.30	7.00	0.064	6.98	82.23

4.4.2 Wicking Dynamics

Next, we study the wetting properties of the silicon nanopillar surfaces by examining the wicking dynamics of silicone oil (γ = 3.399 ×10^{-2} N/m, μ = 3.94×10^{-2} Pas).[14] For this measurement, a 1 μl droplet of silicone oil was dispensed onto the bottom of a freshly prepared sample surface at a very slow approaching speed to minimize the impact effect. The snapshots of the whole wicking process are visualized in Figure 4.7. The silicone oil front reaches the top of the sample (which is about 8 mm in height and 7 mm in width) in about 300 sec.

The silicone oil on the sample surface was cleansed by dipping the sample in acetone and IPA for 1 min and rinsed in DI water. The same experiment steps were then carried out to test the wicking of DI water (γ = 7.28 $\times 10^{-2}$ N/m, μ = 8.9$\times 10^{-3}$ Pas). This time the wicking speed was much faster and the water front reached the top of the sample in about 10s. The difference in the wicking speed of silicone oil and de-ionized water could be accounted for by the large difference in the intrinsic properties (such as viscosity and surface tension) of the two liquids (see Eqn. (2.13)).

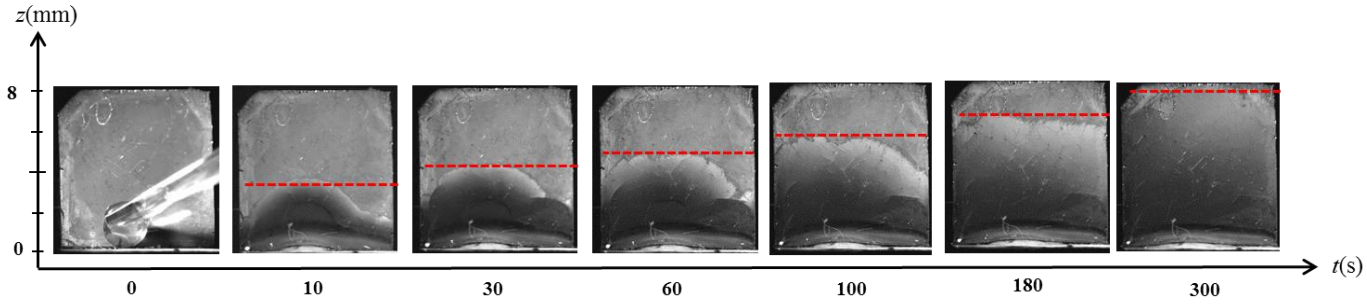

Figure 4.7 Snapshots of the wicking process of silicone oil on silicon nanopillars surface (Sample B). The red dotted line marks the liquid front.

Figure 4.8 shows plots of distance traveled by the wetting front versus the square root of time (i.e. z vs. $t^{1/2}$) for all our samples. Note that the viscous enhancement factor β can be obtained by measuring the gradient of this plot (i.e. the value of D) and substituting the value into Eqn. (2.12).

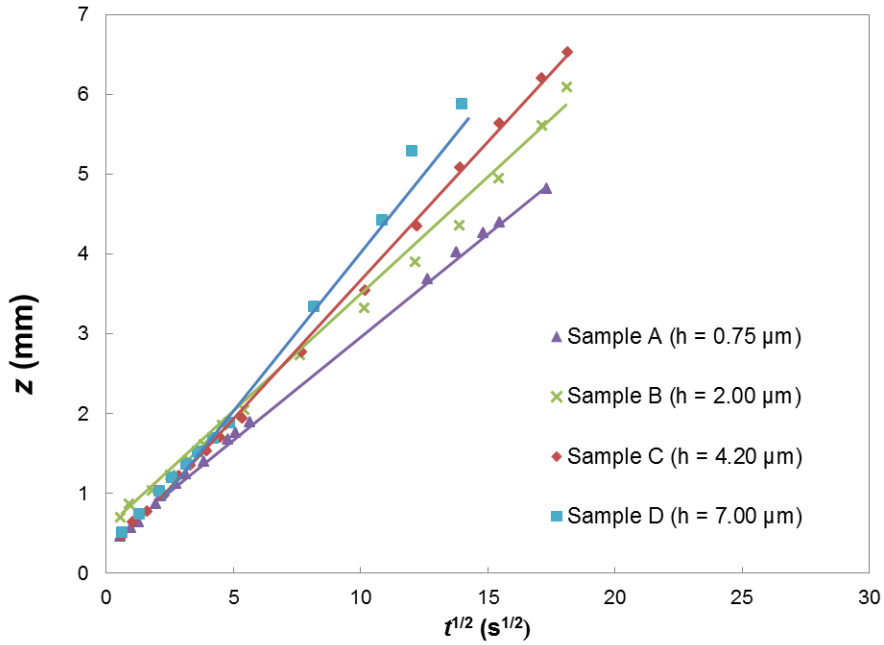

Figure 4.8 Plot of distance travelled by the wetting front against the square root of time for nanopillars with silicone oil (γ = 3.399×10^{-2} N/m, μ = 3.94×10^{-2} Pas, θ_{oil} = 18^{o}).

4.4.3 Validation of Theory

The calculated (from Eqn. (4.33)) and the experimentally determined values of β are plotted in Figure 4.9. As can be seen from this figure, our theoretical values for β fit very well with the experimental data over a wide spectrum of h/w values. Note also, that the empirical values of β obtained with water and silicone oil are very close, thus proving that β is independent of fluid properties, as predicted by Eqn. (4.33). The only exception to this is for the data point at h/w = 7.1, where β (water) deviates from β (silicone oil). This difference is likely due to the deformations of the mechanically weak, high aspect ratio (≈23) nanopillars caused by capillary forces during the wicking process (see Figure 4.1(b) iii).

In Figure 4.9, we also show the values for β calculated for our samples based on the models proposed by Zhang *et al.*[20] and Ishino *et al.*[4]. We have taken the expressions for U_{mean} reported in these papers and compared with Bico's expression ($U_{mean} = \frac{\Delta P h^2}{3\beta\mu z}$) to obtain β. This will give

$$\beta = \frac{1}{1-\phi_s} \qquad \text{for } h < (d+s) \quad (4.36)$$

$$\beta = \frac{4\pi h^2}{3(1-\phi_s)(d+s)^2\left[\ln\left(\frac{2d+2s}{d}\right)-1.31\right]} \qquad \text{for } h > (d+s) \quad (4.37)$$

for Ishino *et al.*[4]'s derivation, and

$$\beta = \frac{4dh^2}{(d+s)^2} \quad (4.38)$$

for Zhang *et al.*[20]'s derivation.

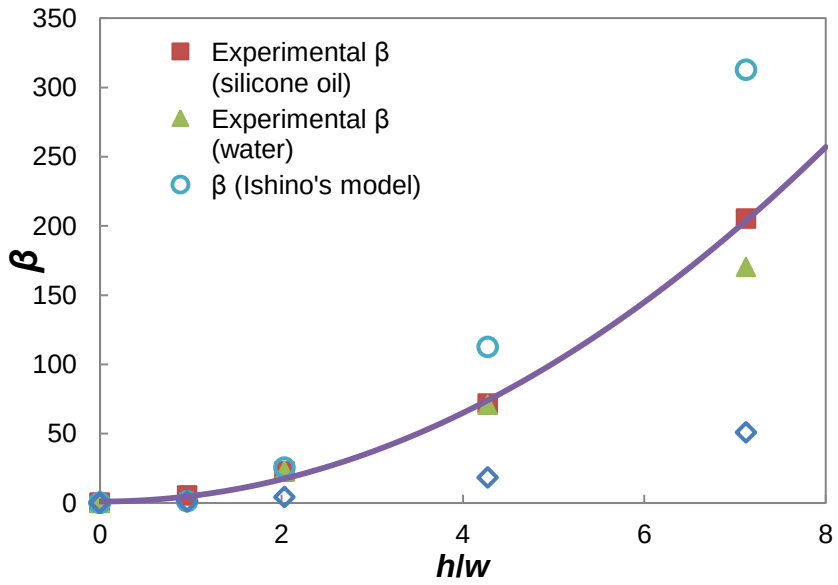

Figure 4.9 Experimental and calculated values of β. Data points for β (silicone oil) and β (water) are obtained with silicone oil and water respectively. Calculation based on our method is represented by a solid line. Also shown in this figure are the calculated β values of our samples based on the models of Zhang *et al.*[20] and Ishino *et al.*[4]

It can be observed that Zhang *et al.*[20]'s approximation for β underestimates the true value for all h/w, while Ishino *et al.*[4]'s expressions overestimate the experimental β at high h/w (≥ 4) but underestimate it at low h/w (< 2). The reason for the deviations can be attributed to the models that were considered. For instance, Zhang *et al.* estimated the flow between the pillars to be Poiseuille's flow between two flat plates (the pillars being the plates) and ignored the contribution to the viscous loss by the floor at $y = 0$. In addition, viscous loss was only considered to occur when the flow occurs between two pillars. However, the velocity profile when the flow proceeds past the channels between adjacent pillars is not expected to be spatially constant and thus there should also be shear losses involved in those regions. For these reasons, the β values determined from Zhang *et al.'s* model are lower than the experimental values. As for Ishino *et al.'s* method, when $h < (d+s)$ the flow between micropillars is assumed to be similar to the flow over a flat plane. In this case, it is expected that the calculated β values should be smaller than the experimental values because the effect of micropillars on viscous loss was not considered. For $h > (d+s)$, *Ishino et al.*[4] suggested that the micropillars could be considered to be infinite and thus the calculated β values were anticipated to be larger than the actual values.

To further validate our theory, we calculate the β values for the micropillars reported by Ishino *et al.*[14] The theoretical predictions by Ishino *et al.* and Zhang *et al.* are presented alongside our calculated β values and the experimentally determined data for comparison purposes. The results are plotted in Figure 4.10. It can be seen that our model fits Ishino *et al.*'s

experimental data very well, and shows a significant improvement over Ishino *et al.*'s theoretical estimation of β values when h is small. Interestingly, our theory (Eqn. (4.33)) and Ishino *et al.*'s model (Eqn. (4.37)) converge when h increases. However, this is only coincidental as it can be proven mathematically that this is not true for all d and s values. In addition, Ishino *et al.*'s results agree with our conclusion that β is independent of the properties of the test fluid.

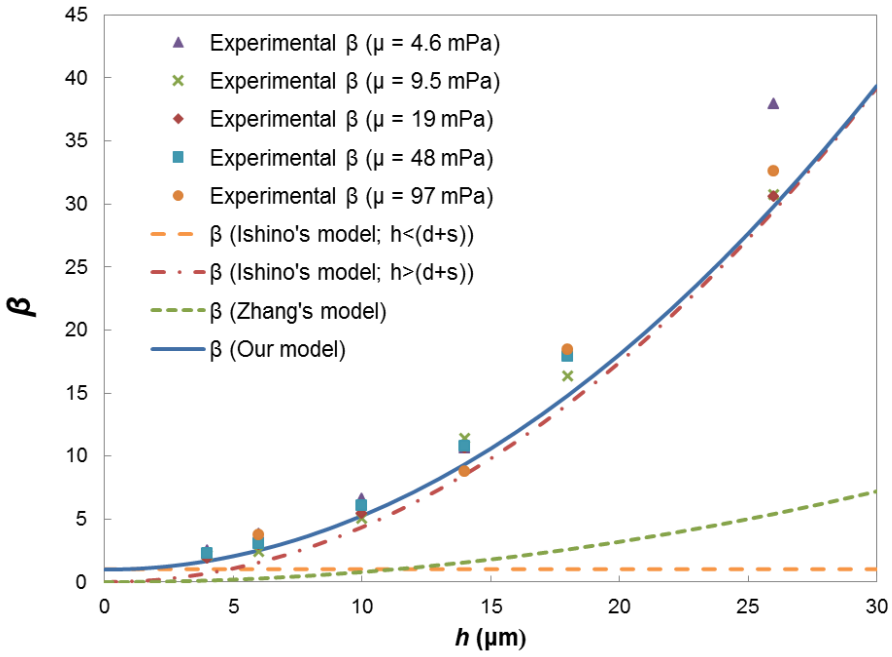

Figure 4.10 Comparison of β values obtained by our methods and others for the micropillars experiment presented in Ishino *et al.*'s paper. Experimental and theoretical values are plotted as points and lines respectively. Our model is represented by a solid blue line. Five different test liquids ($\gamma = 2\times10^{-2}$ N/m) were used and their respective viscosities are given in the legend. $d = 2$ μm and $s = 8$ μm remained constant for all experiments.

Our model described in Eqn. (4.33) can also be employed to solve an observation previously made by Ishino *et al*. in which the wicking coefficient D becomes increasingly independent of nanopillar height h as h becomes very

large. By considering $h >> d, s, w$ in Eqns. (4.1) and (4.33) to (4.35), it can be shown that $\frac{\cos\theta - \cos\theta_c}{\cos\theta_c} \sim h$ and $\beta \sim h^2$. Therefore, from Eqn. (2.13), D will approach a constant value.

This means that in the regime of short pillars, when the pillar height is increased, the capillary driving force for wicking is increased more than the viscous loss (represented by β) and this will result in a faster wicking velocity. This finding also agrees well with McHale *et al.*[7]'s experiment results whereby faster spreading dynamics were observed when increasing the pattern height. However, as the pillars grow taller, the viscous force is increasing as fast as the capillary driving force with increasing height and therefore a maximum speed will be reached. In the nanopillars discussed in this chapter, if the diameter d = 0.3 μm and spacing s = 0.7 μm remain, D saturates at 0.117 mm^2/s for silicone oil when the pillar height h reaches about 5 μm. The understanding that wicking velocity cannot be endlessly improved by increasing h has important implications for the designing of engineering applications based on wicking and is one of the many insights that can be derived from this model.

Furthermore, it can be seen from Eqns. (2.13), (4.33-35) that beside h, the speed of wicking can be controlled by adjusting other dimensional parameters such as the diameter d and spacing s. For instance, all else being equal, higher speed of wicking can be achieved by increasing d. Similar to the case of height, the wicking speed cannot be enhanced without end. When d

increases, $\cos\theta_c$ also increases and at certain value of d, the condition for wicking (Eqn. (2.8)) is not met and the wicking will not occur. Finding an optimized set of value of d, s and h for the maximum wicking speed is not a straightforward task because the nonlinearity of the function gives expectation of many local maxima. Despite this, a rough estimation, with realistic constraints such as $s > 0.1$ μm, $h < 20$ μm, $d \leq h$, and $\cos\theta_c < 0.45$, reveals that the highest wicking speed can be achieved at $d = h = 20$ μm and $s = 11.34$ μm. This will yield $D \approx 4.41$ mm^2/s.

It is also noteworthy to consider the extreme case where the structural dimensions are extremely small. Remember that the capillary pressure can be roughly estimated by $P=\gamma/h/(\cos\theta-\cos\theta_c)/\cos\theta_c$. When the pillars height reduces to Angstrom range, P is in the range of 10^8 N/m. While the compressibility for water decreases (thus it remains an incompressible fluid), the compressibility of silicone oil increases to 13%. As such, the assumption of constant density is no longer valid, the continuity equation (Eqn. (4.6)) cannot be simplified, and the solving of the Navier-Stokes equation will be more challenging. In this regime, besides capillary and viscous forces, we need to consider the dispersion force component (i.e. the *van de Waals* force), which will further complicate the calculation. Despite this limitation, our theory proved to be valid for a wide range of practical dimensions.

4.5 Summary

We presented in this chapter a theoretical study and an experimental validation of the wicking dynamics on a regular silicon nanopillars surface. The enhancement factor of viscous loss, β, due to the presence of nanopillars was investigated and found to depend on the ratio of h/w where w is the width of the channel that is used to approximate the wicking. Our expression for β was also found to be applicable to published results obtained by other groups.

The success in describing the dynamic of wicking explicitly without any empirical parameters means that the wicking property (i.e. speed) of a particular material can be adjusted by simply controlling the geometry (i.e. height) of the textured surface. All things being equal, the wicking speed increases with increasing nanopillars' height. However this speed will eventually reach a maximum value at a certain nanostructures' height. These insights are valuable for design and realization of potential wicking applications.

4.6 References

1. E. Martines, K. Seunarine, H. Morgan, N. Gadegaard, C. D. W. Wilkinson, and M. O. Riehle. Superhydrophobicity and Superhydrophilicity of Regular Nanopatterns. *Nano Letters* **2005**, 5[10] 2097-2103.

2. R. N. Wenzel. Resistance of Solid Surfaces to Wetting by Water. *Industrial & Engineering Chemistry* **1936**, 28[8] 988-994.

3. J. Bico, C. Tordeux, and D. Quéré. Rough wetting. *Europhysics Letters* **2001**, 55[2] 214.

4. C. Ishino, M. Reyssat, E. Reyssat, K. Okumura, and D. Quéré. Wicking within forests of micropillars. *Europhysics Letters* **2007**, 79 56005.

5. C. W. Extrand, S. I. Moon, P. Hall, and D. Schmidt. Superwetting of Structured Surfaces. *Langmuir* **2007**, 23[17] 8882-8890.

6. Y. Chen, L. S. Melvin Iii, M. M. Weislogel, R. M. Jenson, S. Dhuey, and P. F. Nealey. Design, fabrication, and testing of microporous wicking structure. *Microelectronic Engineering* **2008**, 85[5–6] 1027-1030.

7. G. McHale, N. J. Shirtcliffe, S. Aqil, C. C. Perry, and M. I. Newton. Topography Driven Spreading. *Physical Review Letters* **2004**, 93[3] 036102.

8. H. S. Ahn, G. Park, J. Kim, and M. H. Kim. Wicking and Spreading of Water Droplets on Nanotubes. *Langmuir* **2012**, 28[5] 2614-2619.

9. A. Y. Vorobyev and C. Guo. Laser turns silicon superwicking. *Opt. Express* **2010**, 18[7] 6455-6460.

10. A. Y. Vorobyev and C. Guo. Water sprints uphill on glass. *Journal of Applied Physics* **2010**, 108[12] 123512-123514.

11. T. A. Savas, M. L. Schattenburg, J. M. Carter, and H. I. Smith, "Large-area achromatic interferometric lithography for 100 nm period gratings and grids," pp. 4167-4170. **Vol. 14**.

12. M. K. Dawood, H. Zheng, N. A. Kurniawan, K. C. Leong, Y. L. Foo, R. Rajagopalan, S. A. Khan, and W. K. Choi. Modulation of surface wettability of superhydrophobic substrates using Si nanowire arrays and capillary-force-induced nanocohesion. *Soft Matter* **2012**, 8[13] 3549-3557.

13. R. E. Bolz, "CRC Handbook of Tables for Applied Engineering Science." Taylor & Francis, (1973).

14. Shin-Etsu Silicone fluids datasheet. http://www.silicone.jp/e/products/type/oil/index.shtml

15. J. G. Fan and Y. P. Zhao. Freezing a water droplet on an aligned Si nanorod array substrate. *Nanotechnology* **2008**, 19[15] 155707-155707.

16. A. M. Cazabat and M. A. C. Stuart. Dynamics of wetting: effects of surface roughness. *The Journal of Physical Chemistry* **1986**, 90[22] 5845-5849.

17. G. K. Batchelor, "An Introduction to Fluid Dynamics." Cambridge University Press, (2000).

18. K. E. Kennedy and M. U. o. N. . "Fingering Instabilities in Newtonian and Non-Newtonian Fluids." Memorial University of Newfoundland (Canada), (2007).

19. E. Guyon, "Physical Hydrodynamics." OUP Oxford, (2001).

20. C. Zhang and C. H. Hidrovo, "Investigation of Nanopillar Wicking Capabilities for Heat Pipes Applications," pp. 423-437 in ASME 2009 Second Inter. Conf. on Micro/Nanoscale Heat and Mass Transfer

Chapter 5

Results and Discussion II: Influence of geometry on wicking in silicon anisotropic nanostructures

5.1 Introduction

From the previous chapter, we have gained some understanding about the mechanisms of wicking in silicon hydrophilic surface, and the effects of micro-/nano-structures in acting as the driving force of wicking and also enhancing the frictional viscous force. Previous efforts to shed light on the impedance to wicking flow caused by surface asperities have proven to be difficult without the introduction of fitting parameters or separation of the flow into discontinuous regimes. We were able to circumvent such difficulties in Chapter 4 and provided a more comprehensive analysis of β. However, like most other studies,[1-4] the results were obtained from square arrays of circular pillars. Although the nanopillar structure is a good starting point to study wicking since the pillars' symmetrical geometry simplified the analysis, it also restricted the amount of further insights that could be gained. For example, one of the biggest drawbacks of the β estimation is that the approach does not

take into account the role of the structural orientations. For the case of micro-/nano-pillars, this property can be reasonably ignored since the structures have a high degree of isotropicity and one should expect the rate of wicking to remain unchanged even if the sample is rotated. The problem arises when the structures under test are anisotropic. For example, nanofin (Figure 5.1(b)) is an asymmetrical structure where one side is significantly longer than the other. Should we expect the rate of wicking to be the same in the directions along these two sides of the nanofins?

It is therefore necessary to further study the role of geometrical properties. A good approach would be to investigate the dynamics of wicking in different directions on a surface decorated with anisotropic micro-/nano-structures. In literature, there are few publications that study wicking in such surfaces. Zhou *et al.*[5] for instance, studied the wetting of distilled water on a silicon microgrooves surface and found that the liquid mostly spread laterally along the direction of the grooves, with very little spreading to the side. This was expected because the grooves acted like a canal which constrained fluid movement along the direction of the grooves. In another work, Chen *et al.*[6] fabricated some un-conventional structures such as waffles and half-ladder structures with different dimensions. However, the study was more like a demonstration of design and fabrication method. No further analysis was conducted to examine the relationship between surface geometry and wicking performance. In a more comprehensive study, Reyssat *et al.*[7] conducted a thorough analysis on the imbibition of fluid inside a channel with axial variations and concluded that there is a deviation from the diffusive law.

In short, there has not been a systematic study of the geometrical effect of asymmetrical micro-/nano-structures on wicking in the literature. To fill in this gap, we make use of IL-MACE techniques to produce hexagonal arrays of nanofins on a flat P-type (100) silicon substrate.[8,9] Nanofin structure is a perfect candidate for this study because of its asymmetrical geometry. Meanwhile, its structural simplicity allows us to effectively examine the effect of structural orientation on wicking characteristics.

5.2 Experimental Details

The fabrication process for nanofin structures using IL-MACE techniques is similar to that of nanopillar structures (see Figure 4.1). The only difference in the fabrication step is during the lithography process. Recall from Chapter 3 that the Lloyd's mirror setup allows light from the original beam to interfere with the light reflected off the mirror to form a standing wave pattern which is then recorded in the photoresist (see Chapter 3.3). For a single exposure, this generates a pattern of periodic lines (Figure 5.2(a)) in the photoresist layer with the period equal to $\frac{\lambda}{2}\sin\alpha$.

Different patterns can be achieved by utilizing the multiple exposure method. For instance, a second exposure of 90^o (tilt the sample by 90^o with respect to the first exposure) generates a rectangle array of circular photoresist

dots on the silicon surface. After developing and etching, the circular nanopillar structures were obtained (Figure 5.1(a)), similar to those shown in Chapter 4.

Similarly, to produce nanofin structures, a second exposure is required with the sample tilted by an acute angle (< 90^o) with respect to the initial exposure (Figure 5.1(b)). This effectively generates an array of parallelogram photoresist dots as shown in Figure 5.2(c). Because of the edge effect, after developing and etching, the resulting structure takes the shape of a ellipse. Note that in this case, the array layout of the nanofins is hexagonal.

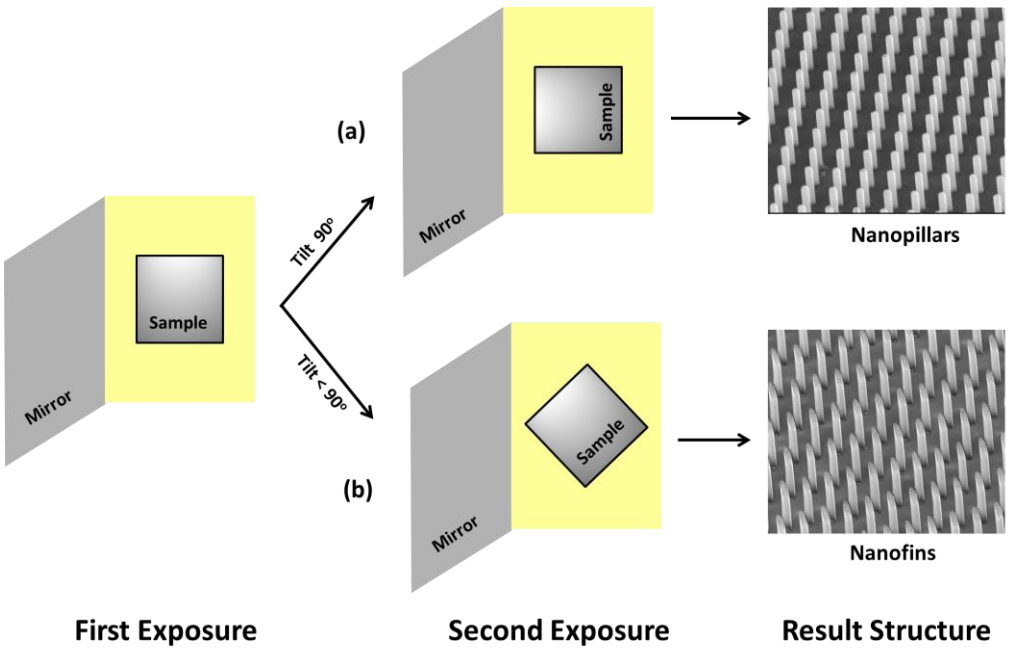

Figure 5.1 Different patterns can be achieved by utilizing multiple exposure method. For instance, a double exposure of 90^o (a) will create nanopillar structures after further processing (developing and etching). A double exposure of less than 90^o (b) will create nanofin structures.

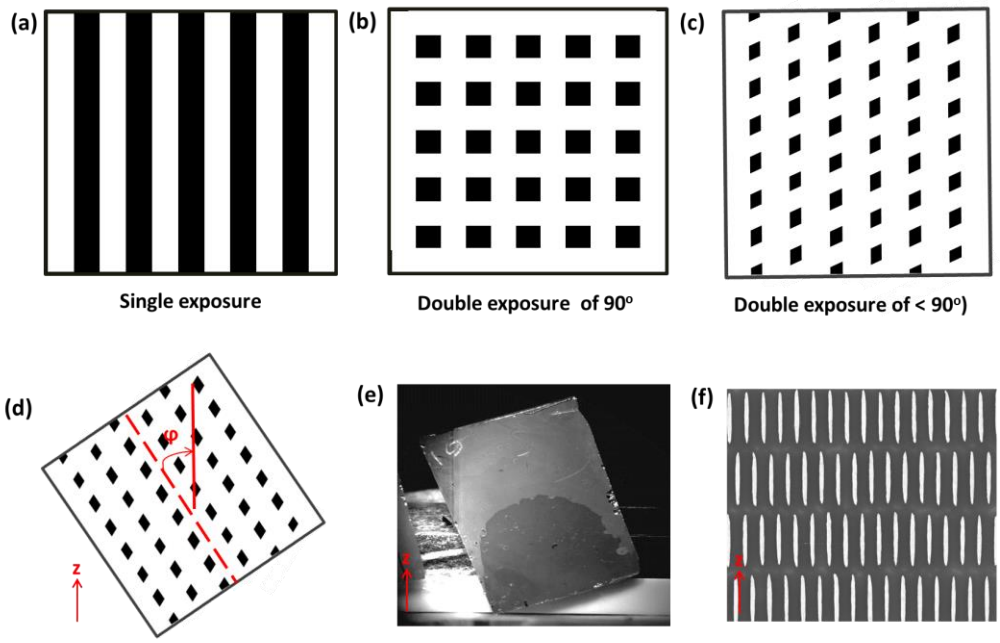

Figure 5.2 Photoresist (denoted by the black color dots) remaining after (a) a single exposure, (b) a double exposure of 90° and (c) a double exposure of less than 90°. The white areas represent the silicon surface. To study wicking in nanofin structures, the sample is tilted so that the nanofins' major axis stands either vertically along the *z*-axis direction (*z* (*normal*)) like illustrated in (d), or horizontally (*z* (*parallel*)). Photo in (e) shows a representative sample tilted for *z* (*normal*) setup. SEM image in (f) shows that the fins' major axis is indeed along the *z*-axis direction.

It can be seen that if the sample is put upright, the fins are slanted (Figure 5.2(c)), which is not ideal for this study. We are more interested in investigating the extreme cases, where the fins' major axis either stands upright vertically (*z* (*normal*)) or horizontally (*z* (*parallel*)). This can be achieved by tilting the samples accordingly when carrying out the wicking experiments. For instance, the alignment of *z* (*normal*) is illustrated in Figure 5.2(d-e). The SEM image for the corresponding orientation is shown in Figure 5.2(f). Similarly, to align for *z* (*parallel*), the sample is tilted 90° with respect to *z* (*normal*).

A total of eleven samples with varying dimensions were fabricated for this study. Figure 5.3 shows the SEM pictures of these nanofin structures. The detailed parameters and dimensions of the samples can be found in Table 5.1.

To measure the displacement of the wicking front with time, about 1μl of silicone oil was deposited at one end of the sample surface and the entire wicking process was recorded at 1000 fps. For every sample, two sets of experiment were carried out for wicking in *z* (*normal*) and *z* (*parallel*) direction. After the first set of experiment, the sample was cleaned with acetone and DI water. The sample was then blown dry with a heat gun, which emitted a stream of hot air at 65^{o}C, to ensure that no trace of silicone oil was left on the sample surface.

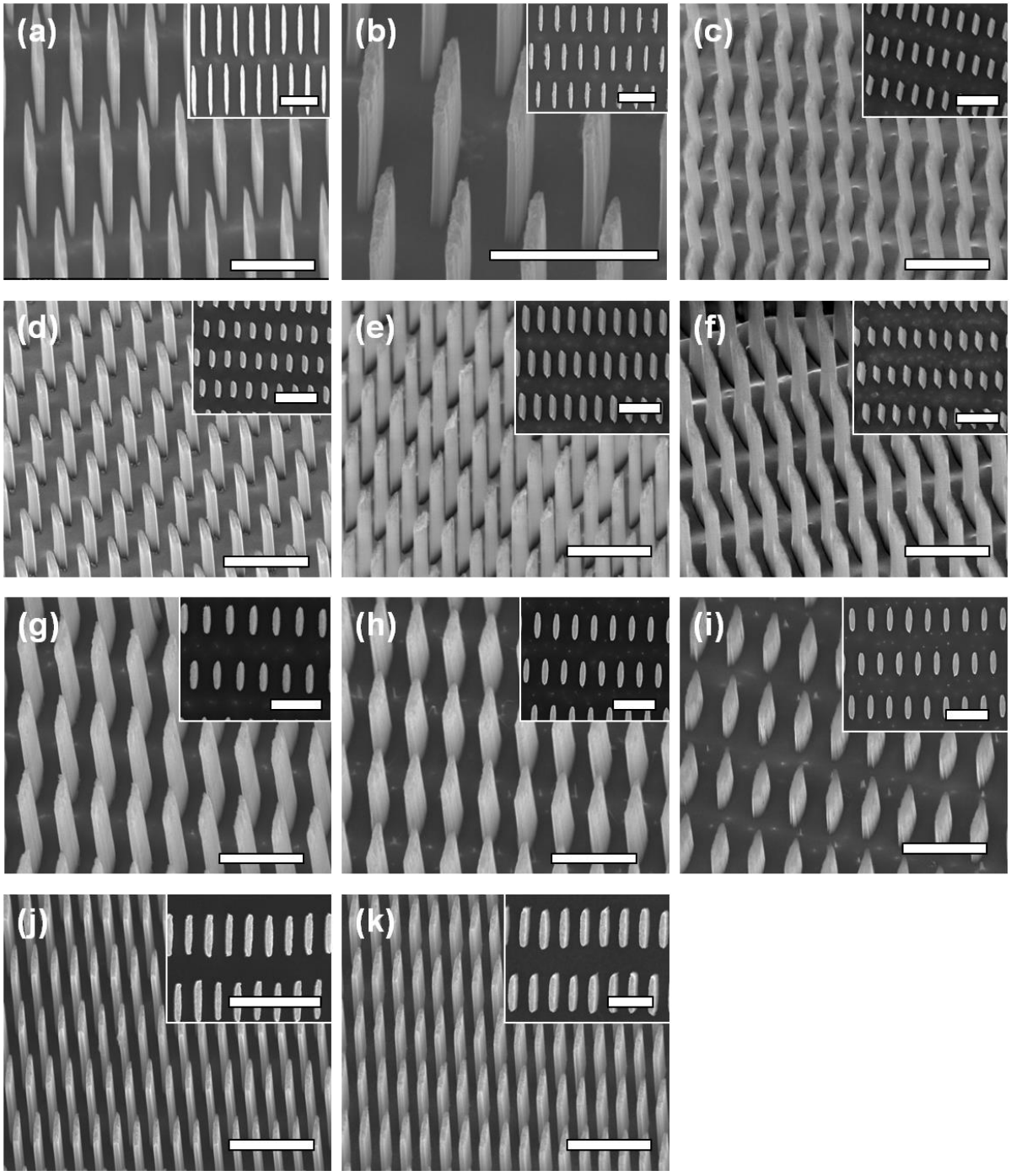

Figure 5.3 SEM pictures of nanofin samples A - K used for this study tilted at 35^{o} angle. Insets show top view of nanofins. Each scale bar represents 2μm.

5.3 Experimental Results

A schematic diagram (top-view) and details of the important dimensions for eleven nanofin structures are given in Figure 5.4 and Table 5.1, respectively. The wicking direction depends on how the nanofin structures are aligned and denoted as *z (normal)* and *z (parallel)* in Figure 5.4. The light blue region represents the flat silicon surface, while the yellow region shows the top of the nanofins. Note that this figure also depicts a dark blue area *A* between the two consecutive nanofins in the same column where the mean flow velocity is zero. This area represents the loss of driving pressure due to the form drag for the case of wicking in *z (normal)* direction only. This assumption will be explained in detail later.

Table 5.1 Geometrical parameters of nanofins used in this study where *h* refers to the height of the nanofins, and definitions of *p, q, m* and *n* can be found in Figure 5.4. Important parameters such as the pillar fraction (ϕ_s) and the surface roughness (r) were shown.

	Sample (all dimensions are in μm)										
	A	**B**	**C**	**D**	**E**	**F**	**G**	**H**	**I**	**J**	**K**
p	3.00	1.47	0.95	0.74	1.17	0.74	1.12	1.21	1.13	1.00	0.85
q	0.60	0.69	1.00	0.72	0.92	1.15	1.06	1.08	1.05	0.63	0.63
m	0.26	0.19	0.19	0.21	0.25	0.16	0.25	0.28	0.27	0.18	0.15
n	0.67	0.81	0.64	0.55	0.57	0.58	0.71	0.69	0.64	0.31	0.32
h	2.33	1.91	2.20	1.77	3.29	3.35	3.10	2.10	1.15	2.34	1.85
r	5.55	3.94	4.12	4.05	6.46	5.34	5.05	3.83	2.63	7.94	6.30
ϕ_s	0.24	0.13	0.11	0.14	0.17	0.09	0.13	0.15	0.15	0.22	0.18

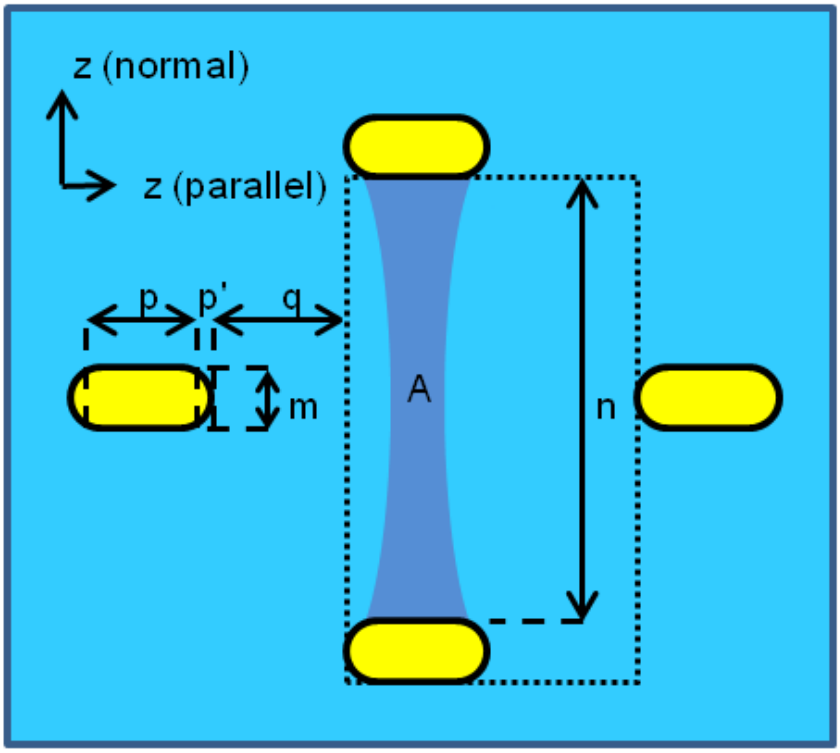

Figure 5.4 Schematic diagram (top-view) of the nanofin structures. The area of the dark blue region is given by *A* and the mean velocity of the fluid in this area is assumed to be zero when wicking occurs in *z (normal)* direction. Note also that *p*' << *p* for all our samples. The dotted line demarcates a unit cell of the nanofins.

About 1µl of silicone oil was deposited at one end of the sample surface and the entire wicking process was recorded in both *z (parallel)* and *z (normal)* directions for each sample. The snapshots fof the whole wicking process for a representative sample are visualized in Figure 5.5.

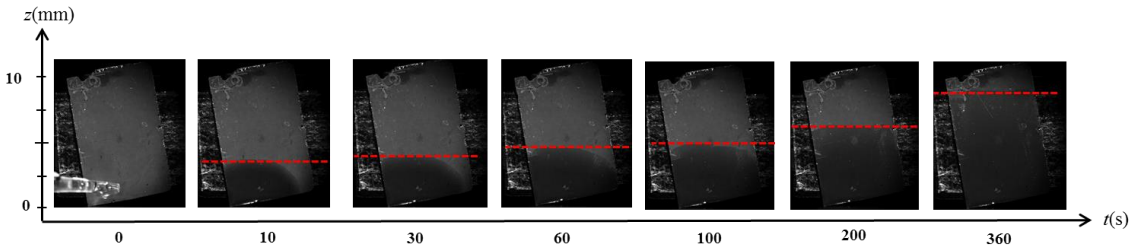

Figure 5.5 Snapshots of the wicking process of silicone oil on representative silicon nanofins surface. The sample is slightly tilted to examine wicking in *z (normal)* direction. The red dotted line marks the liquid front.

Figure 5.6 shows typical z vs. $t^{1/2}$ plots for wicking in the *z (parallel)* and *z (normal)* directions for the same sample. As expected from Bico *et al.*[1]'s analysis and previous studies, the plots follow a diffusive response, or in other words, exhibit a linear relationship between z and $t^{1/2}$. The linear trend does not extend to the origin, however, which is consistent with the results presented in previous studies.[1,2] One of the reasons may be due to the influence of droplet spreading during the early stages of wicking. More specifically, when the liquid droplet comes in contact with the nanostructured surface, the wetting process can be observed to take place in two stages: firstly a spreading of the liquid droplet, followed by the wicking process. The purpose of this spreading of liquid might establish an effective contact angle on the silicon surface as proposed by Bico *et al.*[1] The spherical cap shaped droplet becomes flatter and widens its radius over a surface in a very short period of time (< 1 sec) before a thin film of liquid appears and seeps ahead of the bulk liquid droplet. As a result, the dynamics of the initial stages of the wicking process is affected by the inertia of this droplet spreading. The details of this initial stage will be investigated in Chapter 6.

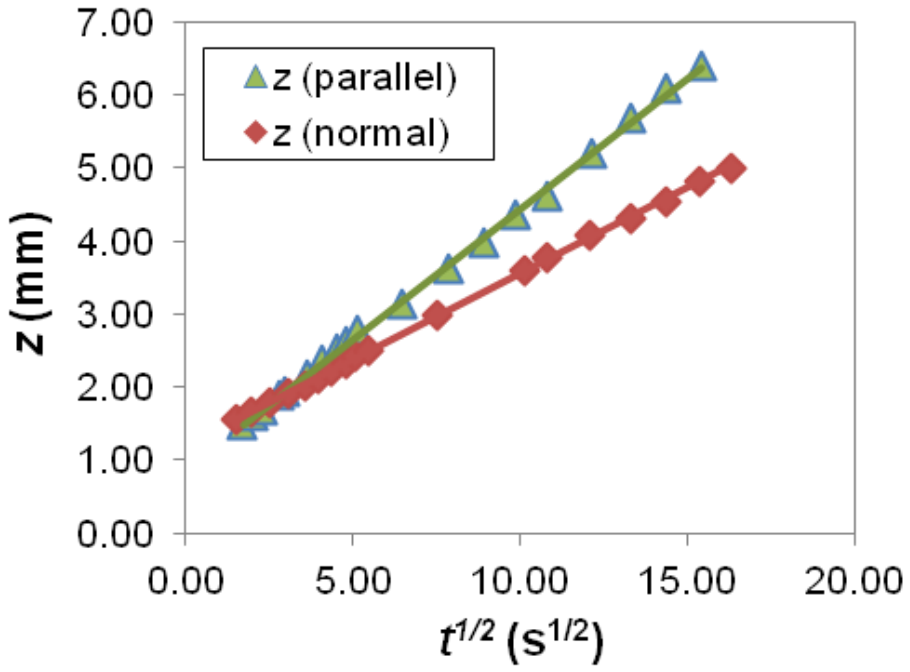

Figure 5.6 Representative *z* vs. $t^{1/2}$ plots obtained experimentally for wicking of silicone oil on a single sample surface. Best fit lines were drawn through the data points.

5.4 Theoretical Model

From Figure 5.6, it is clear that the viscous enhancement factor β, which is inversely proportional to the square of the gradient of the *z* vs. $t^{1/2}$ graphs, is distinctly different for *z (parallel)* and *z (normal)*, even when the experiments were conducted on the same sample surface. This implies that nanoscale geometry and the forces retarding the wicking flow, as caused by the nanostructures, are strongly correlated.

These retardation forces essentially consist of firstly, viscous drag, which arises due to shear stresses between fluid layers as a result of the "no-

slip" condition at the fluid-solid interface, and secondly, form drag, which is related to the pressure distribution around the solid body. The magnitude of form drag experienced by a flow is influenced by how streamlined the solid body is.

To establish this correlation theoretically, similar to the case of nanopillar structures, we firstly approximate the viscous dissipation associated with a unit cell of the nanofin to be roughly the same being caused by an open channel of the same height and length (in the direction of the flow) holding the same volume of actively flowing fluid. This approximation has been proven to work well for micro-/nano-pillars in the previous chapter, giving the expression (Eqn. (4.33))

$$\beta = \frac{4h^2}{w^2} + 1,$$

where w is the width of the channel which can be easily computed by dividing the volume of actively flowing fluid in a unit cell of nanofin by the height and length of the unit cell. For the case of nanopillars in Chapter 4, β was estimated under the assumption that the pillar structures were streamlined and thus the form drag due to the solid body was negligible.

In the case of nanofin structures, to account for the energy lost to form drag, we designate a certain volume of fluid in a unit cell of nanofin to be stagnant. In other words, this particular volume of fluid, V_{form}, is assumed to have lost all its capillary driving pressure, ΔP, due to form drag and therefore, its mean velocity has fallen from U_{mean} to zero while the remaining fluid in the

unit cell retains ΔP and continues to flow at U_{mean}. The energy loss per unit cell due to form drag caused by a single nanofin, ΔE_{form}, can therefore be written as

$$\Delta E_{form} = V_{form} \Delta P \tag{5.1}$$

Furthermore, we will assume that ΔE_{form} is only significant if the nanostructure possesses flat planes that are normal to the capillary flow direction, as such geometry tends to cause the overall structure to be considerably non-streamlined. In other words, there is substantial form drag for wicking in *z (normal)* due to the presence of the plane of area *ph* but there is no significant form drag for wicking in *z (parallel)* because the rounded ends of the nanofins of length, *p'*, and width, *m*, offer no flat normal planes to impede capillary flow. This assumption is supported by previous studies which indicated that form drag for viscous flows is significantly less pronounced in circular pillars[10] than square pillars.[11] This also implies that V_{form} can only occupy a space within the area *pn* when wicking takes place in *z (normal)*. Therefore, with reference to Figure 5.4, we have

$$V_{form} = Ah = kpnh\ , \tag{5.2}$$

where $0 \leq k \leq 1$.

Starting with the schematic diagram of the nanofins shown in Figure 5.4, we first note that the length of the rounded ends of the nanofins, *p'*, (due to the edge effect described above) which is not necessarily equivalent to *m*/2, is much smaller than *p* for our samples such that the length of the nanofin can be taken as $p + p' \approx p$. As a result, we can calculate the solid fraction Φ_s and surface roughness *r* as

$$\phi_s = \frac{pm}{(p+q)(m+n)} \tag{5.3}$$

and

$$r = \frac{2h(p+m)}{(p+q)(m+n)} + 1 \tag{5.4}$$

Next, consider wicking in the *z (normal)* direction. Since the energy lost to form drag in a unit cell of nanofin, ΔE_{form}, is equal to $knph\Delta P$ (Eqns. (5.1) and (5.2)), we can obtain the energy loss due to form drag per unit width of the sample, dE_{form}, as

$$dE_{form} = \Delta E_{form}\left(\frac{dz}{(p+q)(m+n)}\right) = (1-\phi_s) f \Delta P h dz\,, \tag{5.5}$$

where

$$f = \frac{kpn}{(1-\phi_s)(p+q)(m+n)}\,, \tag{5.6}$$

f represents the fraction of fluid that is stagnant, which is also equivalent to the fraction of energy lost to form drag. The remaining energy, when averaged over the entire fluid volume, *dV*, then gives the reduced pressure driving the capillary flow, $\Delta P'$, as

$$\Delta P' = \frac{dE - dE_{form}}{dV} = \Delta P(1-f) \tag{5.7}$$

Eqn. (5.7) describes a situation in which all of the fluid volume in a unit width of the sample, *dV*, is flowing with reduced pressure of $\Delta P'$ due to the form drag. This is different from the previously described situation where a reduced volume of fluid, $dV - dV_{form}$ is flowing with the original driving pressure, ΔP, which is not reduced by form drag.

In Chapter 4, we have shown that for steady-state, incompressible fluid in the capillary-dominated regime, flow in a unit cell of nanopillar can be approximated by a similar flow in an open channel of the same height and length (in the direction of the flow), which holds the same volume of liquid. Extending the usage of this approximation to the nanofin structure, the velocity of the wicking front in the *z (normal)* direction can therefore be found by considering U_{mean} for a flow in an open channel of height, h, and length, $m + n$, which contains $V_{normal} = (1 - \phi_s)(p + q)(m + n)h - kph$ amount of actively flowing fluid. Note that the volume of fluid, $kpnh$, is stagnant due to the form drag. The width of the channel, w_n, is therefore

$$w_n = (1-f)(1-\phi_s)(p+q) \tag{5.8}$$

For the case of wicking in the *z (parallel)* direction, because there are no form drag and no stagnant area, a unit cell of nanofin is modeled as an open channel of height, h, and length, $p + q$, which contains $V_{parallel} = (1 - \phi_s)(p + q)(m + n)h$ amount of actively flowing fluid. As a result, the width of the channel, w_p, is

$$w_p = (1 - \phi_s)(m + n) \tag{5.9}$$

Following the approach in Chapter 4, the mean velocity of flow, taking into account form drag, can be given by

$$U_{mean} = \frac{\Delta P'}{\mu z}\frac{h^2 w_n^{\,2}}{3\left(4h^2 + w_n^{\,2}\right)} = (1-f)\frac{\Delta P}{\mu z}\frac{h^2 w_n^{\,2}}{3\left(4h^2 + w_n^{\,2}\right)} \tag{5.10}$$

Finally, by comparing Eqn. (5.10) with the equation for U_{mean} given by Bico *et al.*[1] ($U_{mean} = \frac{\Delta P h^2}{3\beta\mu z}$), we obtain

$$\beta\,(normal) = \left(\frac{1}{1-f}\right)\left(\frac{4h^2}{w_n^{\,2}} + 1\right) \tag{5.11}$$

For wicking in *z (parallel)* direction, there is no form drag as discussed above, and thus, $f = 0$. Consequently, β *(parallel)* can be expressed as

$$\beta\left(parallel\right) = \frac{4h^2}{w_p^{\,2}} + 1 \tag{5.12}$$

As a preliminary check on the validity of Eqns. (5.11) and (5.12), let us consider the effect of varying the nanofin dimensions on β. At one extreme case, in the absence of nanostructures ($p \rightarrow 0$, $p' \rightarrow 0$, $m \rightarrow 0$, $q \rightarrow \infty$, $n \rightarrow \infty$, $h \rightarrow 0$), β *(normal)* = β *(parallel)* = 1 and the only obstruction to the capillary flow is the viscous dissipation provided by the basal plane which is similar to the Poiseuille's flow as discussed in Chapter 4. At another extreme case, if the nanostructures are much larger than the gaps between them ($q \rightarrow 0$, $n \rightarrow 0$, $p \rightarrow \infty$, $m \rightarrow \infty$), β *(normal)* = β *(parallel)* $\rightarrow \infty$ as there is essentially no room for wicking to take place. Thus, it can be seen that eqns. (5.11) and (5.12) give reasonable predictions even in the limiting cases.

The general expression for β after taking into account both viscous and form drags can then be derived as

$$\beta = \left(\frac{1}{1-f}\right)\left(\frac{4h^2}{w^2} + 1\right), \tag{5.13}$$

where h is the height of nanostructures, f represents the fraction of fluid that is stagnant and w_n, w_p represent the channel widths calculated for wicking in *z (parallel)* and *z (normal)* directions, respectively. All three parameters can be calculated in Eqns. (5.6), (5.8) and (5.9).

5.5 Discussion

Eqn. (5.13) proves that for wicking in *z (parallel)* direction, $f = 0$ because of the assumption that ΔE_{form}, and therefore, V_{form} (from Eqn. (5.2)), is insignificant. This is due to the rounded ends of the nanofins offering no flat normal planes to impede the capillary flow. This applies for circular micro-/nano-pillars too, with the consequence that Eqn. (5.13) is returned to Eqn. (4.33). Thus, it can be seen that the theoretical treatment of β presented here is a generalized version that is consistent with the theory presented in our previous study of wicking in circular micro-/nano-pillars.[12]

From Eqns. (5.5) and (5.13), it can be seen that other than k (embedded in A), all variables can be determined directly by measuring the dimensions of the nanofins using SEM pictures. To obtain an empirical value for k and investigate how it varies for different samples, we used these two equations and experimental values of β *(normal)*, i.e. β for wicking in the *z (normal)* direction, to determine A. Then we plot A against pn to fit k (Figure 5.7).

From Figure 5.7, it can be seen that *A* and *pn* follow a linear relationship. Therefore, *k*, which corresponds to the gradient of the plot, is constant for all samples with an approximate value of **0.912**. The physical interpretation of this is that 91.2% of the fluid in the area of *pn* between the two consecutive fins has completely lost its driving capillary energy to form drag. This is rather unexpected as *k* is independent of the velocity of flow which is known to affect drag.

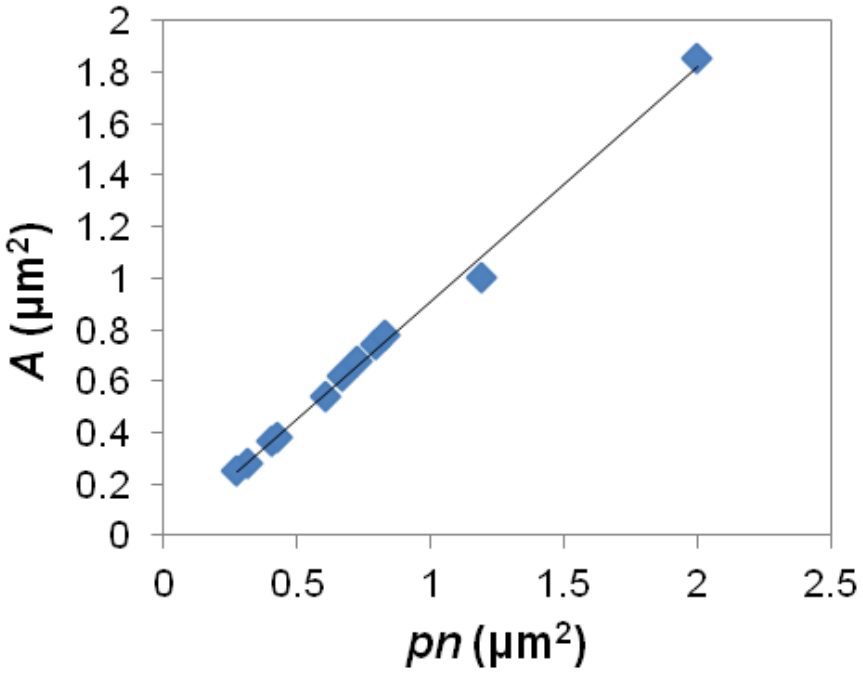

Figure 5.7 Plot of *A* vs. *pn* where *A*, *p* and *n* are structural parameters of the nanofin structure and are illustrated in Figure 5.4. The best fit line drawn through the data points has a gradient value of 0.912 and passes through the origin.

More generally, we can now express *f* (from Eqn. (5.5)) as

$$f = \frac{0.912\,pn}{(1-\phi_s)(p+q)(m+n)} \tag{5.14}$$

With Eqn. (5.14), β in Eqn. (5.13) can now be fully predicted based on the geometry of the nanofins alone. In Figure 5.8, the computed values of β are validated against experimental results and it can be observed that Eqn. (5.13) provides excellent predictions for β in both *z (normal)* and *z (parallel)* directions, indicating that our model accurately reflects the dynamics of wicking in the nanostructured surfaces.

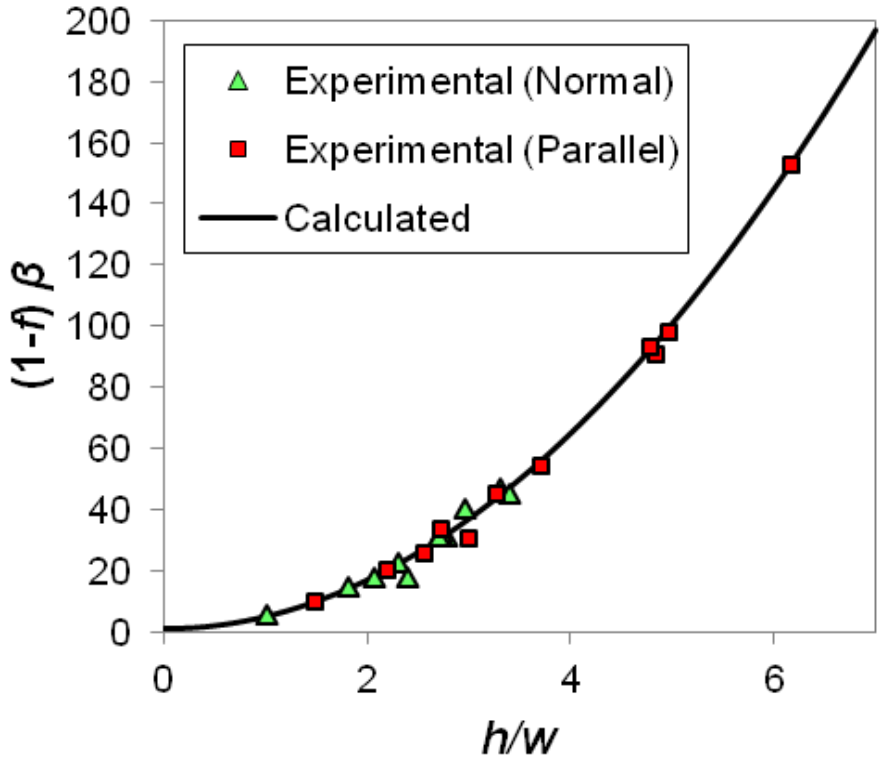

Figure 5.8 Experimental values of $(1 - f)\ \beta$ vs. h/w where f represents the fraction of fluid that is stagnant, β is the drag enhancement factor, h and w are the height and width of the nanochannel used to appromixate the flow, respectively. Note that $f = 0$ for wicking in *z (parallel)* direction.

One of the most pertinent insights derived from this result is that the capillary driving pressure is not axis or direction dependent but the obstruction to the flow (represented by β) caused by the anisotropic nanostructures is. The more streamlined a nanostructure geometry is along the direction of flow, the

lower the value of β. Quantitatively, this can be seen from Eqn. (5.13), which shows that, all else remaining constant, a lower f (due to a smaller p) leads to a lower β and consequently, a faster wicking speed. In short, wicking in anisotropic nanostructures will always proceed faster in the direction that induces a lower form drag. This has important implications for the design of nanostructures used to induce uniaxial or even directional wicking. It also means that nanostructure geometries involving flat planes normal to a given wicking direction are not ideal to maximize the rate of wicking in that direction.

Additionally, other than providing a means of estimating β theoretically, Eqn. (5.13) also reveals insights about the wicking process that may not be obvious at the first glance. An example is that β *(parallel)* may not always necessarily be smaller than β *(normal)* even though wicking in *z (parallel)* is only subjected to viscous drag, whereas wicking velocity in *z (normal)* is retarded by both viscous and form drag. To understand this clearly, let us consider the simplified case where $4h^2/w^2 >> 1$ for wicking in both *z (normal)* and *z (parallel)* directions. It can be easily shown that

$$\frac{\beta\,(parallel)}{\beta\,(normal)} = (1-f)\left(\frac{w_n}{w_p}\right)^2 \tag{5.15}$$

The relationship of β *(parallel)* and β *(normal)* is therefore dependent on the values f, w_n and w_p, which can be combined in the form shown in Eqn. (5.15) to give a value greater than or equal to 1. Plotting the experimental values of β *(parallel)*/ β *(normal)* against $(1-f)(w_n/w_p)^2$ for samples where h/w

> 2 (Figure 5.9), it can be seen in that Eqn. (5.15) is a valid approximation for predicting the relative magnitudes of *β (parallel)* and *β (normal)*.

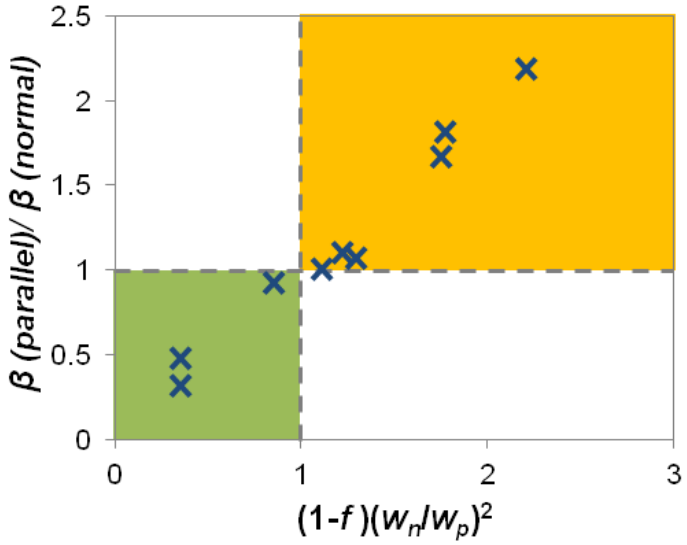

Figure 5.9 Plot of *β (parallel)/ β (normal)* vs. $(1\text{-}f)(w_n/w_p)^2$. *β (parallel)* > *β (normal)* in the orange region and *β (parallel)* < *β (normal)* in the smaller green region. No data points were expected to reside in the white regions. Only data from samples with *h/w* > 2 for both *z (normal)* and *z (parallel)* were used in this plot.

5.6 Conclusions

In conclusion, the dependence of wicking dynamics on the geometry of nanoscale surface structures was investigated with orderly arrays of anisotropic nanofins. It was found that nanostructures dissipate flow energy through viscous and form drag. While viscous drag was present for every form of nanostructure geometry, form drag was only associated with nanostructure geometries that have flat planes normal to the wicking direction. It was also

proved that the viscous dissipation for a unit cell of nanofin could be effectively approximated with a nanochannel of equivalent height and length that contained the same volume of liquid. The energy dissipation by form drag per unit cell of nanofin was found to be proportional to the volume of the fluid between the flat planes of the nanofins.

Combined together with the insights deduced in Chapter 4, we were able to generalize the dependence of β, the drag enhancement factor, on the geometrical parameters of the nanostructures. This is important as it provides a precise method to adjust β, and therefore wicking velocity, for a given direction on a surface by means of nanostructure geometry.

5.7 References

1. J. Bico, C. Tordeux, and D. Quéré. Rough wetting. *Europhysics Letters* **2001**, 55[2] 214.

2. C. Ishino, M. Reyssat, E. Reyssat, K. Okumura, and D. Quéré. Wicking within forests of micropillars. *Europhysics Letters* **2007**, 79 56005.

3. G. McHale, N. J. Shirtcliffe, S. Aqil, C. C. Perry, and M. I. Newton. Topography Driven Spreading. *Physical Review Letters* **2004**, 93[3] 036102.

4. D. Chandra and S. Yang. Dynamics of a droplet imbibing on a rough surface. *Langmuir : the ACS journal of surfaces and colloids* **2011**, 27[22] 13401-13405.

5. M. Zhou, J. Yu, J. Li, B. Wu, and W. Zhang. Wetting induced fluid spread on structured surfaces at micro scale. *Applied Surface Science* **2012**, 258[19] 7596-7600.

6. Y. Chen, L. S. Melvin Iii, M. M. Weislogel, R. M. Jenson, S. Dhuey, and P. F. Nealey. Design, fabrication, and testing of microporous wicking structure. *Microelectronic Engineering* **2008**, 85[5–6] 1027-1030.

7. M. Reyssat, L. Courbin, E. Reyssat, and H. A. Stone. Imbibition in geometries with axial variations. *Journal of Fluid Mechanics* **2008**, 615 335-344.

8. W. K. Choi, T. H. Liew, M. K. Dawood, H. I. Smith, C. V. Thompson, and M. H. Hong. Synthesis of Silicon Nanowires and Nanofin Arrays Using Interference Lithography and Catalytic Etching. *Nano Letters* **2008**, 8[11] 3799-3802.

9. M. K. Dawood, T. H. Liew, P. Lianto, M. H. Hong, S. Tripathy, J. T. L. Thong, and W. K. Choi. Interference lithographically defined and catalytically etched, large-area silicon nanocones from nanowires. *Nanotechnology* **2010**, 21[20] 205305.

10. C. Y. Wang. Stokes flow through an array of rectangular fibers. *International Journal of Multiphase Flow* **1996**, 22[1] 185-194.

11. D. J. Acheson, "Elementary Fluid Dynamics." Oxford University Press, (1990).

12. T. T. Mai, C. Q. Lai, H. Zheng, K. Balasubramanian, K. C. Leong, P. S. Lee, C. Lee, and W. K. Choi. Dynamics of Wicking in Silicon Nanopillars Fabricated with Interference Lithography and Metal-Assisted Chemical Etching. *Langmuir* **2012**, 28[31] 11465-11471.

Chapter 6

Results and Discussion III: Influence of geometry on spreading of liquid on silicon nanostructures

6.1 Introduction

As mentioned in Chapter 4, it can be seen from the plot of wicking distance versus the square root of time that the extrapolation of the curve does not pass through the origin (see Figure 4.8). A closer look at the figure reveals that the wetting process is separated into two regimes. In the first regime, the droplet spreads extremely fast. This lastes for only a few seconds (for silicone oil) or milliseconds (for water) after the liquid touched the wetting surface, and leads to the steep slope observed. In the second regime, the droplet spreading slows down and results in a gentler slope. Similar observations were reported in other studies.[1,2] It has been identified that the latter regime is associated with wicking. However, the rapid spreading of the liquid in the initial stage shows that there may be different mechanisms operating apart from wicking. It is our interest to figure out what are the dominating factors or forces in this stage. For ease of fabrication and analysis, we focus the study on

the onset of wicking of DI water on nanopillar surfaces at different heights using different drop sizes.

6.2 Experimental details

The fabrication process of making nanopillar structures using IL-MACE is the same as described in Chapter 4 and will therefore not be repeated in this section. The only difference during the experimental setup is that the samples were placed horizontally on a flat surface (Figure 6.1). This is because when putting the samples vertically as in previous chapters, the thin film penetrates the nanostructures but the liquid bulk retreats back to the ground under the influence of gravity after a while. The volume of this portion of the liquid is unknown due to the unconventional shape that it assumes. To simplify the process and to enable quantitative study of the initial stage of the wetting process, we carried out experiments with the samples lying horizontally on a flat surface.

In addition, since it is important to know exactly how much liquid was dispensed, the samples were placed on a micro balance as shown in the experiment setup (Figure 6.1). The micro balance has a resolution of 0.1 mg. Since the density of DI water in air is known, it is easy to estimate the volume of liquid dispensed.

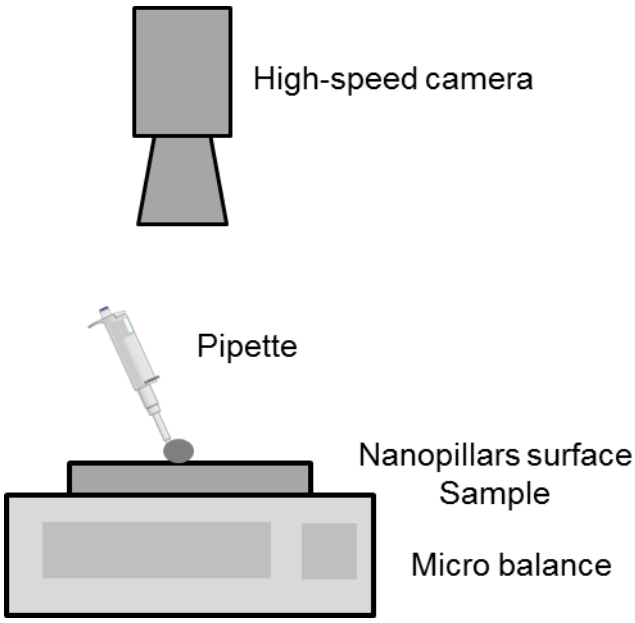

Figure 6.1 Experimental setup for the spreading experiments of liquid on nanostructure surfaces. The samples were put on a horizontal surface. The microbalance serves to determine the amount of liquid dispensed.

In this experiment, water (ρ = 1000 kg/m^3) was chosen as the testing liquid instead of the silicone oil used in previous chapter. This was because silicone oil was extremely viscous and we noticed that after dispensing, some of the oil remained inside the tip of the pipette which made it very difficult to measure the exact volume of liquid dispensed on the surface. Water did not suffer from this shortcoming. In fact, when the water droplet was not too large, it formed a quasi-sphere shape on the tip of the pipette which made it relatively easy to estimate the volume (using the well-known equation $V_{drop} = \frac{4}{3}\pi R^3$ where R is the radius of the droplet).[3] We found that for water, the droplet remained spherical at the tip of the pipette as long as its volume did not exceed 5 µl (Figure 6.2). A bigger drop would make its shape deviate from a sphere and cause experimental errors. The calculated volume was then confirmed with the weight data collected from the micro balance.

Figure 6.2 Water droplet of 1 µl forms a perfect sphere on the tip of the pipette.

One challenge in the setup of this experiment was that the high speed camera required a very strong light source to adequately illuminate the sample under test. However, this strong light source became a heat source which evaporated the water droplet as it spread. The problem was aggravated when the water volume was small (about 0.5 µl). It became difficult to obtain meaningful data since the water vaporized very quickly. Therefore, we have chosen the drop size to be 1 – 2.5 µl in volume (or 0.62 – 0.78 mm in radius). The intensity of the light source was also reduced and as a result, the recording speed decreased to 250 fps, instead of 1000 fps used in previous chapters.

A total of eight nanopillar samples with varying heights were fabricated for this study. Detail dimensions of the samples can be found in

Table 6.1. Again, to measure the displacement of the wicking front with time, DI water droplets of various volumes (1 – 2 µl) were deposited at the center of the sample using a pipette. The pipette was moved very slowly so that the approaching velocity was assumed to be very small and the kinetic energy transferred to the droplet could be ignored. Measurements and analysis of the captured video were carried out using the embedded software Photron FASTCAM Viewer.

Table 6.1 Dimensions of silicon nanopillars fabricated by the IL-MACE method. Crucial parameters such as diameter, height, and period of the nanopillars are shown. The surface roughness r and solid fraction ϕ_s were also calculated.

	Nanopillar Diameter (µm)	**Nanopillar Height (µm)**	**Period of nanopillar array (µm)**	ϕ_s	r
Pillar A	0.30	1.24	0.75	0.13	3.08
Pillar B	0.30	1.66	0.9	0.09	2.96
Pillar C	0.42	2.64	0.9	0.17	5.28
Pillar D	0.40	2.66	0.9	0.16	5.13
Pillar E	0.30	4.05	0.75	0.13	7.79
Pillar F	0.30	4.18	0.75	0.13	8.00
Pillar G	0.30	4.76	0.75	0.13	8.98
Pillar H	0.30	5.39	0.75	0.13	10.03

6.3 Shape Matters

When the droplet comes in contact with the solid surface, there are two possible scenarios of wetting that have been studied experimentally and theoretically.[1] Firstly, for the partial wetting case (hydrophilic surface), the drop forms an equilibrium contact angle with the solid substrate. Secondly, for the total wetting (super-hydrophilic) case, the liquid will completely cover the substrate in order to reduce the total surface energy. However, the liquid will not be flattened out but was seen to be composed of a liquid bulk and the precursor thin film expanding ahead of the bulk (Figure 6.3).

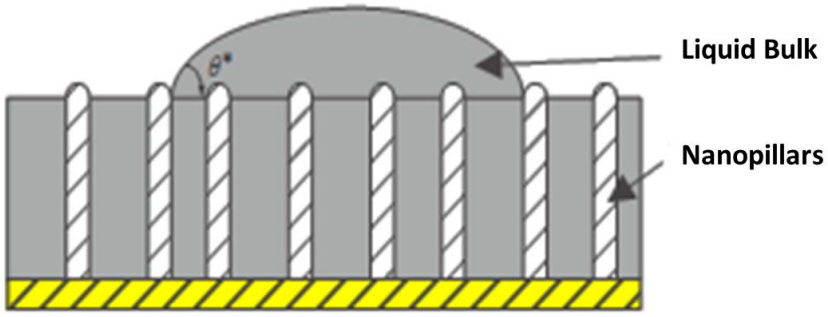

Figure 6.3 Illustration of the liquid bulk and the thin film spreading on a silicon nanopillar surface.

To model the spreading process, it is necessary to determine the precise volume of the droplet. Therefore, the exact shape of the droplet on the surface has to be identified. When the liquid touches the solid surface, it is assumed that the liquid bulk maintains an approximate shape, such as a spherical cap. This assumption is generally accepted if the radius of the droplet R is much smaller than the capillary length.[1,4] For DI water, the capillary length is about 2.7 mm, which is much larger than the liquid bulk

radius of about 0.7 mm in our experiment (Figure 6.2). Hence, we can safely assume that the liquid bulk will take the shape of a spherical cap. For droplet dispensed on a flat silicon surface, this proves to be right (Figure 6.4(a)).

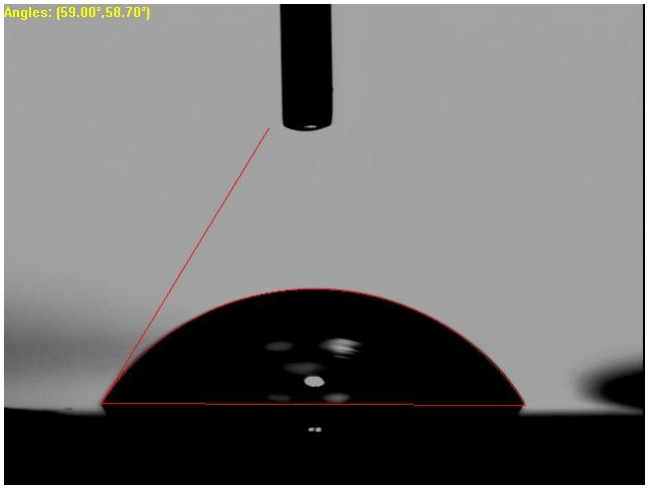

(a)

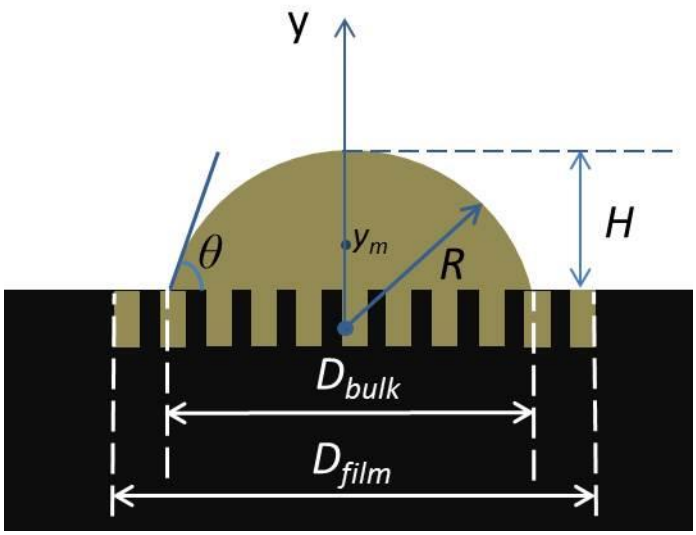

(b)

Figure 6.4 (a) A 1µl water droplet on a flat silicon surface resulted in a spherical cap shape; and (b) Schematic diagram of a spherical cap with dimensional parameters. *R* is the radius of the spherical cap. *H* is the height of the droplet. D_{bulk} and D_{film} is the spreading diameter of the liquid bulk and the thin film, respectively. y_m denotes the center of gravity for the droplet. And θ is the contact angle.

For the ideal case where the liquid droplet is resting on a horizontal plane, the droplet takes the shape of a spherical cap where the base contour is circular and the contact angle is constant around the base. The volume of the spherical cap is given as [5]

$$V_{cap} = \frac{\pi D_{bulk}^{\ 3}}{24}\left(\frac{\cos^3\theta - 3\cos\theta + 2}{\sin^3\theta}\right), \tag{6.1}$$

where D_{bulk} is the spreading diameter of the liquid bulk and θ is the contact angle (Figure 6.4(b)).

Although the contact angle θ cannot be measured directly, it can be estimated by applying the conservation of mass equation $V_{drop} = V_{cap} + V_{film}$ where V_{drop} is the total volume of the droplet, V_{cap} can be calculated by Eqn. (6.1) and V_{film} represents the amount of liquid contained inside the nanostructures and can be calculated as

$$V_{film} = \frac{\pi D_{film}^2}{4}(1-\phi_s)h \tag{6.2}$$

where ϕ_s and h are the fraction of area of the pillars and the pillar height, respectively.

The surface area of the spherical cap (which excludes the surface area of the bottom of the spherical cap, which is equal to $\frac{\pi D_{bulk}^{\ 2}}{4}$) is given as

$$S_{cap} = 2\pi RH \tag{6.3}$$

where R and H are the radius of the spherical cap and height of the droplet, respectively (see Figure 6.4(b)).

Since the contact angle is constant around the base, we can express R and H as

$$R = \frac{D_{bulk}}{2\sin\theta} \tag{6.4}$$

and

$$H = \frac{D_{bulk}(1-\cos\theta)}{2} \tag{6.5}$$

Substitute Eqns. (6.4-5) into Eqn. (6.3) to obtain

$$S_{cap} = 2\pi \frac{D_{bulk}{}^2(1-\cos\theta)}{\sin\theta} \tag{6.6}$$

In addition, the distance between the center of gravity of a spherical cap and the center of the sphere y_m (Figure 6.4(b)) was derived as

$$y_m = \frac{3(2R-H)^2}{4(3R-H)}, \tag{6.7}$$

where R and H are the radius and height of the spherical cap, respectively (see Figure 6.4(b)). This expression will be used in section 6.4.1.2. Note that the detailed proof for y_m can be found in Appendix B.

6. 4 Results and Discussion

From the high speed camera recorded images, data for spreading of the liquid bulk and thin film were extracted. The liquid bulk could be seen to take the shape of a spherical cap whereas the thin film could be identified by the darkened circle extended ahead of the liquid bulk (Figure 6.6).

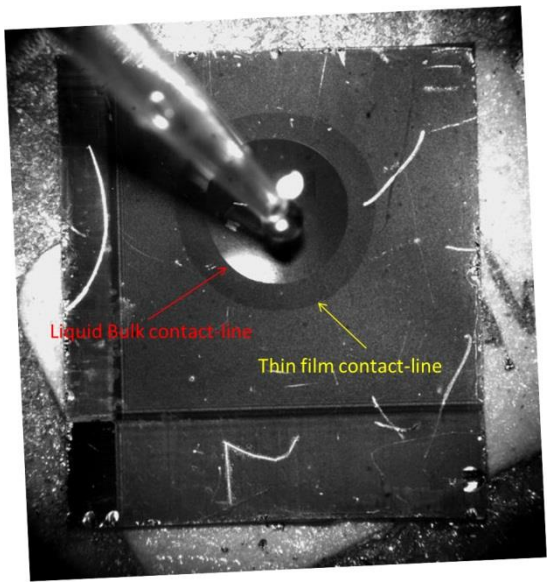

Figure 6.6 The separation of liquid bulk and thin film spreadings as seen at $t > t_c$.

The spreading distances of the liquid bulk and the thin film were measured as a function of time. The spreading distances were plotted against the square root of time. Figure 6.7 illustrates such plot for one representative sample.

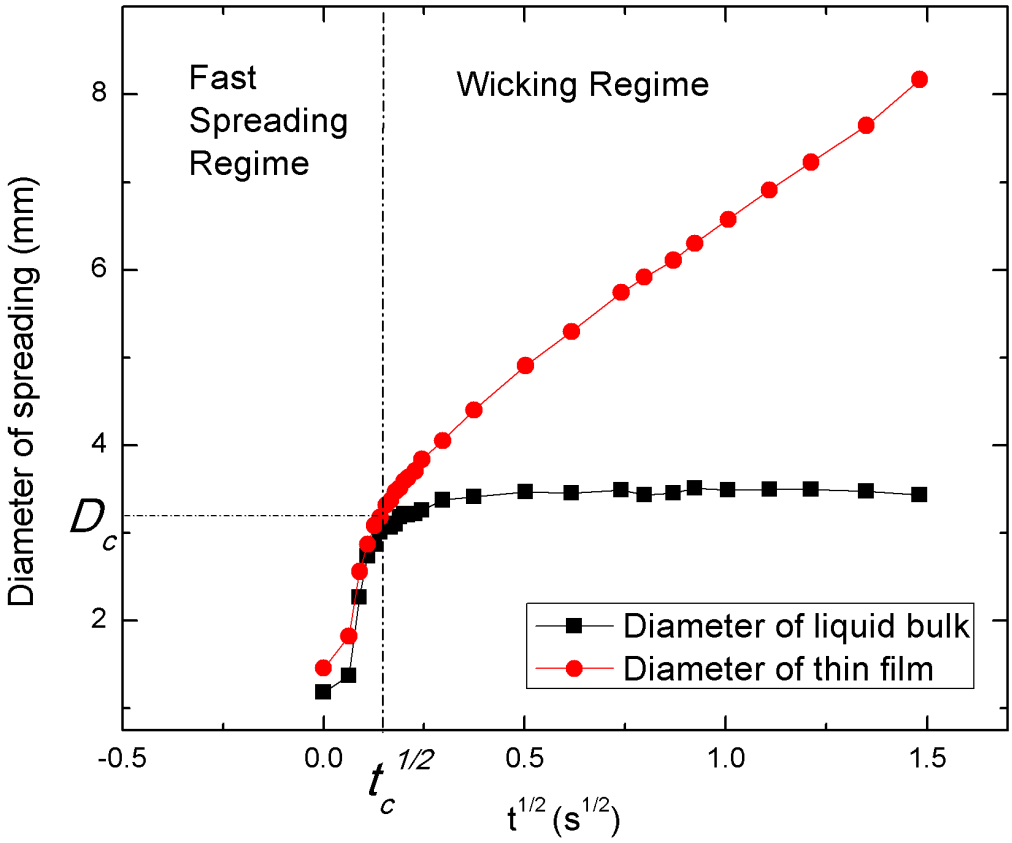

Figure 6.7 Spreading distances of the liquid bulk and the thin film versus the square root of time. The spreading and wicking regimes are clearly shown. The spreading diameter D_c and the cross over time t_c were identified.

In this figure, the separation of the two regimes of wetting is clearly shown. Specifically, there is a cross-over time, t_c, when a sharp transition in the dynamics of spreading occurs. It is noticeable that at $t < t_c$, the liquid spreads out rapidly and reaches a cross-over diameter D_c. In this instance, there is very little difference between the liquid bulk and the thin film spreading diameter ($D_{bulk} \approx D_{film} = D_c$). After t_c, the liquid bulk almost stops spreading, hence the flat line. However, the thin film diameter continues to extend, though at a slower speed. The fact that both the bulk and the thin film spreading have the same cross-over time t_c suggests that the physical mechanism for the initial stage is the same.

Similar to our finding, there are a few studies in the literature that reported a sharp change in dynamics of wetting.[1,4] The second regime which occurs at a later stage was governed by wicking where the capillary and viscous forces control the dynamics. This has been discussed in great detail in the previous chapters.

In this chapter, we only focus on the first regime where the spreading of liquid bulk and thin film is extremely rapid ($t < t_c$). The fundamental question here is what determines the cross-over time t_c and cross-over diameter D_c. To answer this question, we investigate different aspects that affect the liquid spreading such as the roles of geometries and gravity. To study the effect of the former, we conducted experiments on several silicon nanopillar samples of the same dimensions (diameter and period) but different heights. To look at the effect of gravity, we tested the wetting of the same sample but with different droplet sizes. The following sections will present our findings.

6.4.1 Effect of Geometry

In this experiment, we looked at how geometry or surface roughness affects spreading. For our samples, the roughness was varied via the nanopillar heights ranging from 1.24 – 5.39 μm as shown in Table 6.1. Since other

parameters (such as diameter and period) of the nanopillars were similar, the ratio of the roughness was the same as the ratio of heights of the nanopillars.

6.4.1.1 Difference in Spreading Diameters and Contact Angles

The spreading distance of the liquid bulk versus time for samples with different pillar heights is plotted in Figure 6.8.

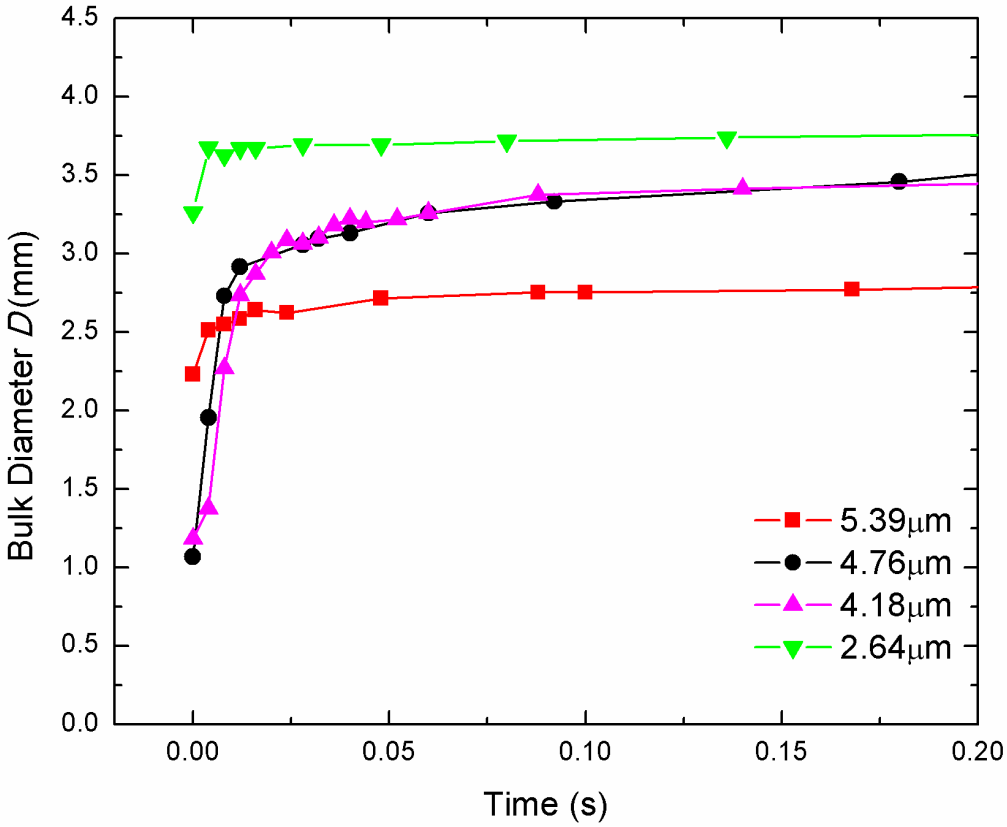

Figure 6.8 Time evolution of the liquid bulk's spreading distance for nanopillar samples of different pillar heights. The liquid volume is 1 μl for all cases.

This figure shows that upon coming in contact with the solid surface, the liquid bulk spreads out rapidly until it reaches a cross-over diameter D_c and then slows down significantly. Note that the values of D_c vary between

different samples, but generally, D_c is larger for samples with shorter pillar heights.

Singh *et al.*[6] suggested that surface roughness enhances spreading in the case of complete wetting. In other words, for a hydrophilic surface with higher roughness level, the wettability or spreading property is magnified. This theory has been corroborated by other studies.[7,8] In our case, it means that for a fixed time, the spreading diameter is wider for taller pillar samples. This is in contrast to our results shown in Figure 6.8 in that, at t_c, the shorter pillar sample actually has a larger spreading distance compared to the taller pillar sample (Figure 6.8). For instance, the samples with 2.64 μm and 5.39 μm nanopillars have spreading diameters of 3.67 and 2.64 mm, respectively. This means that the tall pillar surface provides more resistance and impedes the spreading of the liquid bulk. Repeated experiments show the same trend and thus, external factors such as impact velocity are deemed to be negligible. Note that this trend does not apply to the second regime where we found that the wicking speed for taller pillar samples is faster than short pillar samples. The explanation for this characteristic in the second regime was already given in Chapter 4.

One can argue that this behavior is expected because the taller pillar samples have more space between the pillars for the liquid to fill up. Since the total volume of liquid dispensed on the surface is the same, the liquid inside the bulk is smaller for tall pillar samples and thus, will take up less space. In other words, the spreading diameter D_c is smaller for tall pillar samples. To

validate this argument, we have calculated the volume of liquid in between pillars V_{film} at t_c as a percentage of the original volume for comparison.

Note that at t_c, the difference between the precursor thin film and the liquid bulk diameter was negligible (i.e. $D_{bulk} \approx D_{film} \approx D_c$). We express the percentage of liquid contained in the pillars as a function of total liquid dispensed by dividing V_{film} calculated in Eqn. (6.2) by the total volume of the droplet V_{drop} and the results are shown in Table 6.2. As can be seen from this table, the contribution of V_{film} is only about 2 – 3 % of the total droplet volume. This negligible difference in V_{film} cannot justify the large difference in D_c for tall and short pillar samples.

Table 6.2 The volumes of the liquid contained in the pillars V_{film} are calculated as a percentage of the original droplet volume V_{drop} for different samples at cross-over time t_c.

	Nanopillar Height (μm)	**t_c (s)**	**D_c (mm)**	**V_{film} / V_{drop} (%)**	**Contact Angle (°)**
Pillar C	2.64	0.008	3.6708	2.83%	11.73
Pillar F	4.18	0.012	3.2219	2.81%	28.39
Pillar H	5.39	0.012	2.6406	3.25%	32.30

Another interpretation can be deduced from Table 6.2. Since the total droplet volume on different samples is the same and the amount of liquid between the pillars is approximately the same, the liquid bulk must have roughly the same volume of liquid. Using Eqns. (6.1) and (6.2), we concluded that the wider spreading liquid bulk must have a smaller contact angle as shown schematically in Figure 6.9.

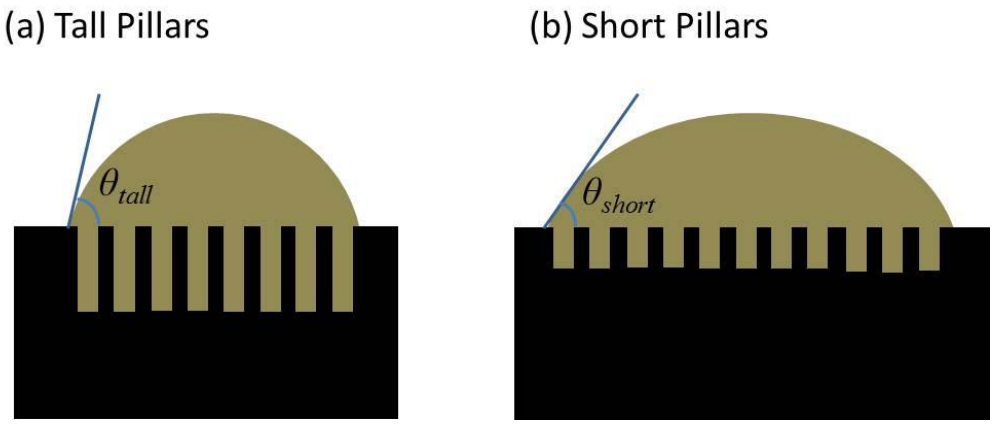

Figure 6.9 Illustration of different contact angles at cross-over time for (a) a tall pillar sample and (b) a short pillar sample. It can be seen that $\theta_{tall} > \theta_{short}$.

6.4.1.2 Energy Dissipation per Unit Area

From the energy point of view, spreading is preferable if the total energy of the system is reduced.[2] Let us consider two systems: one just before the droplet touches the surface (Figure 6.10(a)) and the other at t_c (Figure 6.10(b)).

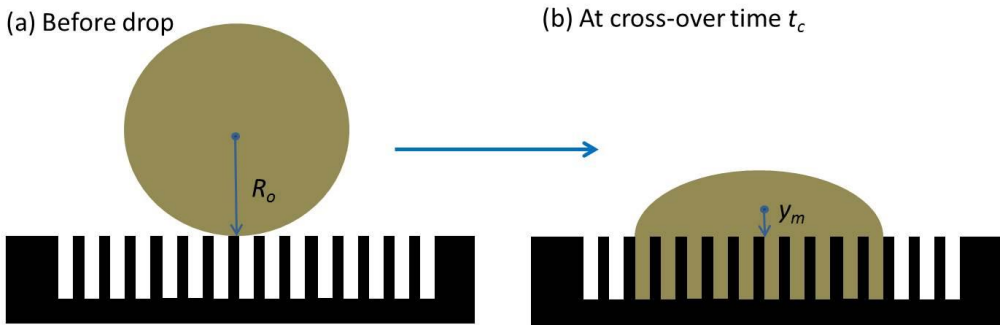

Figure 6.10 Illustration of two energy states: (a) before the droplet touches the solid surface and (b) at t_c.

Considering the two systems in Figure 6.10, there is a continuous transformation and exchange of potential and interfacial energies. The system

depicted in Figure 6.10(a) possesses potential energy originating from the gravitational effect, and interfacial energies originating from the surface tensions at the liquid - vapor and solid – vapor interfaces. The system depicted in Figure 6.10(b) possesses a lower potential energy, a higher liquid - solid interfacial energy and a reduction of solid - vapor interfacial energy compared to the system in Figure 6.10(a). This is because the center of mass of the liquid bulk is lowered, while the solid - vapor interface is replaced by the solid-liquid interface.

The expressions for various energy components of the two systems are identified and listed in Table 6.3. Note that the interfacial energy is calculated as $E = \gamma A$, where γ is the surface tension between the two interfaces (either liquid - vapor, liquid - solid or solid - vapor interface), and A is the surface area of the interface.[9]

Table 6.3 Identification of energy components prior to droplet touches the solid surface and at cross-over time t_c.

	Before dispense	At t_c
Potential Energy	$E_{pot} = mgR_o$	$E_{pot} = mg(y_m - (R-h))$
Liquid-Vapor Surface Energy	$E_{LV} = 4\pi R_o^2 \gamma_{LA}$	$E_{LV} = 2\pi RH\gamma_{LA}$ [d]
Liquid-Solid Surface Energy	$E_{SL} = 0$	$E_{SL} = \frac{\pi D^2 \gamma_{SL} r}{4}$
Solid-Vapor Surface Energy	$E_{SV} = \gamma_{SV} A_{total}$	$E_{SV} = \gamma_{SV} A_{total} - \frac{\pi D^2 \gamma_{SV} r}{4}$

[d] The surface area of the spherical cap is described in Eqn. (6.3)

Summing up the components of the two columns in Table 6.3, the total energy of the system right before the droplet was dispensed is

$$E_{before} = mgR_o + 4\pi R_o{}^2\gamma_{LV} + \gamma_{SV}A_{total} \tag{6.8}$$

and the total system energy at t_c is

$$E_{after} = mg(y_m - (R-H)) + 2\pi RH\gamma_{LV} + \frac{\pi D^2 r(\gamma_{SL} - \gamma_{SV})}{4} + \gamma_{SV}A_{total} \tag{6.9}$$

Note that the Young's law (Eqn. (2.1)) states that

$$\cos\theta = \frac{\gamma_{SV} - \gamma_{SL}}{\gamma_{LV}},$$

where θ is the equilibrium contact angle of water on a flat silicon surface and was measured using a contact angle goniometer to be θ = 56°. γ_{LV} was found in the datasheet to be γ_{LV} = 0.073 N/m.

Substitute Eqn. (2.1) into Eqn. (6.9), one obtains

$$E_{after} = mg(y_m - (R-H)) + \pi DH\gamma_{LV} - \frac{\pi D^2 r\gamma_{LV}\cos\theta}{4} + \gamma_{SV}A_{total} \tag{6.10}$$

The conservation of energy dictates that

$$E_{before} = E_{after}$$

$$\text{or,} \quad mgR_o + 4\pi R_o^2\gamma_{LV} = mg(y_m - (R-H)) + \pi DH\gamma_{LV} - \frac{\pi D^2 r\gamma_{LV}\cos\theta}{4} \tag{6.11}$$

The values for energies before liquid dispensing (the left hand side of Eqn. (6.11)) and at t_c (the right hand side of Eqn. (6.11)) were calculated and

summarized in Table 6.4. As shown in this table, the contribution from potential energy is much smaller (of about two orders of magnitude) compared to the contribution from interfacial energies. This reveals that the gravitational force is weaker than the surface tension forces and the latter is the dominant driving force at this stage of spreading.

Also it can be seen that for all samples, the energies at the two states are not equal $E_{before} \neq E_{after}$. The difference between them, which represents an energy loss in the system, is shown in the last column of the table.

For a closed system, the first law of thermodynamics states that

$$\Delta E = Q - W , \tag{6.12}$$

where ΔE, Q, W are the change of internal energy, the heat added to the system and the work done by the system, respectively. In this case, it is assumed that there is no change in the temperature of the liquid droplet or the silicon surface, i.e. $Q = 0$. Therefore, the energy loss observed is due to the work done by the system.

Table 6.4 Energy components of the system before dispensing and at cross-over time. Here *h* stands for the nanopillar height. E_{pot} is the potential energy, E_{LV}, E_{SL}, E_{SV} are the interfacial energy of liquid - vapor, solid-liquid and solid-vapor interfaces, respectively.

$V_{drop} \approx 1$ µl	*h* (µm)	E_{pot} (x10^{-7} J)		E_{LV} (x10^{-7} J)		$E_{SL} + E_{SV}$ (x10^{-7} J)		$E_{before} - E_{after}$ (x10^{-7} J)
		Before	After	Before	After	Before	After	
Flat surface	0	0.062	0.023	3.52	3.87	0	-1.68	1.38
Pillar A	1.24	0.055	0.008	3.31	5.47	0	-9.27	7.17
Pillar C	2.64	0.062	0.006	3.53	8.09	0	-24.8	21.6
Pillar D	2.66	0.062	0.007	3.51	6.99	0	-20.0	14.5
Pillar F	4.18	0.067	0.001	3.66	4.93	0	-21.1	19.9
Pillar G	4.76	0.062	0.0009	3.51	5.20	0	-25.3	23.6
Pillar H	5.39	0.062	0.001	3.52	4.66	0	-24.9	23.9

In our case, one factor to dissipate the energy is the skin friction due to the contact between the liquid and the solid surface. Because skin friction is proportional to the surface area, the energy loss varies for samples with different nanopillar heights and wetting diameters. Let us normalize the energy loss to the wetted solid surface area to obtain the average energy dissipation per unit area, and plot it against the pillar heights in Figure 6.11.

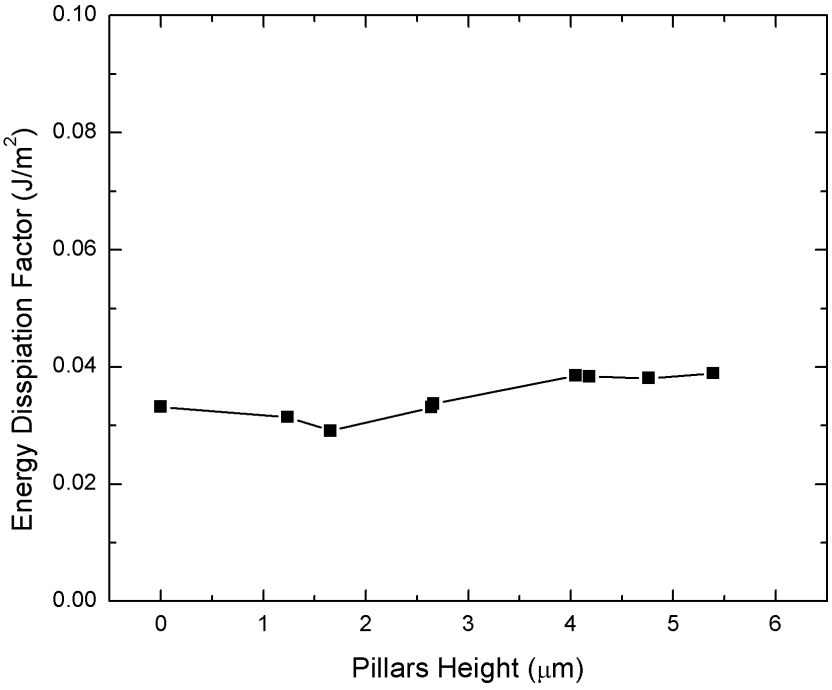

Figure 6.11 Total energy dissipation per unit area for different pillar heights.

From this plot, it is notable that the energy loss per unit area α is consistent for samples with varying nanopillar heights. Interestingly, despite that the values of α seem very close, there appears to be two ranges of values for short and tall pillars. For short pillar samples (h = 0 - 2.7 μm), $\alpha_{short} \approx 0.03$ J/m^2. For tall pillar samples (h = 4.0 – 5.4 μm), α is slightly larger $\alpha_{long} \approx 0.038$ J/m^2. One possible reason for this difference is that the liquid - vapor surface energy may have been overestimated in the case of short pillars. When the bulk diameter increases, its shape deviates from a spherical cap[1] as can be seen in Figure 6.12 and gives rise to the surface area overestimation.

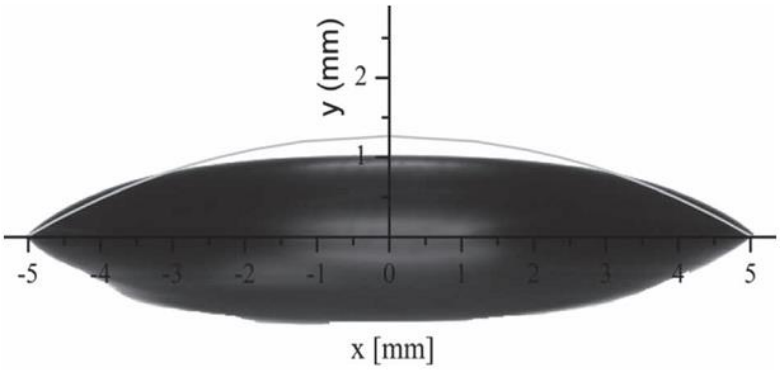

Figure 6.12 Comparison of the spherical cap shape (represented by the solid line) and the real drop shape when spreading diameter is large. Picture taken from Harth *et al.*[1]

Similar to our findings, Carlson *et al.*[10,11] suggested that the energy loss is caused by the contact line friction. The contact line is defined as the intersection of the droplet's liquid – vapor interface and the solid substrate. Carlson *et al.*[10,11] also came up with a non-hydrodynamic parameter called the contact line friction factor μ_f to describe this energy loss. According to this study, μ_f is an intrinsic property of the combination of solid and liquid materials, and is independent of drop sizes.

At this point, we do not have a good explanation for the seemingly constant α value. But as suggested by Carlson,[10] this energy loss per unit area can be considered as the intrinsic property of the combination of the solid material and the wetting liquid, and is independent of other factors such as the drop sizes. To prove whether this is a valid theory, we look at the spreading distance of different drop sizes in the next section. If this is indeed an intrinsic property, the energy loss per unit area α should not be dependent on the drop sizes and should remain the same.

6.4.2 Effect of Drop Size

In this experiment, different drop volume sizes are dispensed on the sample and the diameter of the thin film is recorded as a function of time (Figure 6.13).

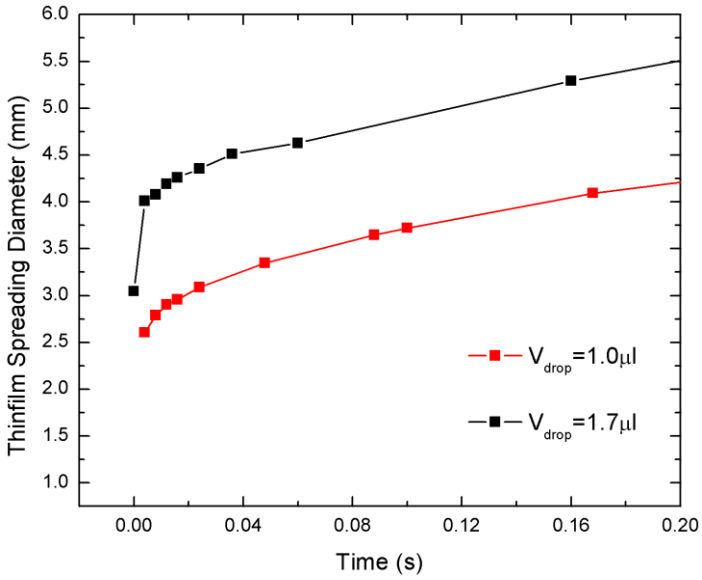

(a)

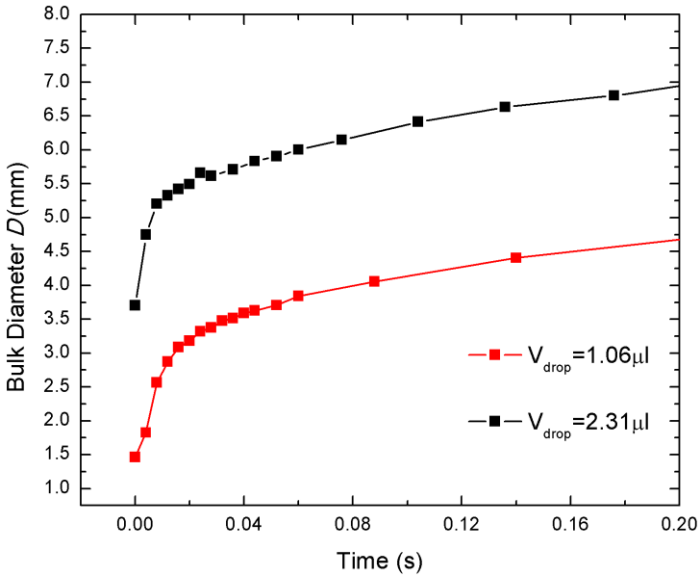

(b)

Figure 6.13 Spreading distance of the thin film diameter versus time for different drop volumes of (a) Sample F (height of 4.18 µm) and (b) Sample H (height of 5.39 µm).

From these plots, the effect of drop size is evident: at t_c, the spreading diameter of the large drop is larger than the small drop. This can be explained by the conservation of mass: since the bigger drop has a larger volume, it is expected to cover more surface area.

Figure 6.13 also shows that in the second regime of wetting, the time evolution of spreading diameter for different drop sizes has the same gradient. In other words, the spreading speed is the same for a specific sample and liquid. This agrees with our theory of wicking presented in Chapters 4 and 5 in which the wicking speed only depends on the geometrical dimensions and the properties of the liquid. Now, let us examine the energy dissipation per unit area for different drop sizes at the cross-over time t_c. The results are shown in Table 6.5.

Table 6.5 Energy dissipation per unit area calculated for different drop sizes.

	Pillars Height (μm)	**Drop size** (μl)	**Total energy dissipated** ($x10^{-7}$ J)	**Energy dissipation per unit area** (J/m^2)
Pillars **A**	1.24	0.91	7.17	0.031
		1.39	11.5	0.028
Pillars **F**	4.18	1.06	19.9	0.038
		2.31	61.3	0.036
Pillars **H**	5.39	1.00	23.9	0.039
		1.70	49.9	0.038

As can be seen from Table 6.5, the energy dissipation per unit area α is consistent with previous observations. For short pillars, $\alpha_{short} \approx 0.033$ J/m^2

while for long pillars, $\alpha_{long} \approx 0.038$ J/m^2 and α indeed does not depend on the drop size. This supports our theory that the energy dissipation per unit area is an intrinsic property of the combination of the solid and the wetting liquid.

6.4.3 Further comments on t_c and D_c

It is interesting to find out how the cross-over time varies across samples at different heights. Figure 6.14 summarizes the value of t_c collected for all samples with various drop sizes.

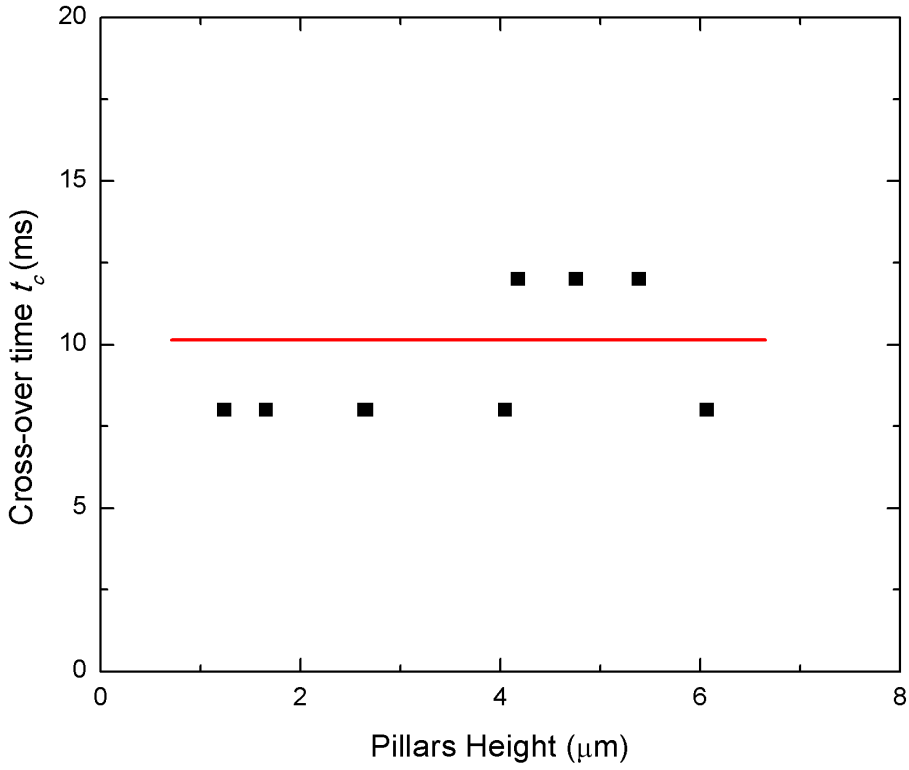

Figure 6.14 Plot of cross-over time versus nanopillar heights for various drop sizes. The red line represents the average value of 10 milliseconds.

From this plot, we can see that the cross-over time is rather consistent ($t_c \approx 10$ milliseconds) and does not depend on the geometry of the nanostructures or the drop size. This value is very close to the cross-over time values observed by Eddi *et al.*[4] ($t_c \approx 1$ - 10 milliseconds) for liquids of varying viscosities, with a higher t_c value corresponding to liquid with higher viscosity. The result also agreed with that of Bird *et al.*[12] in that the millimeter-sized water droplet wets an area having the same diameter as the drop within a millisecond.

According to Courbin *et al.*[13], the duration of the first regime of spreading increases with the size of the drop. However, in our experiment, it is difficult to support this theory. In fact, Figure 6.15 shows that the duration of the initial stage of spreading does not depend on geometry or drop size. Nevertheless, the study by Courbin *et al.*[13] only explains the behavior of wetting before the complete drop touches the surface (for time less than 1.5 milliseconds) and is therefore not applicable to our work (where we are looking at a slightly later period for time later than 4 milliseconds). However, the presented results in this section are not free of shortcomings, one of which arises from the volatile liquid used in the experiment. The high volatility of deionized water requires a slow capturing speed which resulted in the large time uncertainty. Given the frame rate of 250 fps, the uncertainty in the time step is 4 milliseconds for each run.

With the findings from the previous sections, we are able to predict the spreading diameter D_c based on the theory of conservation of mass and energy.

Firstly, from the conservation of mass equation, we have

$$V_{drop} = V_{film} + V_{cap} = \frac{\pi D_{film}^2}{4}(1-\phi_s)h + \frac{\pi H^2(3R-H)}{3}, \qquad (6.13)$$

with $\frac{D^2}{4} = R^2 - (R-H)^2 = H(2R-H)$ as can be seen from Figure 6.4(b).

Substitute into Eqn. (6.13) we can express R in terms of H as

$$R = \frac{\frac{H^3}{3} + H^2(1-\phi s)h + \frac{V_{drop}}{\pi}}{H^2 + 2H(1-\phi s)h} \qquad (6.14)$$

Secondly, incorporating the energy loss factor, the equation for the conservation of energy can be rewritten as

$$mgR_o + 4\pi R_o^2\gamma_{LA} = mg(y_m - (R-H)) + 2\pi RH\gamma_{LA} - \frac{\pi D^2 r\cos\theta_o}{4}\gamma_{LA} + \frac{\alpha\pi D^2 r}{4} \qquad (6.15)$$

Note that the last element on the right hand side of the equation stands for the loss of energy caused by skin friction.

Express D in terms of R and H to arrive at

$$mgR_o + 4\pi R_o^2\gamma_{LA} = mg(y_m - (R-H)) + 2\pi RH\gamma_{LA} - \pi H(2R-H)r\cos\theta_o\gamma_{LA} + \alpha\pi H(2R-H) \qquad (6.16)$$

All parameters in Eqn. (6.16) such as m, R_o, γ_{LA}, r, $\cos\theta_o$, α and y_m are known or can be calculated. Substituting R from Eqn. (6.14) into Eqn. (6.16), we arrive at a non-linear equation where H is the only unknown variable.

There is unfortunately no elegant mathematical expression for *H*. The value of *H* can instead be fitted using optimizers such as Excel's Solver feature. Once the value for *H* is found, *R* and D_c can be calculated. The theoretical values for D_c were plotted against the experimental values in Figure 6.15. As can be seen from this plot, a good fit between the theoretical and experimental data is achieved.

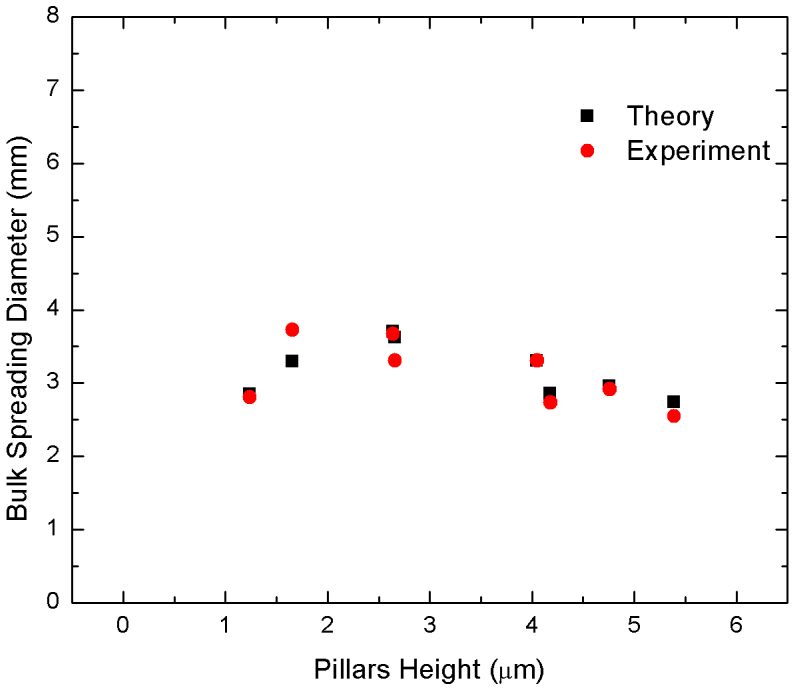

Figure 6.15 Theory and experimental spreading diameter at cross-over time for nanopillars samples of different heights.

6.5 Conclusions

In this chapter, we have investigated the initial stage of spreading of water on silicon nanopillar surfaces and its dependence on geometry and drop size. We postulate that during this initial stage of wetting, the gravity effect is minimal and the driving forces for the spreading are the surface tensions. We found that there is a cross-over time t_c when there is a change-over in dynamics of spreading. Before t_c, the liquid spreads rapidly until it reaches a certain cross-over spreading diameter D_c. After t_c, the wetting process slows down significantly and is dominated by the physics of wicking. We found that t_c is independent of drop sizes as well as geometry.

We also found that the skin friction during the initial spreading process was significant. The values of energy dissipation per unit area, α, were determined to be 0.033 J/m^2 and 0.038 J/m^2 for short and long pillars, respectively. With this finding, the value of D_c could be predicted based on the conservation of energy and mass theories. We believe that α is solely dependent on the combination of solid and liquid materials. Further study with different wetting liquids can be conducted to validate this theory.

6.6 References

1. M. Harth and D. W. Schubert. Simple Approach for Spreading Dynamics of Polymeric Fluids. *Macromol Chem Phys* **2012**, 213[6] 654-665.

2. J. Bico, C. Tordeux, and D. Quéré. Rough wetting. *Europhysics Letters* **2001**, 55[2] 214.

3. A. L. Biance, C. Clanet, and D. Quere. First steps in the spreading of a liquid droplet. *Physical Review E* **2004**, 69[1].

4. A. Eddi, K. G. Winkels, and J. H. Snoeijer. Short time dynamics of viscous drop spreading. *Physics of Fluids* **2013**, 25[1].

5. A. D. Sommers and A. M. Jacobi, "Calculating the Volume of Water Droplets on Topographically-Modified, Micro-Grooved Aluminum Surfaces." in International Refrigeration and Air Conditioning Conference**.** Purdue, 2008.

6. S. K. Singh and B. S. Dandapat. Spreading of a non-Newtonian liquid drop over a homogeneous rough surface. *Colloids and Surfaces A: Physicochemical and Engineering Aspects* **2013**, 419[0] 228-232.

7. R. N. Wenzel. Resistance of Solid Surfaces to Wetting by Water. *Industrial & Engineering Chemistry* **1936**, 28[8] 988-994.

8. D. Bonn, J. Eggers, J. Indekeu, J. Meunier, and E. Rolley. Wetting and spreading. *Rev Mod Phys* **2009**, 81[2] 739-805.

9. E. Guyon, "Physical Hydrodynamics." OUP Oxford, (2001).

10. A. Carlson, G. Bellani, and G. Amberg. Universality in dynamic wetting dominated by contact-line friction. *Physical Review E* **2012**, 85[4].

11. A. Carlson, G. Bellani, and G. Amberg. Contact line dissipation in short-time dynamic wetting. *Europhysics Letters* **2012**, 97[4].

12. J. C. Bird, S. Mandre, and H. A. Stone. Short-time dynamics of partial wetting. *Physical Review Letters* **2008**, 100[23].

13. L. Courbin, J. C. Bird, M. Reyssat, and H. a. Stone. Dynamics of wetting: from inertial spreading to viscous imbibition. *Journal of Physics: Condensed Matter* **2009**, 21[46] 464127-464127.

Chapter 7

Conclusions

7.1 Summary

The wicking of fluids on textured surfaces is an interesting research topic for many decades. However, there has neither been a systematic study on the effect of nanostructured surfaces, nor a theory that could fully describe the dynamics of wicking without the use of fitting parameters. This thesis aimed to fill in this void by investigating the wicking phenomenon both theoretically and experimentally. The dependence of the wicking dynamics on the geometrical variables was thoroughly studied and quantified. The presented work in this study is successful in establishing mathematical expressions that are capable of predicting the wicking process without use of extensive empirical values. This means that the wicking characteristic of a particular material can be controlled by adjusting the geometry properties (i.e. sizes and height) of the nanostructures.

At first, this thesis focused on the uniform and isotropic silicon nanostructured surfaces. Nanopillar structures fabricated by the IL-MACE method were chosen for this study because of the ease of fabrication, and to

the best of the author's knowledge, there has not been a quantitative study of wicking in the nanometer scale. In addition, the size and height of the nanopillar could be controlled easily by the fabrication techniques which proved to be useful in the studying of the surface geometry effect. By approximating a primitive cell of the nanopillar array to that of a nanochannel, the Navier-Stokes equations for fluid dynamics were simplified. With appropriate boundary conditions, the set of complicated differential equations were solved. The enhancement factor of viscous loss, β, due to the presence of nanopillars was found to be $\beta = \frac{4h^2}{w^2} + 1$ where h is the nanopillar height and w is the width of the approximating nanochannel. Excellent fit between theoretical and experimental results was achieved for our samples. Our expression for β was also found to be applicable to reported results by other research groups. However it was discovered when the height of the structures increases, the increase in the frictional force is faster than the increase in the driving force. For this reason, the wicking speed will saturate at a certain structures' height.

Secondly, the dependence of wicking dynamics on the geometry of nanoscale surface structures was further investigated with orderly arrays of anisotropic nanofins. It was found that nanostructures dissipate flow energy through viscous and form drag. While the former is present for every form of nanostructure geometry, the latter is only associated with nanostructure geometries that have flat planes normal to the wicking direction. The energy dissipation by form drag per unit cell of nanofin is proportional to the volume of the fluid between the flat planes of the nanofins in the direction of wicking.

With these findings, the dependence of β on the geometrical parameters of the nanostructures was established. The mathematical expressions of β for different directions of wicking were derived as $\beta = \left(\frac{1}{1-f}\right)\left(\frac{4h^2}{w^2}+1\right)$ where h is the height of nanostructures, f is the fraction of stagnant fluid between the flat planes of the nanofins, and w_n, w_p represent the channel width calculated for wicking in *z (normal)* and *z (parallel)* directions, respectively.

Finally, the initial stage of wetting before wicking occurs was studied. During this stage, the gravity effect is minimal and the driving forces for the spreading are the surface tensions originating from the interfacial forces where the solid, liquid and vapor phase intersect. There is a cross-over time t_c when there is an abrupt change in the dynamics of wetting. Before t_c, the liquid drop spreads rapidly until it reaches a certain cross-over diameter D_c. After t_c, the wetting process slows down significantly and is dominated by the physics of wicking. t_c is found to be independent of drop sizes as well as geometry. It is noted that the skin friction during the initial spreading process is significant. The values of energy dissipation per unit area α ranged between 0.033 to 0.038 J/m^2 for short and long pillars, respectively. With this finding, the value of D_c can be predicted based on the conservation of energy and mass theories. We suggest that the value of α is solely dependent on the combination of the solid and liquid materials.

7.2 Future Works

In the last part of the study we postulated that the value of the energy dissipation per unit area α is solely dependent on the combination of solid and liquid materials. To validate this theory, experiment with different wetting liquid and substrate materials can be carried out. Additionally, due to the limitations in experimental apparatus, the wetting experiments were only recorded at a fairly slow capture speed which gave rise to the experimental error. For a more accurate result, it is suggested to use a less volatile liquid to avoid evaporation during wetting.

It was calculated and confirmed that the range of drop sizes selected for this thesis's experiments does not affect the initial stage of wetting. To obtain a more conclusive result, the drop sizes can be increased further to the range that is comparable to or larger than the capillary length. However in this case, the shape of the droplet deforms from a sphere and makes it more difficult to estimate the interfacial energies.

Lastly, we believe that the insights presented in this thesis are important and useful for the creation of future devices based on wicking. All in all, wetting phenomenon, and wicking in particular, is truly an exciting playground where physics, chemistry, biology and engineering intersect.

APPENDIX A

To demonstrate the relative contribution to U_{mean} by each term in the summation series, we plotted E vs. m when $n = 0$ (Figure A1(a)) and E vs. n when $m = 0$ (Figure A1.b). Typical experimental parameters $w = 1$ μm and $h = 2$ μm were used to compute E. As observed from Figure A1, the value of E falls rapidly with increasing m or n. The second term ($m = 1$ or $n = 1$) is already an order of magnitude below the first term ($m = 0$, $n = 0$) and the rest of terms are approximately zero. E falls faster for m than for n because $4h^2 > w^2$ and thus $4h^2$ mediates the increase of $(2n+1)^2$ in the denominator of E, which would have otherwise cause a much more rapid decrease of E with increasing n. It is not necessary to consider the rest of the cases such as the variation of E with n when $m = 1, 2, 3\ldots$as the largest term of these series (when $n = 0$) is already shown in Figure A1(a) to be negligible compared to the case of $m = 0$ and $n = 0$. For these reasons, we approximate the expression for E to the first term of the summation series ($m = 0$, $n = 0$), which contributes the greatest to the value of E in Eqn. (4.29).

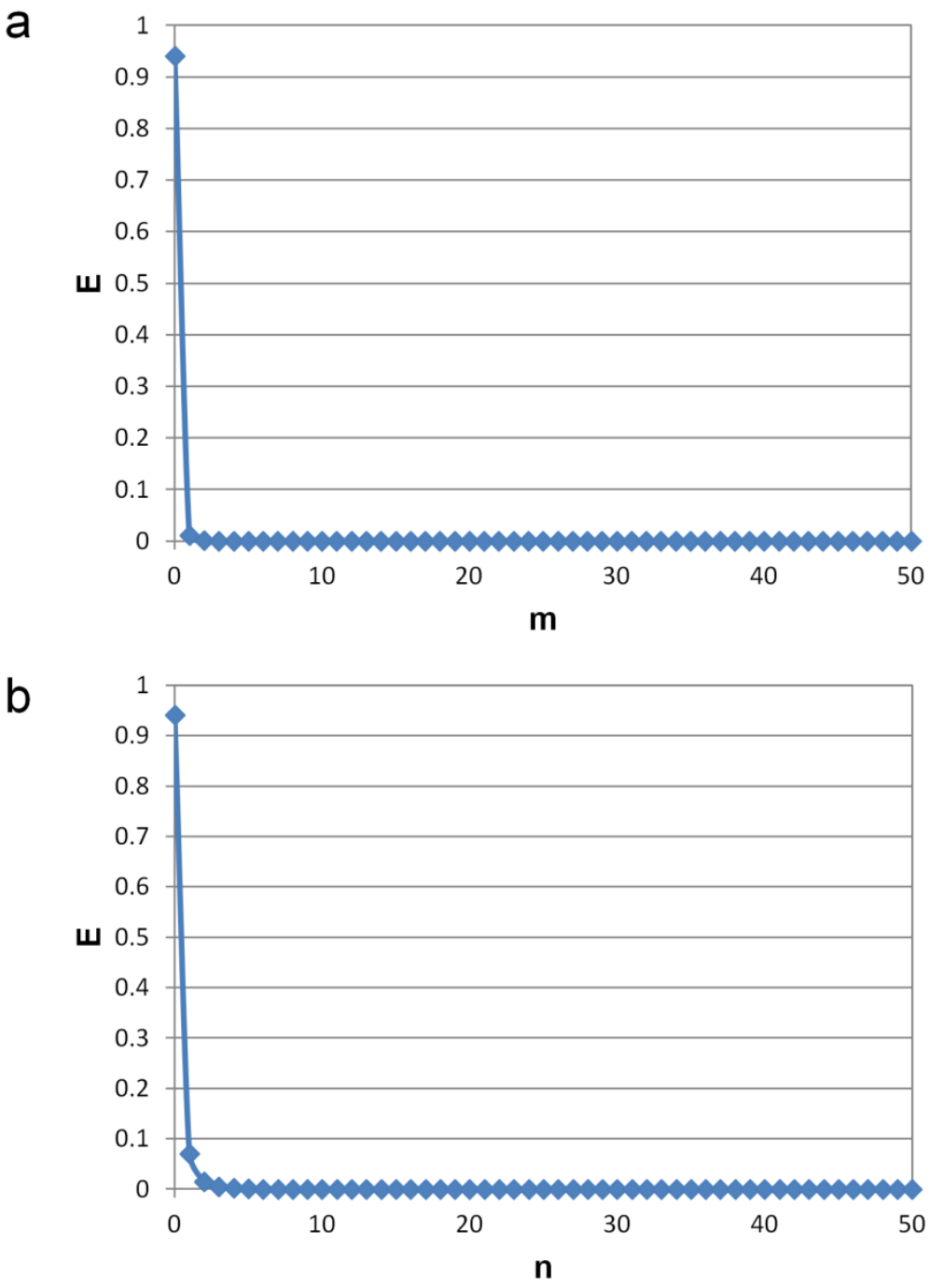

Figure A1 Plot of *E* versus (a) *m* when *n* = 0 and (b) *n* when *m* = 0. Width (*w*) and height (*h*) of the nanochannel are fixed at 1µm and 2 µm respectively.

APPENDIX B

The proof for y_m is given as follow. Due to the symmetrical property of the spherical cap, the center of gravity must lie on the *y*-axis as shown in Figure 6.4(b). To determine the center of gravity, let us imagine that the spherical cap consists of many small slices, each of which has a thickness of *dy* and a mass of *m*. The center of gravity y_m is the average position of the center of gravity of all the slices. In other words

$$y_m = \frac{\Sigma y_i m_i}{\Sigma m_i} = \int \frac{y\rho dV}{\rho V_{cap}} = \int_{R-H}^{R} \frac{y\pi(\sqrt{R^2 - y^2})^2 dy}{\pi \frac{H^2}{3}(3R - H)} = \frac{3\int_{R-H}^{R}(R^2 - y^2)ydy}{H^2(3R - H)}$$

$$= \frac{3}{H^2(3R - H)}\left(\frac{R^2(R^2 - (R-H)^2)}{2} - \frac{R^4 - (R-H)^4}{4}\right)$$

Reduce this equation to arrive at Eqn. (6.6).

Publications

Most of the work presented in this study has been published in the following journals:

[1] Trong Thi Mai, Chang Quan Lai, H. Zheng, Karthik Balasubramanian, K. C. Leong, P. S. Lee, Chengkuo Lee, and W. K. Choi. Dynamics of Wicking in Silicon Nanopillars Fabricated with Interference Lithography and Metal-Assisted Chemical Etching. *Langmuir* **2012** 28[31], 11465-11471

[2] Chang Quan Lai, **Trong Thi Mai**, H. Zheng, P. S. Lee, K. C. Leong, Chengkuo Lee, W. K. Choi. Influence of nanoscale geometry on the dynamics of wicking into a rough surface. *Applied Physics Letters* **2013**, **102** [5], 053104[e]

[3] Chang Quan Lai, **Trong Thi Mai**, H. Zheng, P. S. Lee, K. C. Leong, Chengkuo Lee, and W. K. Choi. Droplet spreading on a two-dimensional wicking surface. *Physical Review E* **2013**, **88**, 062406[e]

The author has also been involved in the following publication:

[4] **Trong Thi Mai**, Fu-Li Hsiao, Chengkuo Lee, Wenfeng Xiang, Chii-Chang Chen, W.K. Choi. Optimization and comparison of photonic crystal resonators for silicon microcantilever sensors. *Sensors and Actuators A: Physical* **2011**, **165**[1], 16-25

[e] C. Q. Lai and T. T. Mai contributed equally to this work